A Study of Pion Photoproduction on Carbon-12 in the Delta Resonance Region.

Thesis

Submitted by

John Alan MacKenzie, B.Sc.

for the degree of

Doctor of Philosophy

Department of Physics and Astronomy
University of Edinburgh
1995

Abstract

This thesis describes a study of the ^{12}C(γ, π^+n) reaction in the Delta resonance region using tagged photons. The experiment was accomplished using the MAMI-B c.w. electron accelerator at the Institut für Kernphysik, Mainz. Bremsstrahlung photons, created when 855 MeV electrons strike a 4 μm Nickel radiator, were tagged with a 2 MeV resolution using the Glasgow tagging spectrometer installed in the MAMI A2 experimental hall.

To perform the measurements, a method of detecting positively charged pions using the Pion-Proton (PiP) plastic scintillator hodoscope was developed. PiP provides solid angle and energy acceptances which enabled data to be obtained over a larger region of phase space than has previously been possible. Combined with the Tübingen time-of-flight array (TOF), exclusive coincidence measurements were performed. Data was analysed for photon energy regions centred at E_γ= 260, 300, 340 and 380 MeV. PiP provided a pion angular coverage of θ_π=52-128° and ϕ_π=(-23)-23° and an energy acceptance E_π=20-180 MeV. The TOF array covered the angles θ_n=10-150° and $\phi_n \approx$ 160-200°. The TOF neutron energy threshold was E_n^{min}=15 MeV. The π^+n channel was isolated and the system's missing energy resolution of 8 MeV was sufficient to identify events leading to p-shell excitation of the residual nucleus.

The data is presented as triple and (by integrating over the pion energy) double differential cross sections. A comparison is made with Distorted Wave Impulse Approximation (DWIA) predictions generated by the code THREEDEE. It is concluded that more reliable theoretical calculations are required. In particular, a better treatment of the distortion and absorption of the outgoing particles is needed.

Initial comparisons with the microscopic theory of Carrasco are attempted and the problems faced in making such a comparison are described and solutions suggested.

Declaration

The data presented in this thesis was obtained in experiments carried out by the Edinburgh University Nuclear Physics group in collaboration with the Nuclear Physics groups at the Universities of Glasgow and Tübingen. The actual experiments, in which I played a major role, were performed at the Institut für Kernphysik at the University of Mainz. The data analysis and interpretation is my own work. This thesis has been written by myself.

John A. MacKenzie

Acknowledgements

Firstly, I am glad of this opportunity to thank all the members of the Edinburgh University Nuclear Physics Group for providing me with a stimulating and supportive environment throughout my three years of study. Deepest thanks go to my supervisor, Derek Branford, for his motivating and guiding influence. I also extend special thanks to Tom Davinson, for imparting some of his not inconsiderable technical knowledge and to my second supervisor, Phil Woods, for his continuous support. The burden of preparation, execution and analysis for the experiment has also been shared with Doug Johnstone and Meme Liang to whom I am most grateful.

The Mainz experiments are a joint venture between the Universities of Edinburgh, Glasgow and Tübingen. The resultant PiP/TOF collaboration has been enjoyable to work within, which, considering the inevitable problems associated with the work, is a tribute to the patience and good nature of all involved. From Glasgow, I would like to thank Peter Harty, Cameron McGeorge, John Annand, Douglas MacGregor, Bob Owens, Gary Miller and Ian Anthony from whose experience I have benefited greatly. Special thanks go to Peter Harty and Cameron McGeorge for the many discussions about the analysis and to John Annand for letting me near his acquisition system (a real act of faith). I am also indebted to fellow analysers, Gillian Cross, Tony Yau and Robin Watson, for sharing the burden of analysis meetings and those beloved night shifts. From Tübingen, I am grateful to Peter Grabmayr, Torsten Hehl, Thomas Lamparter, Ralph Schneider and Karin Spaeth. Special thanks go to Peter Grabmayr for discussions about the analysis code and to Torsten Hehl for his development of the Oset code.

From Amsterdam, I would like to thank Gerard van der Steenhoven for his help with the code THREEDEE and for his encouraging influence.

The work of this thesis would not have been possible without the facilities of the Institut für Kernphysik at Mainz. I am grateful to the Head of the Lab, D. von Harrach, for making them available. Also from Mainz, I would like to thank the A2 spokesperson, Juergen Ahrens, and Reinhard Beck who gave valuable help during the experiments.

During my course, I have been funded by SERC, the now EPSRC, and I am grateful for this support. I am also indebted to Prof. Alan Shotter, who, as Head of the Physics Dept., afforded me use of the facilities here and, as Head of the Group, encouraged me to take up this research and found a studentship for me.

Contents

List of Figures

Chapter 1

Introduction

1.1 Overview

The central success of nuclear physics theory to date is that of the shell model. In this view of the nucleus, neutrons and protons move as independent particles within some phenomenological local potential. The potential can be said to be arbitrary in the sense that it is chosen to reproduce the magic numbers (associated with shell closures) and other nuclear properties e.g. binding energies. Certainly, much of nuclear spectroscopy and many nuclear reactions are described successfully within this framework. It is interesting to note, though, that for many years the success of the shell model remained a puzzle. In particular, it was not understood how a cluster of strongly interacting particles could be so well described by independent particle motion. The answer was found to lie in both the short range nature of the nucleon-nucleon interaction and the influence of the Pauli exclusion principle, which prohibits most nucleon-nucleon scattering due to the lack of available final states in the nucleus.

It is perhaps ironic that these same qualities, which are responsible for the shell model's success, also render many nuclear properties insensitive to much of the underlying dynamics. Attempts to better understand these underlying dynamics have led to an increasing interest in microscopic theories of the nucleus. Intermediate energy photonuclear reaction studies have proved their worth in this area, not only in verifying the general validity of the shell model (e.g. in extracting sin-

gle particle wave functions) but also in providing powerful tests of the microscopic models. It is within this context of improving our understanding of the nucleus at this microscopic level that the work reported in this thesis should be viewed. In contrast to the phenomenology of the shell model, where the nuclear potential well can be freely chosen, the input for microscopic theories is generally much more fundamentally constrained. A good example of this is Hartree-Fock theory, where a mean field, similar in nature to the shell model potential, is not 'pulled out of thin air' but rather derived from some realistic nucleon-nucleon potential. It is generally accepted that the nucleon-nucleon interaction is mediated via the exchange of virtual mesons. Many microscopic theories include these mesonic degrees of freedom explicitly and various coupling constants, form factors and propagators are used as inputs. It has also been shown that the explicit inclusion of Meson Exchange Currents (MEC) is necessary to describe some photonuclear reactions, i.e. they cannot be explained in conventional nuclear theory which projects onto the purely nucleonic components of the Hilbert space. Another interesting question which can only be answered through a microscopic approach is the role of isobars, in particular the $\Delta(1232)$, in nuclei. Experiments suggest the Delta constitutes a few per cent of the nuclear wave function and certainly plays an important role in reaction mechanisms in the resonance bombarding energy region. Nuclear pion photoproduction forms an important part of these studies. Given the good knowledge of free pion photoproduction, one can learn, by studying the nuclear case, about medium modifications, thus testing our understanding of Delta and pion propagation in the nucleus. The next section reviews previous studies of the process.

1.2 Previous Data

Although nuclear pion photoproduction has been extensively surveyed near threshold, the aim of these experiments was primarily to study exclusive (γ, π) reactions where the residual nucleus is in a definite state and no nucleon emission has occurred. These reactions are very sensitive to nuclear structure effects and it was indeed to probe these effects that the experiments were performed. For an extensive review of this area of the field the reader is referred to reference [Nag91].

In the Delta excitation region, where higher photon energies are involved and at least one nucleon is normally emitted in addition to the pion, the sensitivity to nuclear structure diminishes and one is looking more at the modifications of the free production process by the nuclear medium. In this area, the data are sparse and those that do exist are either of a single arm (inclusive) nature or of low resolution. All the data suffer from restricted kinematics. Each experiment is reviewed as follows.

The Tokyo Data

Homma *et al.* performed inclusive proton photoproduction measurements on Beryllium and Carbon using tagged photons at the Tokyo 1.3 GeV synchrotron [Hom83]. The photon energy range was 340 to 580 MeV, tagged with a 10 MeV resolution. Protons were detected by a spectrometer set to cover the angular range θ_p=25° ± 5° and a momentum range from 300 to 1100 MeV/c. Results were presented as double differential cross sections, $\frac{d^2\sigma}{d\Omega_p dp_p}$, versus proton momentum. The results for Carbon are shown in figure 1.1. The momentum spectra shown can be fitted to two Gaussians. The natural explanation of this structure is that the high energy peak is due to proton knockout as part of the quasi-deuteron process and the lower peak is due to quasi-free pion production, where the pion is undetected. The Gaussian fits allow the energy dependence of the two processes to be determined and Delta resonance behaviour is found in the latter, as expected.

The Bonn Data

Arends *et al.* performed an inclusive charged pion photoproduction experiment on ^{12}C using tagged photons at the Bonn 500 MeV synchrotron facility [Are82]. The photon range was from 200 to 390 MeV, tagged with a 10 MeV resolution. A pion spectrometer ($\Delta\Omega$=80 msr) recorded data for positive and negative pions at four angular settings, $\bar{\theta}_\pi$=48, 72, 108 and 128°. The pion energy threshold, T^π_{min} = 40 MeV, was quite high. The data were presented as double differential cross sections, $\frac{d^2\sigma}{d\Omega_\pi dT_\pi}$, versus pion energy and compared to results obtained using the cascade code PIKI which assumes that the process is essentially a quasi-free reaction followed by final state interactions. Reasonably good agreement was obtained as can be seen from the comparison (solid line) shown in figure 1.2.

The MIT-Bates Data

The MIT-Bates experiment represents one of only two exclusive coincidence studies previously performed on the pion photoproduction reaction. L.D. Pham *et al.* made $(\gamma, \pi^-\mathrm{p})$ measurements on oxygen [Pha91]. The experiment used a bremsstrahlung photon beam with end-point energy E_γ = 360 MeV. Pions were detected using the 5.1 msr Bigbite magnetic spectrometer, which was positioned at two settings, θ_π= 64 and 120°. Protons were detected at the conjugate angles, θ_p= 40 and 20°, by an array of plastic scintillator telescopes, which measured proton energy and out of plane angle. The analysis allowed the ground and 6.2 MeV states in ^{15}O (i.e. p-shell removal states) to be resolved and data were presented as double differential cross sections, $\frac{d^2\sigma}{d\Omega_\pi d\Omega_p}$, as a function of proton out of plane angle with pion energy being integrated out. A 30 MeV lower energy threshold was applied to the proton measurements. The data generally suffered from low statistics and both the bremsstrahlung beam and high electron background at forward angles led to complexities in the analysis. The data are shown in figures 1.3, where they are compared to calculations made using the Distorted Wave Impulse Approximation (DWIA) code THREEDEE [Cha77]. The main feature found was that the forward pion angle data were dramatically lower than predicted.

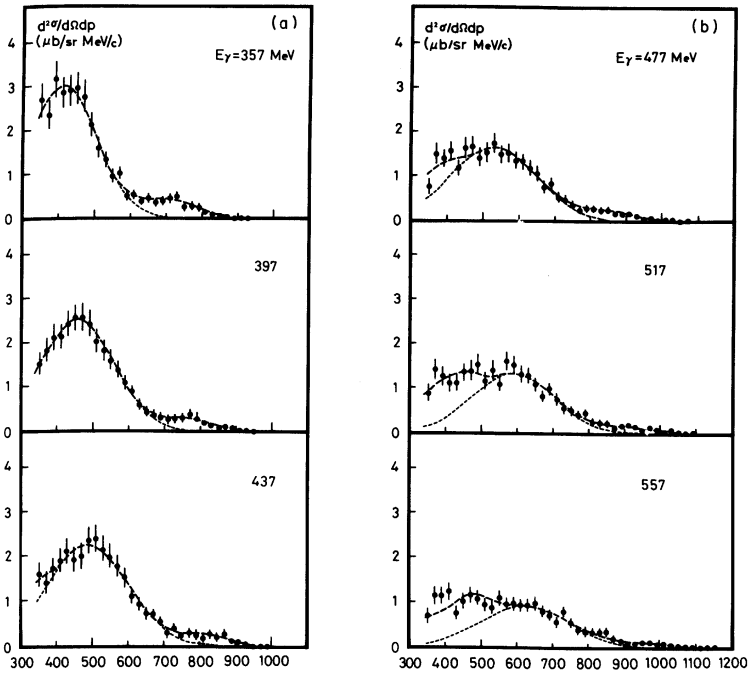

Figure 1.1: *Inclusive proton momentum spectra from the Tokyo data*

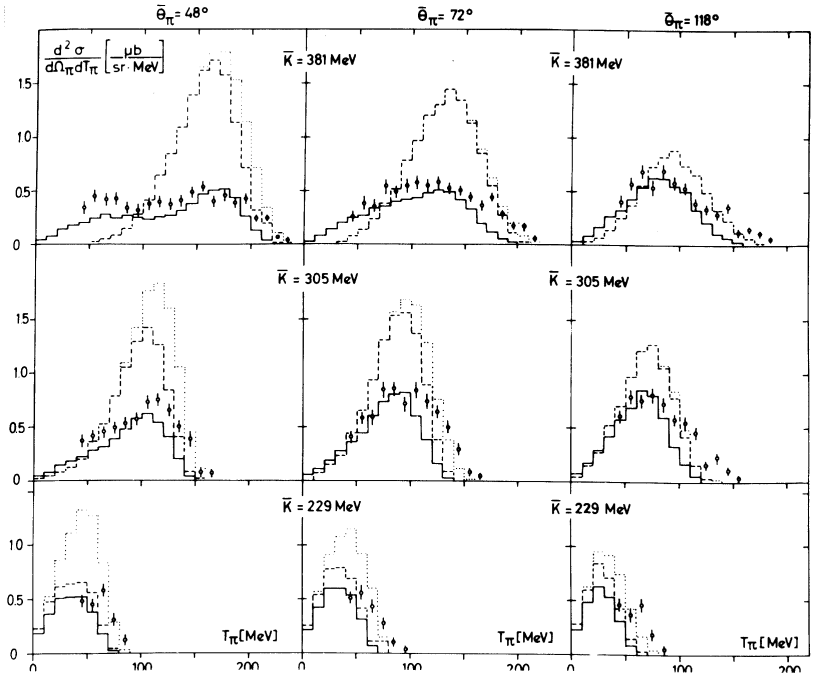

Figure 1.2: *Comparison of Bonn data with the cascade code PIKI (solid line)*

The Tomsk Data

Perhaps the highest quality data published to date are those provided by Glavanokov *et al.* [Gla79a]. They performed an exclusive $(\gamma, \pi^- \mathrm{p})$ measurement on Carbon-12 using a bremsstrahlung photon beam produced at the Tomsk electron synchrotron. Three end point energies of E_γ= 350, 370 and 390 MeV were used. Pion energies were determined by measuring their range in a copper absorber and proton energies by time of flight measurements. This gave pion and proton acceptances of 40-180 MeV and 50-190 MeV respectively. The measurement of the pion was performed at 120° and of the proton at 20°. Both detectors were in the reaction plane. The excitation of the final system was measured with a resolution between 6 and 17 MeV. The data were presented as three-fold differential cross sections, $\frac{d^3\sigma}{dT_p d\Omega_\pi d\Omega_p}$, versus proton energy. The data were split into two sets corresponding to residual nucleus excitation energies E_X <10 MeV and 10 MeV< E_X <40 MeV, corresponding to removal from $\mathrm{p}_{3/2}$ and $\mathrm{s}_{1/2}$ shells respectively. The data and a comparison to calculations made using the DWIA code of Li, Benhold and Wright [Li93] are shown in figure 1.4. The non-local DWIA predictions are represented by the solid line and good agreement with the data points is found although a problem remains in describing the $\mathrm{s}_{1/2}$ shell data.

The Present Experiment

The present experiment constitutes a significant improvement over all the above. It offers a fully exclusive measurement of the $^{12}\mathrm{C}(\gamma, \pi^+\mathrm{n})$ reaction over a wide region of phase space. Photons in the range 150-800 MeV, tagged with a 2 MeV resolution, allow a survey over the whole Delta resonance region. A missing energy resolution of 8 MeV allows for separation of p- and s-shell excitation regions in the residual system. The pion and neutron detectors cover a wide angular range, θ_π=50-130° and θ_n=10-150° with good resolution. The detector thresholds are low, T^π_{min}=20 MeV and T^n_{min}= 15 MeV, with a maximum pion detection energy of 180 MeV. All the above facts taken together lead to the conclusion that sensitive tests of theoretical models should be possible.

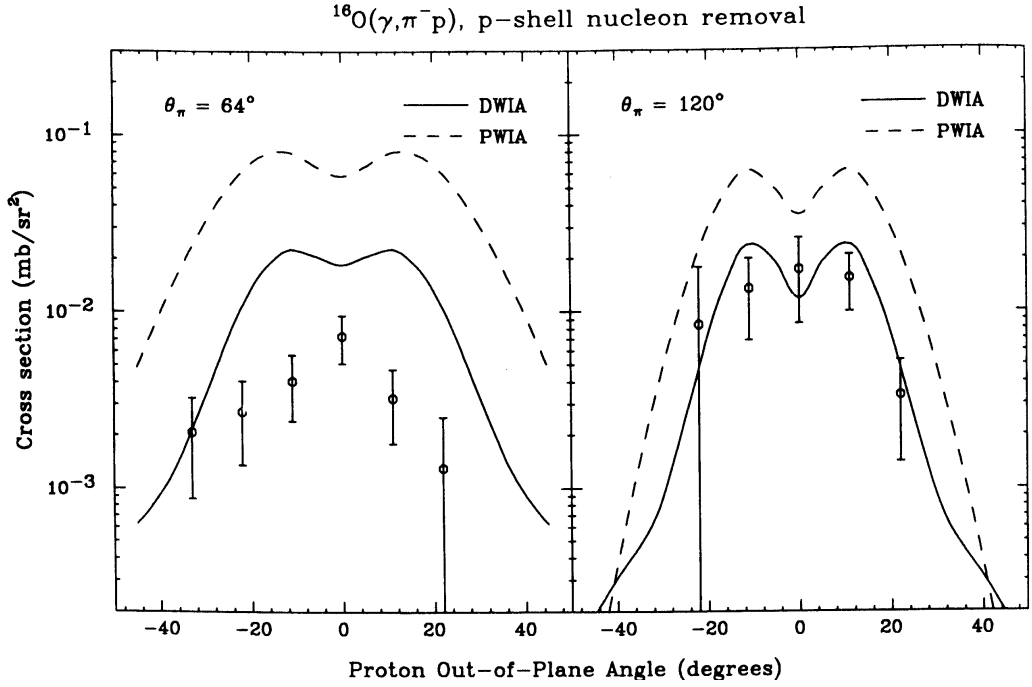

Figure 1.3: *Comparison of Bates data with the THREEDEE DWIA prediction*

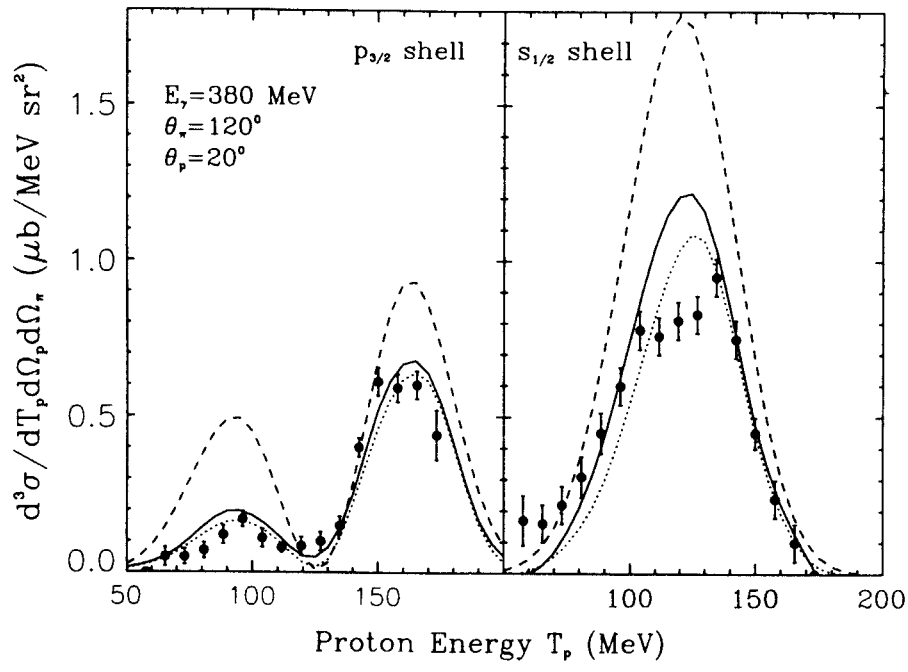

Figure 1.4: *Comparison of Tomsk data with a DWIA prediction (solid line)*

Chapter 2

Theoretical Framework

2.1 Photoabsorption

Photoabsorption is a process in which the electromagnetic field of the photon couples to the charge and current of the nucleus inducing a transition. The energy and momentum of the absorbed photon are shared amongst the constituents of the final state. The total photoabsorption cross section versus photon energy is shown in figure 2.1. Different energy regions involve different dynamics of the nuclear system.

To describe the system more formally, a reference to classical electrodynamics can be made, where the electromagnetic interaction is expressed by the term:

$$-eJ_{\mu}A^{\mu} \tag{2.1}$$

in the Lagrangian density of the 'field + charge' system [Ber71]. The 4-potential of the field is denoted A^{μ} and the particle current density 4-vector is denoted J_{μ} and satisfies the continuity equation:

$$\partial_{\mu}J^{\mu} = 0 \tag{2.2}$$

which expresses the principle of conservation of charge.

Expressed quantum mechanically, dynamical variables are replaced by operators and the initial nuclear system is described by the state vector Ψ_i, which is an eigenstate of the Hamiltonian H:

$$H\Psi_i = E_i\Psi_i \tag{2.3}$$

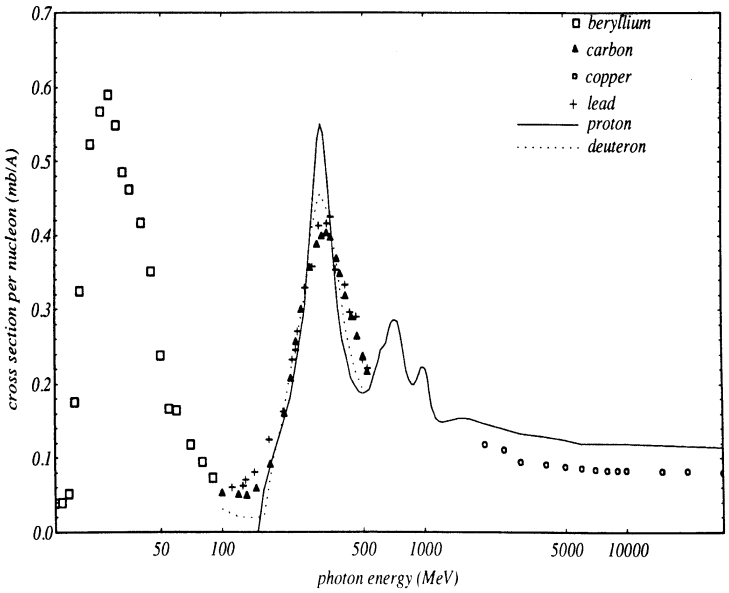

Figure 2.1: *The total photoabsorption cross section*

where E_i is the energy of the nuclear system. The presence of the photon introduces an interaction term into the Hamiltonian of the form,

$$V = e \int J_\mu A^\mu d^3x \tag{2.4}$$

This term is responsible for the time development of the system. Due to the weakness of the interaction, transitions can be described using perturbation theory. To first order, the transition rate from initial state Ψ_i to final state Ψ_f is given by Fermi's Golden Rule:

$$w_{i\to f} = \frac{2\pi}{\hbar}|V_{fi}|^2 \rho_f \tag{2.5}$$

where ρ_f is the density of final states and V_{fi} is the matrix element of the interaction operator between initial and final states.

$$V_{fi} = < f|V|i > \tag{2.6}$$

$$= e \int (J_{fi} A) d^3x \tag{2.7}$$

$$J_{fi} = < \Psi_f|J|\Psi_i > \tag{2.8}$$

where J_{fi} is referred to as the *transition current.*

Photonuclear reactions can be used to test theoretical predictions of the transition current. The initial and final states, Ψ_i and Ψ_f, involve nucleons, mesons and resonances and the current operator includes terms involving all of these, viz,

$$J = J^{\text{nucleons}} + J^{\text{mesons}} + J^{\text{resonances}} \tag{2.9}$$

Conventional nuclear physics, however, uses the subspace of nucleons only. Using the formalism of Gari and Hebach [Gar81], where the wave functions in the nucleonic subspace are denoted χ_i and χ_f and the operator projecting out this space is $(\eta + \mathrm{Q})$, one obtains the following expressions:

$$\begin{aligned}
\Psi_{i,f} &= (\eta + Q)\chi_{i,f} && (2.10)\\
V_{fi} &= <\Psi_f|V|\Psi i> && (2.11)\\
&= <\chi_f|(\eta + Q)^\dagger V(\eta + Q)|\chi_i> && (2.12)\\
&= <\chi_f|V^{eff}|\chi_i> && (2.13)
\end{aligned}$$

The interaction operator has been replaced by an effective one in the nucleonic subspace. The effective operator can be expressed as an expansion in one-, two-, three- etc. body terms. In terms of the current operator, J, the many body terms are collected into a single exchange term J_{EXC}:

$$\begin{aligned}
V^{eff} &= V^{eff}_{\text{one-body}} + V^{eff}_{two-body} + ... && (2.14)\\
J^{eff} &= J^{eff}_{\text{one-body}} + J^{eff}_{EXC} && (2.15)
\end{aligned}$$

Photoabsorption reactions essentially measure the transition current thus revealing the associated nuclear dynamics. When discussing photoabsorption it is necessary to specify the energy range. This is because the scale to which a photon is sensitive is of the order of its wavelength. Low energy photons ($\mathrm{E}_\gamma < 20\,\mathrm{MeV}$) tend to be sensitive to the nucleus as a whole and hence excite collective states. Ultra-GeV photons at the other extreme probe the quark sub-structure of nucleons as in deep inelastic scattering. Indeed the success of the parton model in describing these reactions was one of the first pieces of evidence for the existence of quarks. In the intermediate energy range which is the domain of this work, viz. $100\,\mathrm{MeV} < \mathrm{E}_\gamma < 1\,\mathrm{GeV}$, the dimension being probed is that of the nucleon and

the inter-nucleon spacing thus one must expect the one- and two-body terms to play an important role in the reaction mechanisms.

One body terms describe processes where the photon interacts with a single nucleon, the rest of the nucleus being a spectator. The two body terms involve meson exchange and are influenced by the fact that nucleons in the nucleus are not independent but correlated. In the ground state these correlations are rapidly healed by Pauli blocking and the repulsive hard core of the nucleon-nucleon potential creates correlation holes in the otherwise independent particle wave function. The rapid healing of the wave function means that these short range correlations will only show up in the high momentum components of the wave function. Where energy is supplied by the photon, the Pauli blocking is overcome as the final state nucleons are promoted above the Fermi level. This induced meson exchange becomes very important in describing the reaction. This is done by using two-body or meson exchange currents (MEC) in the nuclear current operator. Some of these contributions are shown graphically in figure 2.2.

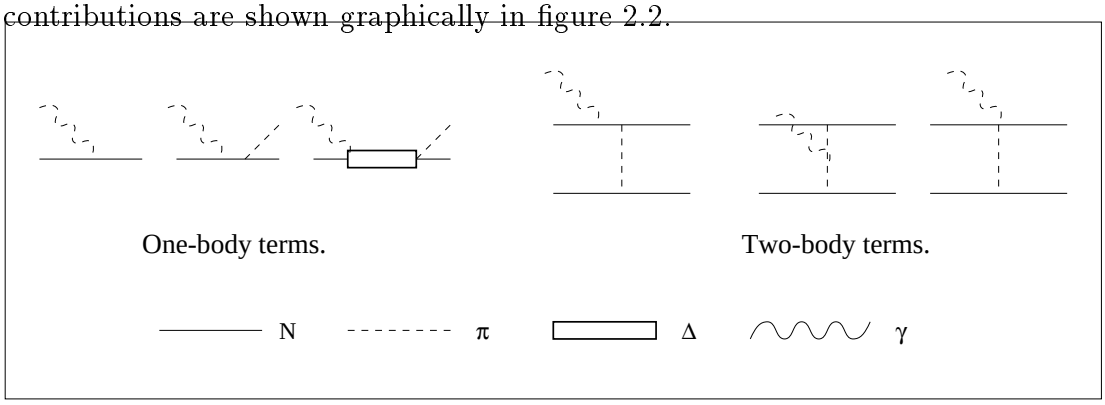

Figure 2.2: *One and two-body terms in photoabsorption*

The work of the Glasgow-Edinburgh-Tübingen collaboration has been to carry out a range of exclusive coincidence photoabsorption measurements viz. (γ,pN) , (γ, πN) etc. at the MAMI-B facility in Mainz and thus measure many channels relating to one and two-body mechanisms. Pion photoproduction is essentially a one body process analogous to nucleon knock out. Where nucleon knockout is suppressed in the resonance region, due to the high momentum mismatch, pion production in which the pion takes up the required momentum takes over.

2.2 Free Pion Photoproduction

Physically, free pion photoproduction involves the coupling of the electromagnetic field to the charge and magnetic moment of the nucleon. This induces the nucleon to radiate pions via the strong interaction. The cross section for the process as a function of incident photon energy is shown in Figure 2.3.

Figure 2.3: *Free charged pion photoproduction cross section*

It rises from threshold and exhibits resonant behaviour at $E_\gamma \approx 340\,\mathrm{MeV}$ (the Δ-region) and then flattens out with higher resonances being unresolved due to their large widths.

Being an electromagnetic process, one might expect it to be well understood; witness the triumphs of Quantum Electro-Dynamics (QED). There are problems however. The first is that the nucleon has a sub-structure due to its quark content, the dynamics of which are not solvable at low energy. If the nucleon were structureless (point-like), as the electron is, then one could express the γNN coupling with the simple transition current:

$$j^\mu_{\gamma NN} = \bar{u}' \gamma^\mu u \tag{2.16}$$

where $\bar{u}'$ and u are Dirac spinors representing the electron and γ^μ represents the Dirac matrices. In the nucleon, however, the underlying structure complicates matters; the nucleon can be seen as coupling to a cloud of virtual mesons which alter its charge distribution and magnetic moment. The transition current must then be expressed in the most general form allowed by symmetry requirements [Bil76]:

$$j^\mu_{\gamma NN} = \bar{u}'[F_1(Q)\gamma^\mu + F_2(Q)\sigma^{\mu\nu}k_\nu]u \tag{2.17}$$

where the structure information is contained in the Dirac and Fermi form factors, F_1 and F_2, which are functions of the momentum transfer to the nucleon. These functions are obtained experimentally and, for the proton at least, they are well known. The second problem is that the final state particles, the pion and nucleon, strongly interact. The strength of the interaction gives rise to rescattering effects. As the following sections will show the description of this aspect of the reaction relies heavily on phenomenology, specifically the use of pion scattering data.

All theories of pion photoproduction proceed from the same starting point [Noz90], a meson-baryon effective Lagrangian. The choice of Lagrangian should be simple and able to reproduce qualitatively a wide variety of elementary processes. The Lagrangian is in effect mocking up the underlying quark dynamics. Some guidance in the choice of Lagrangian can be found in the underlying symmetries of Quantum Chromo-Dynamics (QCD) and a good discussion of this is given in a report by E. Oset [Ose82]. The pseudo-vector (PV) coupling of pion and nucleon has become a common choice as it satisfies chiral symmetry and the Partially Conserved Axial Current (PCAC) hypothesis. The interaction Lagrangian has the form,

$$\mathcal{L}_{\pi\mathrm{NN}} = i\frac{f}{m}\bar{\mathrm{N}}\gamma_\mu\gamma_5\tau^\alpha\mathrm{N}\partial_\mu\pi^\alpha \tag{2.18}$$

where coupling constants are chosen to fit πN and $\pi\pi$ scattering in the tree approximation i.e. no Feynman diagrams involving loops can be included. The electromagnetic coupling is introduced by minimal substitution:

$$\partial_\mu \rightarrow \partial_\mu - ieA_\mu \tag{2.19}$$

thus ensuring gauge invariance. For a PV πN coupling the interaction Lagrangian

becomes,

$$\mathcal{L}_{PV} = \mathcal{L}_{\pi NN} + \mathcal{L}_{\gamma NN} + \mathcal{L}_{\gamma\pi\pi} + \mathcal{L}_{\gamma\pi NN} \tag{2.20}$$

the terms of which are shown diagrammatically in Figure 2.4.

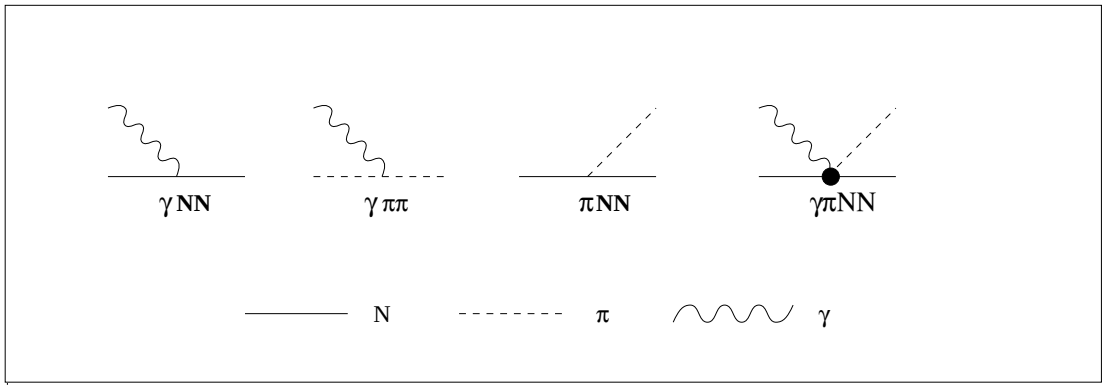

Figure 2.4: *Vertices associated with interaction terms in the PV πN Lagrangian*

From this Lagrangian, the amplitude for the process in the Born approximation is given by constructing the lowest order Feynman diagrams as shown in figure 2.5.

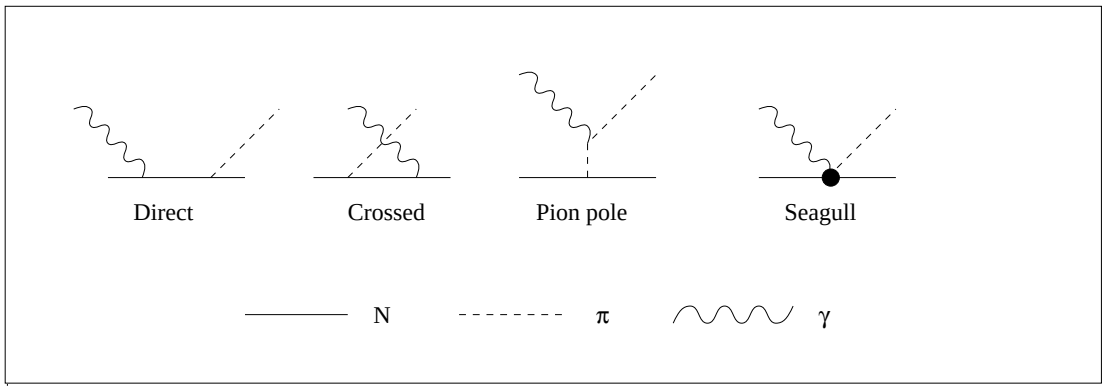

Figure 2.5: *Born terms in the free pion production amplitude*

These are referred to as the Born terms and they are dominant at low energy and for charged pion production still provide 50% of the cross section in the Δ resonance region. Going beyond the Born approximation involves the inclusion of resonant and multiparticle intermediate states in the amplitude. The dominant non-Born contribution for $E_\gamma \leq 500\, MeV$ is that of the P_{33} pion-nucleon resonance

- the Delta. In the following sections, different models for the non-Born part are reviewed. Before doing this it is necessary to introduce some notation used to describe the general form of the amplitude and also the concept of unitarity relating to the photoproduction process.

2.2.1 The Elementary Amplitude

The $(\gamma, \pi\mathrm{N})$ process is represented in figure 2.6, which gives the standard notation for the various dynamical variables relating to the process.

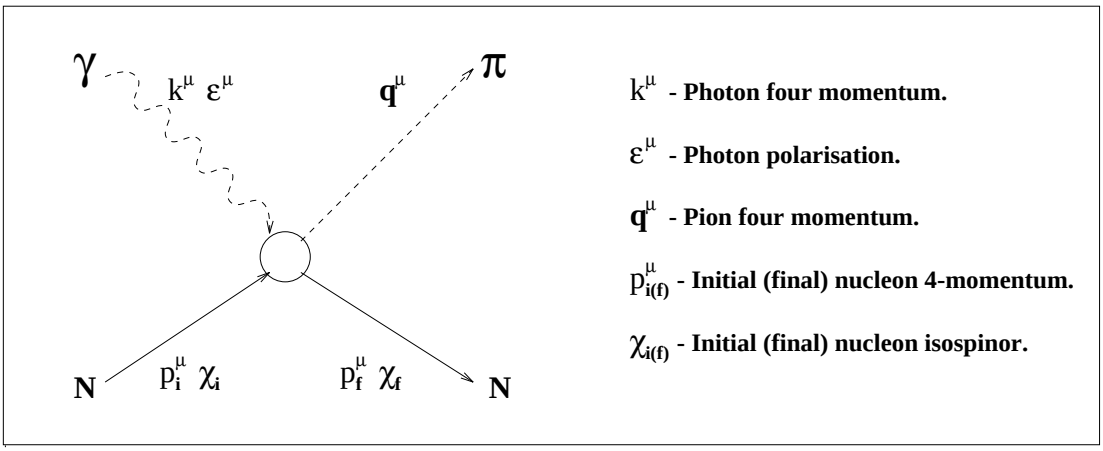

Figure 2.6: *Dynamical variables relating to pion photoproduction*

The first photopion production amplitude to gain recognition was that of Chew, Low, Goldberger and Nambu (CGLN) introduced in their classic paper of 1957 [Che57]. In this paper, they introduced notation which has become standard in describing the amplitude for pion photoproduction.

The most general form of the $\gamma N \to \pi N$ transition operator can be expressed as a linear combination:

$$t_{(\gamma,\pi)} = \epsilon^{\mu} J_{\mu}^{fi} \tag{2.21}$$

$$= \sum_{i} A_i M_i \tag{2.22}$$

of all the Lorentz invariants M_i which can be formed from the particle four-momenta, the Dirac γ-matrices and the photon polarisation ϵ^{μ}. There are four

linearly independent combinations and the representation chosen by CGLN (with P=(p_i + p_f)/2) was:

$$M_1 = i\gamma_5 \not\epsilon \not k \tag{2.23}$$

$$M_2 = 2i\gamma_5(P\cdot\epsilon q\cdot k - P\cdot kq\cdot\epsilon) \tag{2.24}$$

$$M_3 = \gamma_5(\not\epsilon q\cdot k - \not k q\cdot\epsilon) \tag{2.25}$$

$$M_4 = 2\gamma_5(\not\epsilon P\cdot k - \not k P\cdot\epsilon - iM\not\epsilon\not k) \tag{2.26}$$

The coefficients A_i are functions of the particle momenta of which there are only two independent Lorentz scalars. CGLN chose:

$$A_i = A_i(\nu,\nu_1)\ ;\ \nu = -P.k/M\ ;\ \nu_1 = -q.k/2M \tag{2.27}$$

There are four possible isospin channels: $(\gamma,\pi^+\mathrm{n})$,$(\gamma,\pi^-\mathrm{p})$,$(\gamma,\pi^0\mathrm{n})$ and $(\gamma,\pi^0\mathrm{p})$. An analysis of the systematics of the isospin dependence of the amplitude was first carried out by K. Watson in 1954 [Wat54]. He showed that the four isospin amplitudes could be expressed in terms of three independent functions, A_i^0, A_i^+, A_i^-. Thus the full description of the amplitude reduces to the evaluation of twelve (four times three) functions of ν and ν_1.

CGLN proceeded to do a non-relativistic reduction of the above operator in the barycentric (pion-nucleon) reference frame. The differential cross-section then takes the form,

$$\frac{d\sigma}{d\Omega} = \frac{q}{k}|<f|\mathcal{F}|i>|^2 \tag{2.28}$$

where, for a given isospin configuration, the transition operator takes the simplified form:

$$\mathcal{F} = i\sigma\cdot\hat\epsilon F_1 + \frac{\sigma\cdot q\sigma\cdot k\times\hat\epsilon}{|q||k|}F_2 + i\frac{\sigma\cdot kq\hat\epsilon}{|q||k|}F_3 + i\frac{\sigma\cdot qq\hat\epsilon}{q^2}F_4 \tag{2.29}$$

where $F_{1..4}$ are functions of photon energy and pion angle. This angular dependence can be expressed in terms of Legendre polynomials thus expressing the amplitude as a multipole expansion,

$$F_1 = \sum_{l=0}^{\infty}[lM_{l+} + E_{l+}]P'_{l+1}(x) + [(l+1)M_{l-} + E_{l-}]P'_{l-1}(x) \quad (2.30)$$

$$F_2 = \sum_{l=1}^{\infty}[(l+1)M_{l+} + lM_{l-}]P'_l(x) \quad (2.31)$$

$$F_3 = \sum_{l=1}^{\infty}[E_{l+} - M_{l+}]P''_{l+1}(x) + [E_{l-} + M_{l-}]P''_{l-1}(x) \quad (2.32)$$

$$F_4 = \sum_{l=2}^{\infty}[M_{l+} - E_{l+} - M_{l-} - E_{l-}]P''_l(x) \quad (2.33)$$

where $x = cos(\theta_\pi)$ and P'_l represent derivatives of the Legendre polynomials.

The amplitude is now expressed in terms of energy dependent multipoles, $M_{l\pm}$ and $E_{l\pm}$, transitions being initiated by magnetic and electric radiation respectively, leading to final states of orbital angular momentum l and total angular momentum $j = l \pm \frac{1}{2}$. Superscripts $(+,-,0)$ can be added to each quantity to denote the isospin amplitude involved. It is in terms of these multipoles that the amplitudes and data are most often compared. They provide some physical insight as the M_{1+} multipole, for instance, corresponds to an incident photon coupling to the nucleon to form a J=$\frac{3}{2}$ state which leads to an l=1 pion. The J=$\frac{3}{2}$ nature of the multipole is identical to that of the Delta nucleon resonance and one may expect this multipole to show correspondingly resonant behaviour as is found to be the case.

The second reason for expressing the amplitude in terms of these multipoles is that comparison with πN scattering data is possible. This is critical as calculation of the non-Born part depends on the use of this information. This can be seen explicitly in Watson's theorem where, for a given isospin configuration, the phase of a given multipole is shown to be the same for the (γ,π) and (π,π') processes.

2.2.2 Watson's Theorem

In his paper "Some general relations between the photoproduction and scattering of π-mesons" Watson [Wat54] derived some key qualitative properties of the photoproduction process. In particular, Watson applied unitarity of the S-matrix to derive an expression for the complex phases of the matrix elements of the production process. Watson states:

> ... the multipole matrix elements for photoproduction are essentially real quantities. Because of meson-nucleon scattering in the final state, the phases of the various meson partial waves are shifted relative to one another by the amount of the *scattering* phase shifts.

Thus we can view the $(\gamma, \pi\mathrm{N})$ process as a two step process; pion production followed by pion scattering in the final state. Watson's theorem can be derived from unitarity of the S-matrix:

$$SS^{\dagger} = 1$$

in conjunction with the dominance of the πN scattering channel over that of $\pi\mathrm{N} \rightarrow \gamma\mathrm{N}$. In the sections to follow, any reference to the imposition of unitarity should be understood as demanding that production multipoles are of the correct phase. Note that Watson's theorem is an explicitly on-shell concept as scattering is on-shell.

2.2.3 Beyond the Born Approximation

All models of pion photoproduction agree on the form of the amplitude in the Born approximation. Their individual characteristics become apparent in describing features beyond this. There are essentially three approaches to attaining the full pion photoproduction amplitude. Each relies heavily on pion scattering data as input. Thus they are all phenomenological in this sense. What is required is an amplitude that can easily be applied to nuclear calculations and this must be borne in mind when evaluating the various models. For example, the Dispersion Relations approach may claim a stronger physical basis as opposed to the more ad-hoc Effective Lagrangian technique. The latter, however, is more convenient for use in nuclear calculations and retains in a manifest way an insight into the underlying dynamics of the process. The Hamiltonian approach claims to have a natural extension off the mass shell, which is necessary when the process is studied inside the nuclear medium. Each technique is discussed in turn.

2.2.4 Dispersion Relations

Dispersion relations were first applied in optics in the Kronig-Kramer relation. Dispersion relations are related to Cauchy's Integral Theorem for analytic complex functions of a complex variable.

$$\oint_C \frac{f(z)}{z - z_0} dz = 2\pi i f(z_0) \tag{2.34}$$

Applied to pion photoproduction, they correspond to a statement of the analytic nature of the S-matrix. They were first used in the current context by Chew *et al.* in the CGLN paper discussed earlier [Che57]. A more rigorous analysis was made by Berends *et al.* in 1967 [Ber67]. The dispersion relation for a multipole amplitude is given as,

$$\begin{aligned} ReM_l(W) &= M_l^B + \frac{P}{\pi}\int_{M+m}^{\infty} dW' \frac{ImM_l(W')}{W' - M} \\ &\quad + \frac{1}{\pi}\sum_{l'}\int_{M+m}^{\infty} sW' K_{ll'}(W, W') ImM_{l'}(W') \end{aligned} \tag{2.35}$$

where $M_l^B(W)$ is the Born term (projected onto the multipole in question) as a function of W, the c.m.s. energy. The second term is called the direct term relating

to rescattering in the multipole in question. The kernel function $K_{ll'}(W, W')$ dictates the contribution from other pion partial waves. The key to solving these equations lies in the application of unitarity in the form of Watson's theorem i.e. the phase of the multipole amplitude is that of pion scattering. This is expressed:

$$ImM_l = ReM_l tan\delta_l^{\gamma\pi} \quad (2.36)$$

$$= ReM_l tan\delta_l^{\pi} \quad (2.37)$$

where δ_l^{π} is the (π, π') scattering phase shift. With these constraints, the dispersion relations become solvable.

Where the phases are small the Born terms will dominate. The success of this approach to pion photoproduction has been due to the fact that only the P_{33} (J=$\frac{3}{2}$, T=$\frac{3}{2}$) phase shift becomes large and hence dominates the dispersion integrals. The resulting M_{1+}^3 multipole is show in figure 2.7.

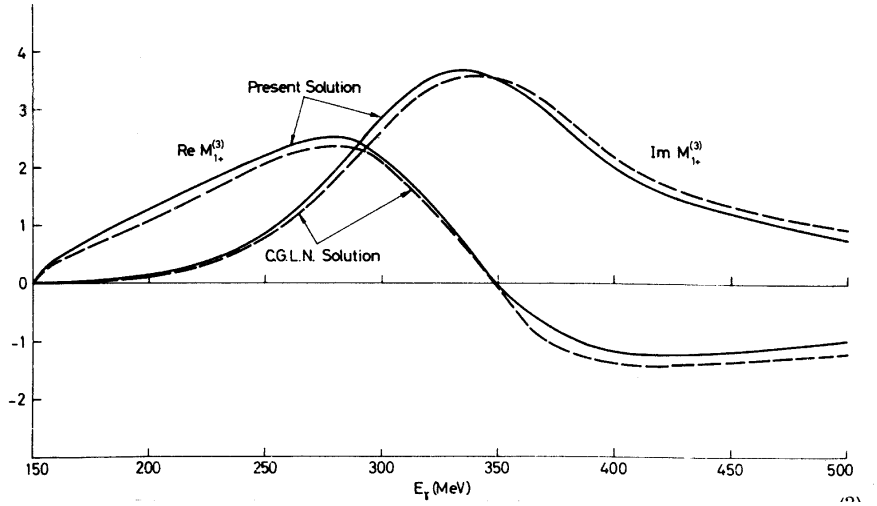

Figure 2.7: *The M_{1+}^3 multipole as predicted by dispersion relations*

A note on the application of the dispersion theory result to nuclear applications is worthy here. Free pion production acts on a stationary nucleon whereas inside the nucleus, nucleons acquire Fermi motion and a frame independent expression for the amplitude is desirable to facilitate calculations. Multipoles are, however, defined in the barycentric frame and one must transform the amplitude into the invariant form $\sum A_i M_i$ discussed earlier. This is complex and physical insight into

the various components of the amplitude is lost. It is, however, the method used by Glavanokov in his nuclear calculations [Gla79].

2.2.5 The Effective Lagrangian Approach

The Effective Lagrangian approach is more ad-hoc than the above dispersion theory. The non-Born part is treated by explicit inclusion into the Lagrangian of new intermediate state particles. As stated above, the non-Born part is dominated by the P_{33} $\pi-$N resonance - the Delta $\Delta(1232)$. The Delta is included as an explicit degree of freedom into the Lagrangian and coupling constants, form factors and widths are chosen to fit πN scattering data and indeed the photomeson data itself. These resonant additions to the amplitude are depicted by the Feynman diagrams in figure 2.8. The first two terms i.e. (a) and (b) represent the direct and crossed Delta pole terms. Term (c) is a rescattering term and should not be included as it is implicit in the first term. This is another way of saying that the couplings used in the model are for that of a dressed Delta.

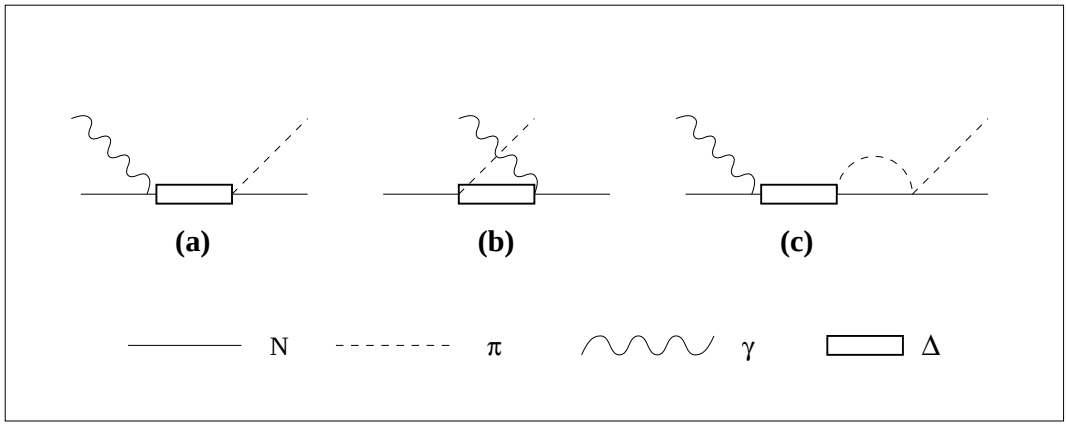

Figure 2.8: *The contribution of the Delta to the pion photoproduction amplitude*

As it stands, the amplitudes are all real and final state rescattering must be properly taken into account by unitarising the amplitude i.e. each multipole must be given the correct phase as dictated by πN scattering. This procedure is complicated by the fact that each multipole may contain a non-resonant (Born) and a resonant piece. The correct procedure for unitarisation was developed by

Olson [Ols74] who showed that one must apply a prescribed phase to the resonant term in the amplitude.

Blomqvist and Laget [Blo77] pursued this approach in 1977 with the aim of finding a convenient yet accurate transition operator for use in nuclear calculations. They performed a non-relativistic reduction of the PV Lagrangian to get an operator valid to order $(p/m)^2$ in any frame of reference. The Δ, being a J=$\frac{3}{2}$ particle, is described by Rarita-Schwinger spinors. There are two γNΔ couplings with constants G_1 and G_2. The second is neglected in the B-L model due to its small effect on the total cross section (although specific multipoles are very sensitive to it). The $\pi\Delta$N coupling constant G_3 and the Δ mass M and width Γ are extracted from pion scattering data. The values obtained are:

$$\begin{aligned} M &= 1231\text{MeV} \\ \Gamma &= 109(\frac{|q|}{|q_\Delta|})^3 \frac{M}{Q} \frac{1+(R|q_\Delta|)^2}{1+(R|q|)^2} MeV \\ G_3 &= \frac{g_3}{m_\pi} \sqrt{\frac{1+(R|q_\Delta|)^2}{1+(R|q|)^2}} MeV^{-1} \\ R &= 0.00552 MeV^{-1} \\ g_3 &= 2.13 \end{aligned}$$

This fit reproduces the (3,3) scattering phase shifts. The $\gamma\Delta$N coupling constant, G_1, was determined by a fit to charged pion production data:

$$G_1 = g_1 \frac{M+m}{m_\pi} \sqrt{4\pi/137}, \qquad g_1 = 0.282$$

Using the above parameters, the various Feynman diagrams involving an intermediate Delta can be calculated. These amplitudes are added to the Born terms and the cross section is calculated. Figure 2.9 shows the predicted cross sections in the B-L model.

Davidson, Mukhopadhay and Wittman (DMW) extended the B-L model in 1986 [Wit86]. They included the u-channel crossed Δ term and the second γNΔ coupling. The effect was noticeable in certain multipoles but the predicted cross section remained largely the same as that of the B-L model.

Figure 2.9: *Pion production cross sections predicted by B-L model (solid line)*

2.2.6 The Hamiltonian Approach

The latest addition to the family of models describing free pion photoproduction is that of Nozowa, Blankleider and Lee (NBL) [Noz90]. Their model is similar to the Effective Lagrangian Approach in that the Δ is added to the Hamiltonian as an explicit degree of freedom. The difference between the two models lies in their treatment of scattering in the πN final state. The Effective Lagrangian technique applied Watson's Theorem to unitarise the amplitude i.e. putting in 'by hand' the phases of the multipoles. In the Hamiltonian approach a scattering formalism is constructed which reproduces on-shell πN scattering phase shifts. The advantage of this model is that it has a natural extension off-shell whereas Watson's Theorem is only defined on-shell. If off-shell effects are important in nuclear calculations (and the authors claim they can account for 50% of the cross section) then this model may come to the fore.

2.3 Nuclear Structure and Properties of Carbon

Before proceeding with a review of nuclear pion photoproduction, it is necessary to introduce concepts and nomenclature relating to the nucleus and in particular to Carbon-12, the target used in this experiment.

As pointed out in the introduction chapter, the bulk of nuclear properties can be discussed in terms of the independent particle motion of the nucleons in a mean field. The form of this potential, an important contribution to which is the spin-orbit term, generates the observed shell structure of the nucleus. The states available to nucleons are denoted by the single particle wave functions ϕ_{nlj}, where n is the primary quantum number defining the number of nodes in the radial wave function, l is the orbital angular momentum of the state and j is the total angular momentum arising from the coupling of this orbital angular momentum to the nucleon spin s. An orbit is often described in the spectroscopic notation nL_j where L is the letter corresponding to the l value. For example the state $1\mathrm{p}_{3/2}$ corresponds to n=1, l=1 and j=3/2. The states are filled in a definite order as dictated by the energy level scheme. Each state has a degeneracy of $(2j+1)$ for both protons and neutrons. In Carbon-12, the $1\mathrm{s}_{1/2}$ and $1\mathrm{p}_{3/2}$ proton and neutron shells are filled as shown in figure 2.10.

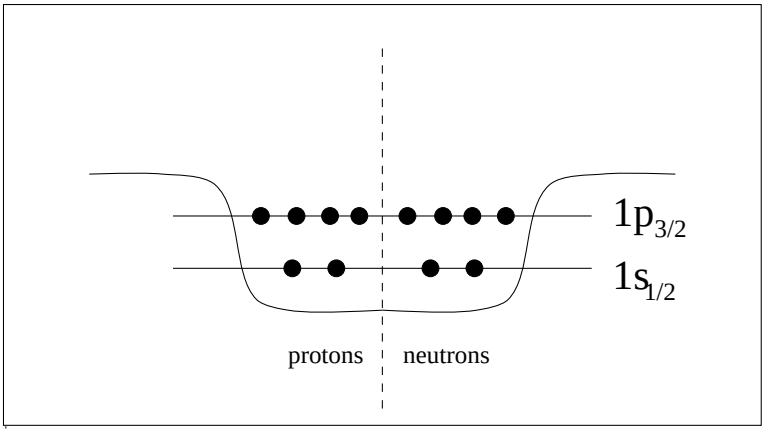

Figure 2.10: *The shell structure of Carbon-12*

In the ^{12}C$(\gamma, \pi^+$n) reaction, a proton is removed from the nucleus leaving (in the absence of hard final state interactions) the Boron-11 nucleus in its ground or an excited state. Information about this final state is given by an observable called the missing energy,

$$E_{miss} = E_\gamma - T_n - T_\pi - T_{recoil} \quad (2.38)$$

$$= Q + E_X \quad (2.39)$$

where E_X is the excitation energy of the residual system and the Q value is simply:

$$Q = M_{^{11}B} + M_n + m_{\pi^+} - M_{^{12}C} \quad (2.40)$$

$$= 156.8\, MeV \quad (2.41)$$

The excitation levels of ^{11}B are shown in figure 2.11 [Led78]. It is of interest to look at the ^{12}C$(e, e'$p) reaction where a proton is also removed from the nucleus. In this case no pion is produced and the Q value for the reaction is 16 MeV. The two missing energy spectra in figure 2.12 were produced by the Mainz A1 collaboration [Mai94]. Figure 2.12(left) shows a high resolution spectrum where the individual excited states in the residual Boron nucleus can be picked out. In figure 2.12(right), which has lower resolution, these states are unresolved but two excitation regions are discernible. The first region at excitation energy $E_X < 10\, MeV$ corresponds to the case where a p-shell proton has been removed whereas the higher region (10 MeV$< E_X <$40 MeV) corresponds mainly to s-shell removal. A resolution of less than 10 MeV is required to resolve the two regions.

When calculating cross sections, theorists make use of the quantity S_{l_j} known as the spectroscopic factor, which is defined as the overlap of the initial nucleus with a nucleon removed and the final nuclear state [Li93]. It represents the fact that the nucleons are not in fact independent and the occupancy of the shells is less than 100%. For example for Carbon-12 the spectroscopic factor for the $1p_{3/2}$ shell, $S_{1p_{3/2}}$, equals 2.6 representing the fact that 2.6 out of the 4 protons in the shell take part in the reaction.

Figure 2.11: *Excitation scheme for Boron-11 [Led78]*

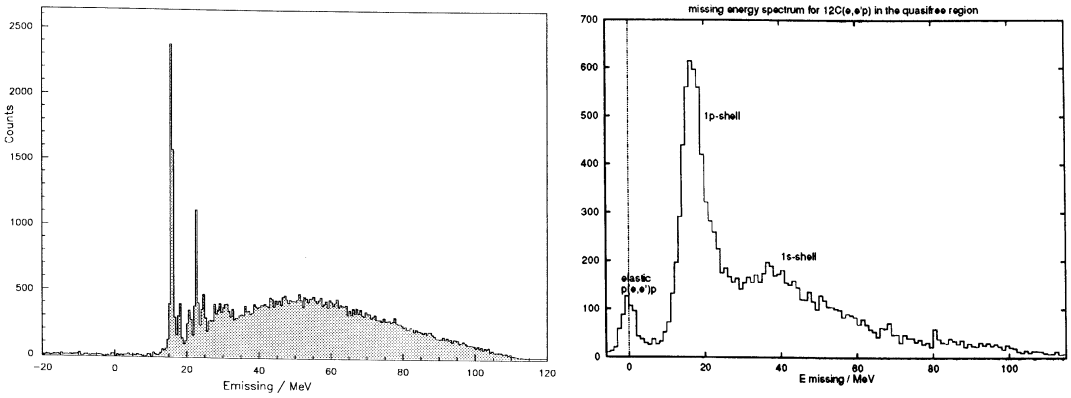

Figure 2.12: *Missing energy spectra from the* $^{12}C(e, e'p)$ *reaction [Mai94]*

2.4 Nuclear Pion Photoproduction

Free pion photoproduction provides a good starting point for the study of the process inside the nucleus. There are, however, many new effects generated by the medium which modify the process. In this section, these modifications are reviewed and theoretical models which include at least some of these effects are discussed.

2.4.1 Medium Modifications

The various medium modifications to the elementary production amplitude are detailed below.

Fermi Motion

In contrast to free pion production on a proton, the nucleons in a nucleus are in motion. Figure 2.13 shows the momentum distribution of p-shell nucleons in ^{12}C [Ste87]. This motion produces a basically kinematical effect which results in a broadening of the observed resonance in the cross section. In effect, the free cross section is folded with the momentum distribution. In exclusive measurements, where nucleons from a given shell can be isolated, the theoretical predictions will be sensitive to the single particle wave functions used in the calculations.

Pauli Blocking

The Pauli Exclusion Principle prohibits any two identical fermions from occupying the same state. This is expressed in the antisymmetry of the nuclear wave function with respect to identical particle interchange. Pion photoproduction imparts energy and momentum to the struck nucleon. The process will be blocked, however, if the resultant state is already occupied by another nucleon. The best picture of this effect is given in the Fermi gas model of the nucleus where states are fully occupied below the Fermi energy ϵ_F and empty above it. This is shown schematically in figure 2.14. In order to proceed, the production process must give the nucleon enough energy to place it above the Fermi level. The resultant

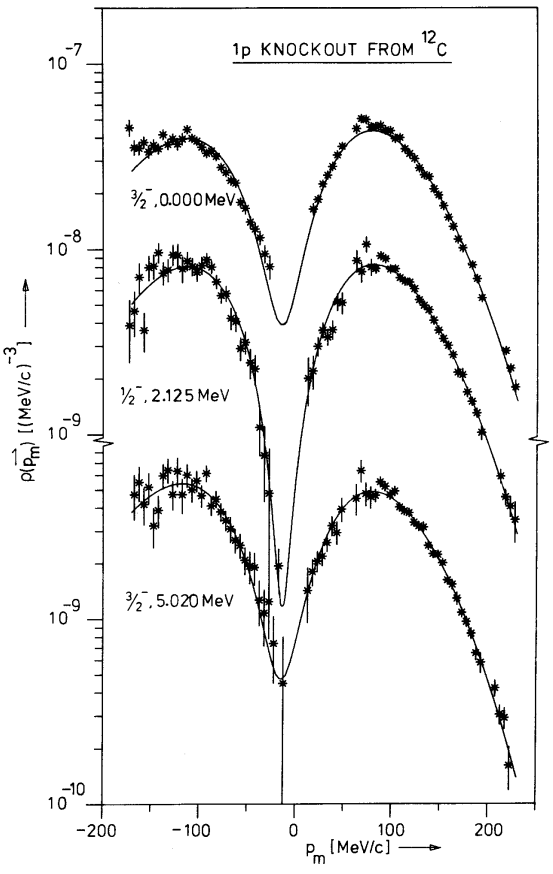

Figure 2.13: *The p-shell momentum distribution in Carbon-12 [Ste87]*

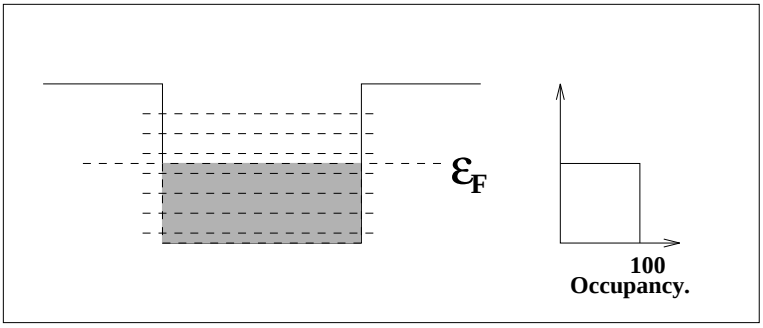

Figure 2.14: *The nucleus in the Fermi gas model*

reduction of the cross section is greatest near threshold but still significant at resonance due to the fact that the nucleon gains only a small fraction of the available energy due to it being seven times more massive than the pion.

Delta-propagation

The most interesting medium modification in the resonance region relates to Delta propagation. In the free case, the excited Δ decays to a nucleon and a pion with a branching ratio of 100% and a decay time expressed as its width Γ=110 MeV ($\approx 10^{-23}$ s). The nuclear medium complicates matters considerably. Firstly, Pauli blocking reduces the phase space available to the decay products thus narrowing the width of the resonance. Counterwise, the medium facilitates new decay modes into purely nucleonic final states viz. ΔN$\rightarrow$NN as shown in figure 2.15. These absorption mechanisms tend to broaden the resonance and remove strength from the pion production channel.

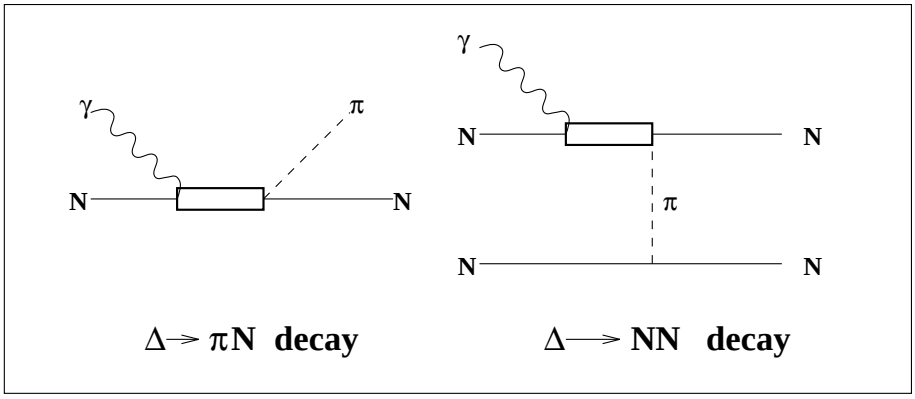

Figure 2.15: *Decay modes of the Delta in the nuclear medium*

An interesting question relating to the resonance is that of the peak position - is it shifted in the medium? A comparison with pion absorption, which is dominated by Δ formation, is illuminating. Here, a flattening of the resonance is accompanied by a downward shift of about 40 MeV. This has been ascribed to coherent multiple scattering of the pion [Ose82] which is favoured due to the longitudinal nature of the πNΔ coupling i.e. the term $S{\cdot}q$ in the transition operator. In photoproduction, the relevant coupling is for γNΔ which is transverse ($S\times$ k). Coherent forward

scattering is suppressed and the associated damping and downward shift are not expected, as is observed in the data. This is displayed in figure 2.16.

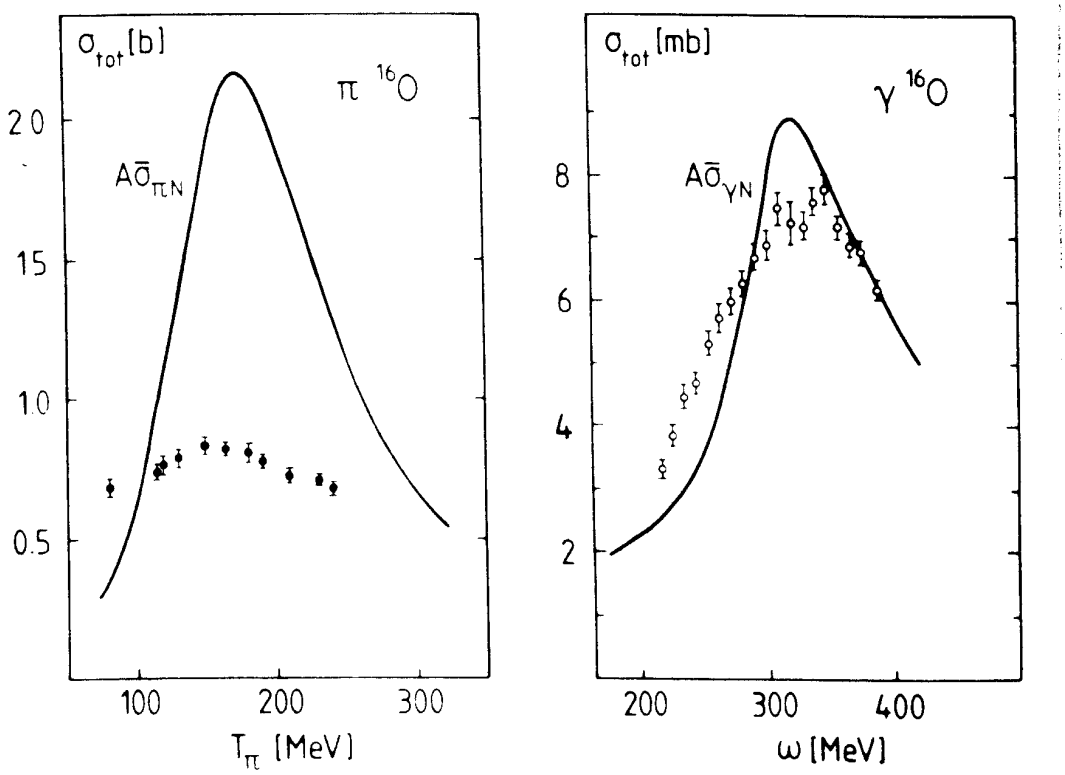

Figure 2.16: *The Delta in pion versus photon absorption*

Polarisation Effects

If one looks at the photoelectric (pion pole) Born term in figure 2.5 one might well expect it to be sensitive to pion propagation. Pion propagation is modified in the medium by polarisation effects. The pion mean path becomes different from that given by the Yukawa form of the pion field. The pion polarises the medium by inducing ph or Δh excitations [Car92a]. This polarisation is shown diagrammatically in figure 2.17.

Such effects can only be included in a full many-body microscopic model such as that of Carrasco, Oset and collaborators [Car92a].

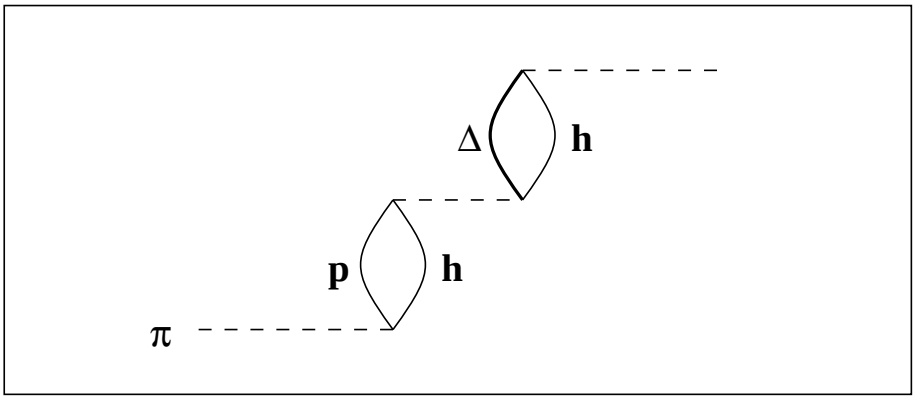

Figure 2.17: *Medium polarisation effects to the pion propagator*

Screening

Screening is an important effect in pion absorption where the interaction probability between pion and nucleus is so large that most of the pions are absorbed at the surface. The nuclear interior is screened as the pion flux falls off rapidly. This surface absorption accounts for the $A^{\frac{2}{3}}$ mass dependence of the cross section. Photoabsorption is a much weaker process and the reduction in photon flux through the nucleus is negligible. The whole nuclear volume is probed and the cross section shows a correspondingly linear A dependence. The role of screening in the two processes is illustrated in figure 2.18

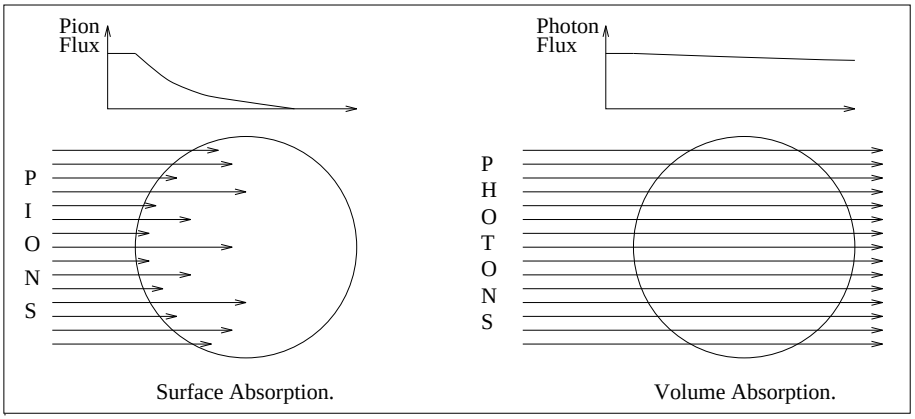

Figure 2.18: *Screening in pion and photon absorption*

Final State Interactions

Final State Interactions (FSI) describe the interaction of the produced particles, in this case the pion and nucleon, with the residual nucleus. The concept is non-trivial in that it assumes a clear separation of the initial process and the exit of the final state particles. Especially where medium modifications to the elementary process are being discussed, there is not always a clear divide and care must be taken to avoid double counting.

The classic technique for describing FSI is via the use of optical potentials. The plane wave of the exiting particle is distorted by the potential thus reproducing scattering of the particle. The imaginary part of the potential effects a damping of the wave reflecting the removal of the particle from the elastic channel, by absorption or inelastic scattering. The potential is energy dependent and parameters are extracted from scattering data. A typical nucleon-nucleus potential might have the form [Sch82],

$$\begin{aligned} U(r) &= U_{Coul}(r) - V f_0(r) - iW f_w(r) \\ &\quad + \frac{2.00}{r}\left[V_{SO}\frac{d}{dr}f_{vSO}(r) + iW_{SO}\frac{d}{dr}f_{wSO}(r)\right]\vec{L}\cdot\vec{\sigma} \end{aligned} \tag{2.42}$$

where V and W are the real and imaginary potentials with the Woods-Saxon form factors $f_x(r)$ being defined,

$$f(r;R,a) = \frac{1}{1+e^{(r-R)/a}} \tag{2.43}$$

This form is shown in figure 2.19. The variable R defines the radius and a defines the surface diffusivity. The spin-orbit term takes the derivative of this form and hence acts at the nuclear surface.

Pion optical potentials are generally more complex, their form being motivated by theoretical considerations. The form used by Carr [Car82] is:

$$\begin{aligned} 2\omega U &= -4\pi[p_1 b(r) + p_2 B(r) - \vec{\nabla}\cdot\frac{L(r)}{1+\frac{4\pi}{3}\lambda L(r)}\vec{\nabla} \\ &\quad + \frac{1}{2}(1-p_1^{-1})\nabla^2 c(r) + \frac{1}{2}(1-p_2^{-1})\nabla^2 C(r)] \end{aligned} \tag{2.44}$$

From these potentials, nucleon and pion distorted waves are generated by solving the relevant wave equation viz. Schrödinger or Klein-Gordon. The distorted

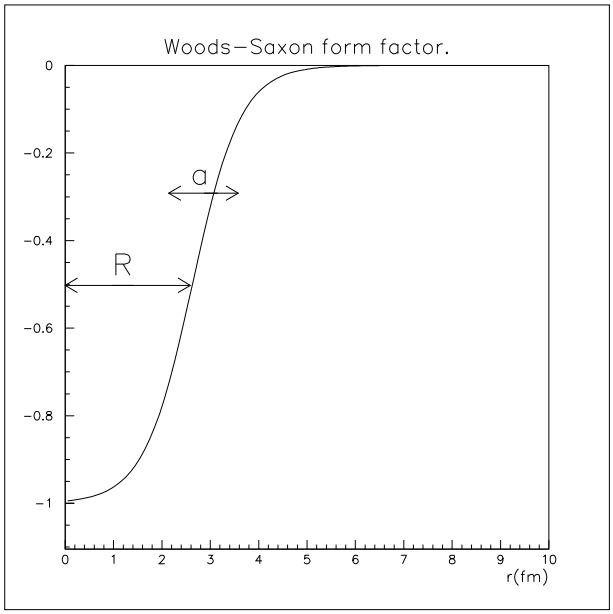

Figure 2.19: *The Woods-Saxon form factor*

waves are used in place of plane waves in nuclear calculations. One criticism of this approach is that no knowledge is retained about the nature of events removed from the elastic channel. At the expense of a semi-classical treatment, this deficiency is rectified in the Monte Carlo cascade treatment of FSI. Exiting particles are tracked along classical trajectories and at each step there exists a chance of scattering or absorption, the probabilities being extracted from optical potentials. Thus one can establish the nature of events which have undergone inelastic FSI. This method is particularly important for inclusive measurements where one cannot necessarily select clean events.

A more intuitive quantity relating to final state interactions is that of transparency. It defines the probability of a particle exiting a nucleus and is a function of particle energy. Typical values for the energy regions relevant to this experiment are 0.8 for nucleons and 0.5 for pions. The large absorption probability of pions means that even though the photon probes the whole nuclear volume, only those pions produced near the surface are likely to escape and be observed.

2.4.2 The Distorted Wave Impulse Approximation

The nuclear pion photoproduction process is expected to be essentially quasi-free i.e. the photon interacts with a single nucleon, the residual nucleus acting as a spectator in the reaction. This concept is shown schematically in figure 2.20.

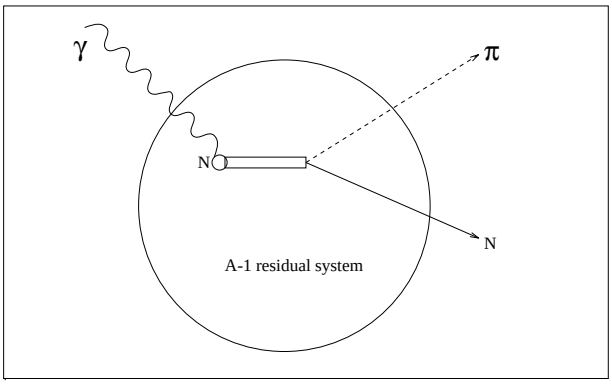

Figure 2.20: *The quasi-free nature of nuclear pion photoproduction*

The obvious first step in describing the A(γ, π^+n) B* reaction is to neglect the medium modifications to the production amplitude and work in the framework of the Impulse Approximation (IA). In the IA, the Fermi motion of the nucleons is accounted for but the free transition operator, $t_{(\gamma,\pi)}$, is used. This is expressed formally as:

$$T = \sum_{nucleons} t_{(\gamma,\pi)} \tag{2.45}$$

where $t_{(\gamma,\pi)}$ is that of the Blomqvist-Laget (B-L) model [Blo77] for example. In order to realistically describe the reaction, the interaction of the outgoing particles with the residual nucleus must be taken into account. These Final State Interactions are modelled by distorting the outgoing waves via the use of optical potentials for the residual system. With this ingredient added to the model, it becomes the Distorted Wave Impulse Approximation (DWIA).

The DWIA formalism was first applied to the A(γ, π^+n) B* by Laget [Lag72]. In his factorised DWIA approach, the derivatives (momentum operators) in the transition operator $t_{(\gamma,\pi)}$ were replaced by the particle asymptotic momenta thus rendering it a local operator. This modification allowed the cross section to be

factorised as follows [Pha91],

$$\frac{d^3\sigma}{dT_\pi d\Omega_\pi d\Omega_n} = k\sigma^{cm}_{\gamma p\to\pi n}|\Psi_l^D|^2 \tag{2.46}$$

where k is a kinematical factor, $\sigma^{cm}_{\gamma p\to\pi n}$ is the free cross section (expressed in the pion-nucleon centre of mass) and Ψ_l^D is the distorted momentum distribution,

$$\Psi_l^D = S\int \chi_\pi^{-(*)}\chi_n^{-(*)}e^{ik_\gamma\cdot r}\phi_l(r)dr \tag{2.47}$$

Here, the $\chi^{-(*)}$ represent the distorted outgoing waves of pion and neutron, ϕ_l is the wave function of the bound nucleon and S is its spectroscopic factor.

Li, Wright and Benhold [Li93] investigated the effects of the non-locality of the transition operator by retaining the momenta as operators and working in momentum space in order to perform the calculation. The pertinent point being that a distorted nucleon (or pion) wave function with a given asymptotic momentum will have a whole range of momentum components inside the nucleus and it is with these internal momenta that the transition operator should be evaluated. The distorted wave function for a nucleon of asymptotic momentum p is expressed as $\Psi(r,p)$ which, when Fourier transformed, becomes, in momentum space, $\Psi(p',p)$. Thus, to properly evaluate the cross section, one has to integrate over the momentum p' using the transition operator evaluated at this momentum. The expression for cross section in this formalism cannot be factorised and takes the form,

$$\frac{d^3\sigma}{dT_\pi d\Omega_\pi d\Omega_n} = k\bar{\sum}|M_{fi}|^2 \tag{2.48}$$

$$\bar{\sum}|M_{fi}|^2 = \frac{1}{2(2J_i+1)}\sum_{\alpha\lambda m_s}\frac{S_\alpha}{2j+1}|T(\alpha,\lambda,m_s)|^2 \tag{2.49}$$

$$T(\alpha,\lambda,m_s) = \int d^3p'd^3q' \Psi^+_{m_s}(\mathbf{p'},\mathbf{p})\phi^+_\pi(\mathbf{q'},\mathbf{q})t_{\gamma\pi}(\lambda,\mathbf{k},\mathbf{p_i},\mathbf{q'},\mathbf{p'})\Psi_\alpha(\mathbf{p_i}) \tag{2.50}$$

where $\alpha = \{nljm\}$ represents the state of the bound nucleon (of momentum $\mathbf{p_i}$), λ is the photon polarisation and m_s is the spin projection of the outgoing nucleon. The $\bar{\sum}$ represents the averaging over initial and summing over final state spin projections. S_α is the spectroscopic factor for state α. This treatment is applied at the expense of an extra three dimensions of integration w.r.t the factorised

case. The authors found the inclusion of non-local effects important in describing some exclusive (γ, π) reactions where nuclear structure plays a prominent role and also found an observable effect in the $(\gamma, \pi\mathrm{N})$ calculations. Some care was needed in treating the off-shell aspects of the amplitude as the B-L version of $t_{(\gamma,\pi)}$ was used which has no natural extension of the mass shell of the struck nucleon.

One final comment to be made on DWIA calculations covers the work of Glavanokov [Gla79]. In his DWIA treatment of the $\mathrm{A}(\gamma, \pi\mathrm{N})\,\mathrm{B}$ reaction, special care was taken to work with fully antisymmetrised nuclear wave functions. The natural implication of this is the inclusion of an exchange term in the amplitude as shown in figure 2.21(b). Physically, this corresponds to the photon interacting with the residual nucleus producing a pion with the outgoing nucleon actually being a spectator in the reaction. This treatment was motivated by the excess strength observed at backward nucleon angles in the $^{12}\mathrm{C}(\gamma, \pi^0\mathrm{p})$ Tomsk data w.r.t calculations involving the direct term (figure 2.21(a)) alone. The exchange term increased predictions at backward angles but not enough to meet the data points, as shown in figure 2.21(c), where the dotted line represents the calculations with the inclusion of the exchange term.

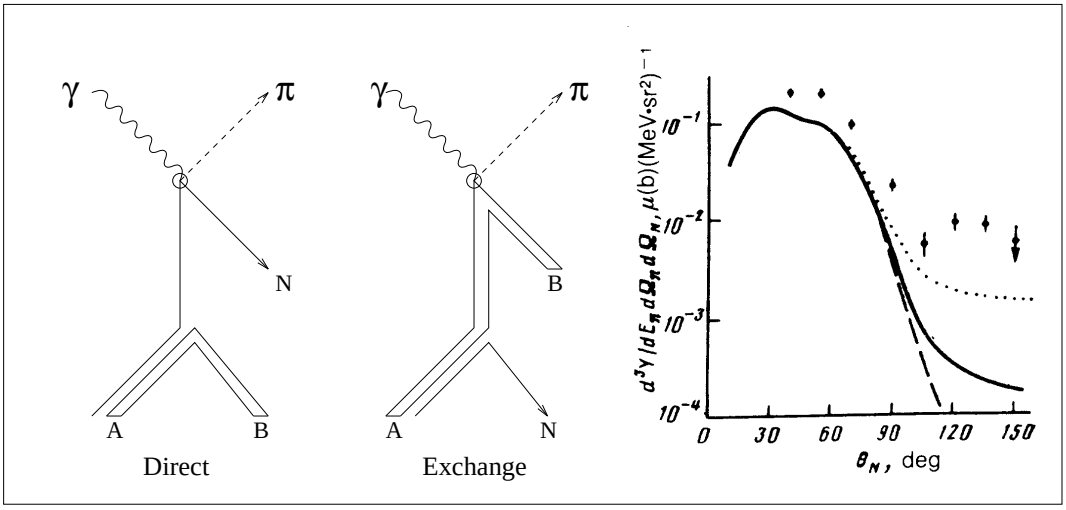

Figure 2.21: *The exchange term in the $A(\gamma, \pi\mathrm{N})\,B$ reaction amplitude*

2.4.3 The Δ-hole Model

In an attempt to describe pion-nucleus scattering, Kisslinger introduced the Isobar-Doorway model in 1973 [Kis73]. The model treats the excitation of the Δ as the dominant initial process in the reaction. The Delta and the associated hole both propagate in the nuclear medium and it is in the expression for this propagator that medium effects are introduced. These ideas were first applied to photoabsorption reactions by Moniz and Koch [Koc84] in what they termed the Δ-hole approach. Encouraged by the success in describing pion scattering, they included the case where the Δ is excited by a photon rather than a pion. The rest of the formalism was little changed and basically carried over from pion scattering. This supplied an important consistency constraint as the same Δ propagator should in principle be applicable to the photonuclear case as that used in pion physics. Recently, the model has been applied specifically to the A(γ, πN) B reaction by Sato and Takaki [Sat93]. Within this formalism, the resonant (Delta) part of the transition operator for free pion photoproduction is expressed:

$$t_\Delta = F^\dagger_{\pi N\Delta} \frac{1}{D(E)} \tilde{F}_{\gamma N\Delta} \tag{2.51}$$

where the F terms are vertex functions related to the absorption of the photon and emission of the pion. The resonance denominator takes the Breit-Wigner form:

$$D(E) = E - E_R + \frac{1}{2} i\Gamma(E) \tag{2.52}$$

In the nuclear medium, the modifications to the propagation of the Delta are taken into account by replacing this term with the expression,

$$\hat{G}^{-1}_{\Delta h} = D(E - H_\Delta) - W_\pi - \delta W - V_{sp} \tag{2.53}$$

as seen schematically in figure 2.22. The free resonance denominator is evaluated at (E-H_Δ), the internal energy of the π-N system. The Δ-Hamiltonian H_Δ is,

$$H_\Delta = T_\Delta + H_{A-1} + V_\Delta \tag{2.54}$$

where T_Δ is the kinetic energy of the Δ, V_Δ its binding potential and H_{A-1} takes into account the hole energy. The remaining terms relate to the various medium

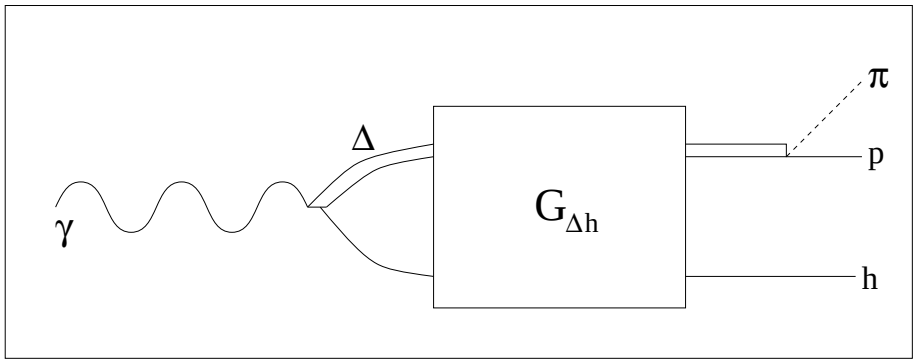

Figure 2.22: *Many-body Greens function in the* Δ*-hole model*

effects. W_π is a rescattering term taking into account coherent π^0 production. The term δW takes into account possible Pauli blocking of the Delta decay inside the nucleus. The most important term is the complex spreading potential V_{sp} which accounts for the coupling of the Delta to more complex configurations e.g. $\Delta N \rightarrow NN$ decay modes. It is a phenomenological potential in that it is chosen to fit pion scattering data.

So far, only the Delta contribution to pion photoproduction has been included in the model. The Delta contributes to the $M_{1+(3/2)}$ multipole of the amplitude and in the model of Sato and Takaki a non-resonant (background) contribution is added to this. Further contributions are added from the pion-pole and background components of the amplitude. Thus,

$$t_{M_{1+(3/2)}} = t_\Delta + t_{b(3/2)} \tag{2.55}$$

$$t = t_{M_{1+(3/2)}} + t_{pion-pole} + t_{b.g} \tag{2.56}$$

This leads to the following expression of the full amplitude:

$$T = < \psi_p^{(-)} \phi_\pi^{(-)}; h|t|\mathbf{k}; 0 > \tag{2.57}$$

where ψ and ϕ are distorted proton and pion waves, $|0>$ and $|h>$ are the nuclear ground and one-hole states and $|\mathbf{k}>$ represents the initial photon state.

2.4.4 Full Microscopic Approach

Both of the previous models have visible weaknesses. The DWIA approach does not take into account medium modifications to the Delta, whereas the Δ-hole model does this in a phenomenological fashion (through the spreading potential) but is only relevant to the resonant part of the production amplitude. Although some theorists have attempted hybrid DWIA/Δ-h calculations, perhaps the most rigorous approach to the problem is that developed by Carrasco, Oset and collaborators [Car92a, Car92b, Car94].

They have used the basic interactions between photons, pions, nucleons and isobars expressed in terms of coupling constants, form factors and propagators and proceeded to apply field theoretical methods to calculate the photon self energy diagrams in nuclear matter. A photon of energy k gets renormalised in the medium with a complex self-energy $\Pi(k, \rho)$ which depends on the nuclear matter density ρ. The imaginary part of the self-energy represents the rate of loss of photon flux in the medium:

$$-\frac{1}{N}\frac{dN}{dt} = -\frac{1}{k} Im\Pi(k, \rho) \tag{2.58}$$

Because of the weak nature of the electromagnetic interaction (i.e. there are negligible screening effects) one can make use of a volume integral to apply the above to a finite nucleus, thus gaining an expression for the photoabsorption cross section,

$$\sigma_A = \int d^3r \frac{1}{k} Im\Pi(k, \rho(r)) \tag{2.59}$$

where the local density approximation (LDA), $\rho \rightarrow \rho(r)$, provides the connection between infinite nuclear matter and the finite nuclear system. The obvious drawback here is the lack of nuclear structure i.e. there is no shell structure implicit in the model as its results are derived from nuclear matter (Fermi gas) calculations. This may well prove a weakness for fully exclusive measurements which should be sensitive to the shell from which a nucleon is removed. However, where the shells are integrated over, as in inclusive reactions, then the problem is not so serious. Thus far, only an expression for the total absorption cross section in terms of the photon self energy has been given. The beauty of the model lies in the derivation

of the photon self energy. The self energy is found by calculating various Feynman graphs and, by applying particle-hole expansions etc. to the graphs, various many body medium effects can be included in the model. Figure 2.23 shows some examples of the graphs which go to make up the self-energy.

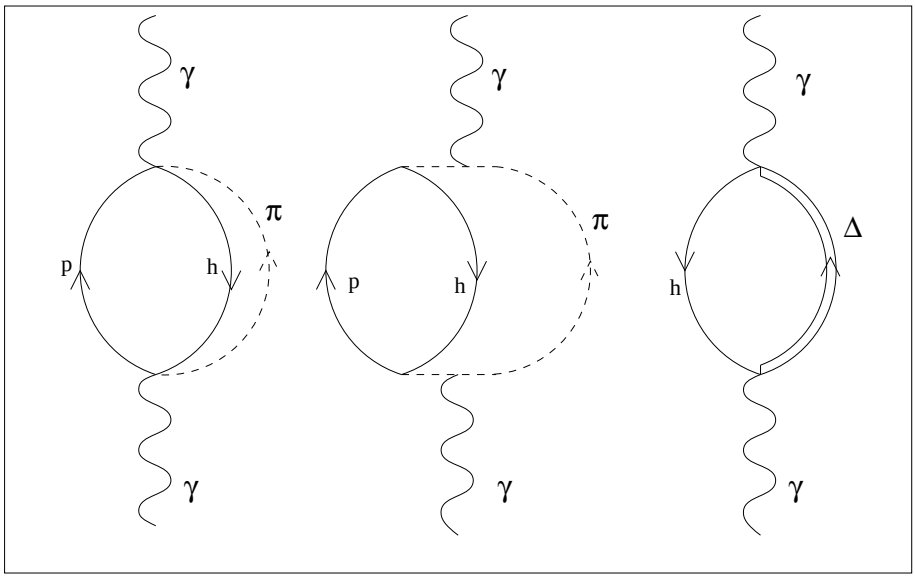

Figure 2.23: *Typical photon self-energy Feynman diagrams*

Particle hole propagators are expressed using Lindhard functions which demand that particle energies are above the Fermi level and hole energies below it. The Fermi level ϵ_F is defined in terms of the nuclear density:

$$\epsilon_F = -\frac{1}{2M}(\frac{3}{2}\pi^2\rho)^{2/3} \tag{2.60}$$

and by this technique the Pauli exclusion principle is enforced. Not only does the theory allow for the inclusion of such medium effects but the procedure for extracting the imaginary part of the self energy allows the contribution to the cross section from individual reaction channels to be ascertained. The imaginary component of a graph is found by applying Cutkosky Rules to it. These involve making cuts through the graph and replacing propagators of particles intercepted by the cut with their imaginary parts. In the procedure, any cut particles are placed on shell and are thus present in the final state. Thus each graph can be associated with a definite reaction channel. Figure 2.24 shows the application of

Cutkosky rules to a typical self energy graph. The upper cut puts two nucleons on shell and corresponds to direct photon absorption whereas the lower cut puts a pion and a nucleon on-shell and corresponds to the pion production channel.

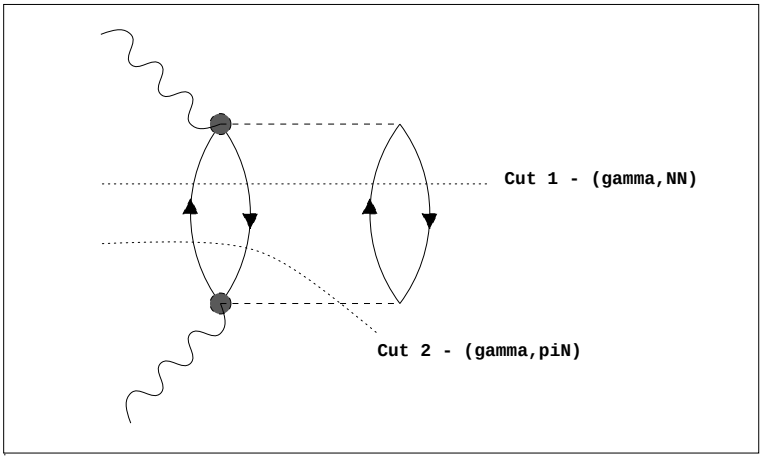

Figure 2.24: *The application of Cutkosky Rules*

It is, however, possible that the particles placed on-shell undergo final state interactions (FSI) and the produced pion in figure 2.24 for example may later be absorbed leading to what Oset calls indirect absorption, where the initial step was pion photoproduction but subsequent absorption leads it to pure nucleon emission. The benefits of being able to split the reaction cross section into the various channels is important for our understanding of the mechanism and this separation is preserved in the treatment of FSI which is done by a cascade calculation. Particles are tracked out of the nucleus, at each step the dice being thrown to determine whether scattering from or absorption by the residual nucleus takes place. This approach is semi-classical but has been found to be quite accurate in the energy range of interest. The cascade acts as an event generator to which detector thresholds and angular coverages can be applied allowing for easy comparison of theory and experiment. It must be stressed that the medium effects are applied comprehensively to all parts of the amplitude. Not only is Delta propagation considered but also pion propagation and vertex corrections.

Chapter 3

Experimental Apparatus

3.1 Introduction

The nuclear pion photoproduction experiment described in this thesis was performed using the facilities of the Institut für Kernphysik at Mainz. The Mainz Microtron (MAMI), in combination with the Glasgow Tagger, has facilitated a new generation of high quality photonuclear experiments. This opportunity forms the basis of the A2 (real photons) collaboration at Mainz.

Within the A2 collaboration, there exists several sub-groups associated with specific areas of research. Researchers from the universities of Edinburgh, Glasgow and Tübingen form the PiP-TOF collaboration. The collaboration aims to discover details of the photoabsorption mechanism by studying (γ,pN) and (γ, πN) reactions on light nuclei. The two main detector systems which give their names to the group are PiP, a scintillator hodoscope designed to detect protons and positive pions, and TOF, a large scintillator time-of-flight array for charged and neutral particle detection. There are also associated ΔE detectors which are used for triggering and particle identification. Equally crucial to the experiment are the electronic and computing systems required for triggering, data acquisition and online analysis. Each of the above elements will be described in more detail in this chapter.

3.2 The Mainz Microtron

The cornerstone of the experiment is the high quality 100% duty factor electron beam provided by the Mainz Microtron [Her90]. The three Race Track Microtron (RTM) stages which form MAMI-B provide a low emittance, highly stable 855 MeV electron beam available at currents from a few picoamps up to one hundred microamps.

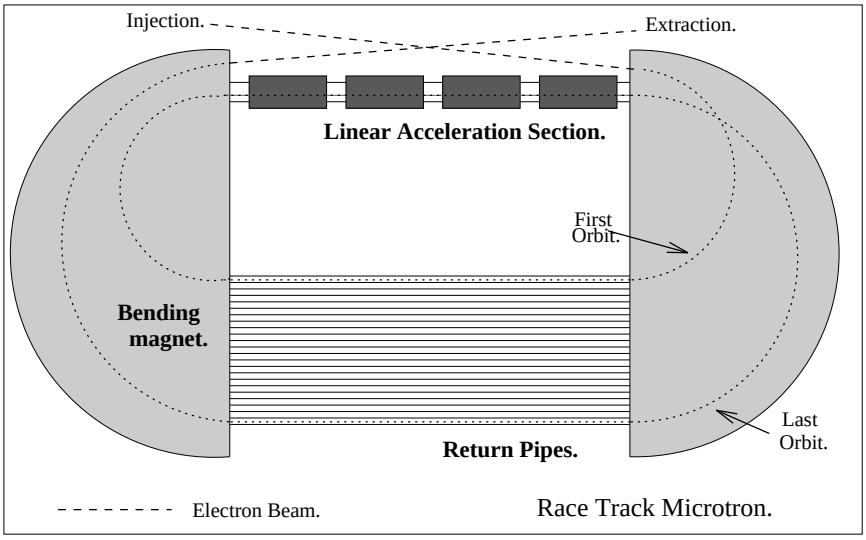

Figure 3.1: *A schematic view of a Race Track Microtron*

3.2.1 Race Track Microtrons

A microtron consists of a linear accelerating section (linac), two bending magnets and a collection of return pipes which together give it its 'race track' shape, as shown in figure 3.1. The linac consists of waveguides carrying radio frequency electric fields which accelerate the electrons. Bending magnets recirculate the beam many times, the orbit length being increased at each pass such that the beam always returns to the linac section in phase with the accelerating field [Cro94].

Due to the many recirculations, the energy boost required at each pass through the linac is relatively low and the accelerating structure can be operated in continuous wave (c.w.) mode. For example the third RTM produces an energy gain per turn of 7.5 MeV. This is achieved using 5 klystrons dissipating a total of 168 kW

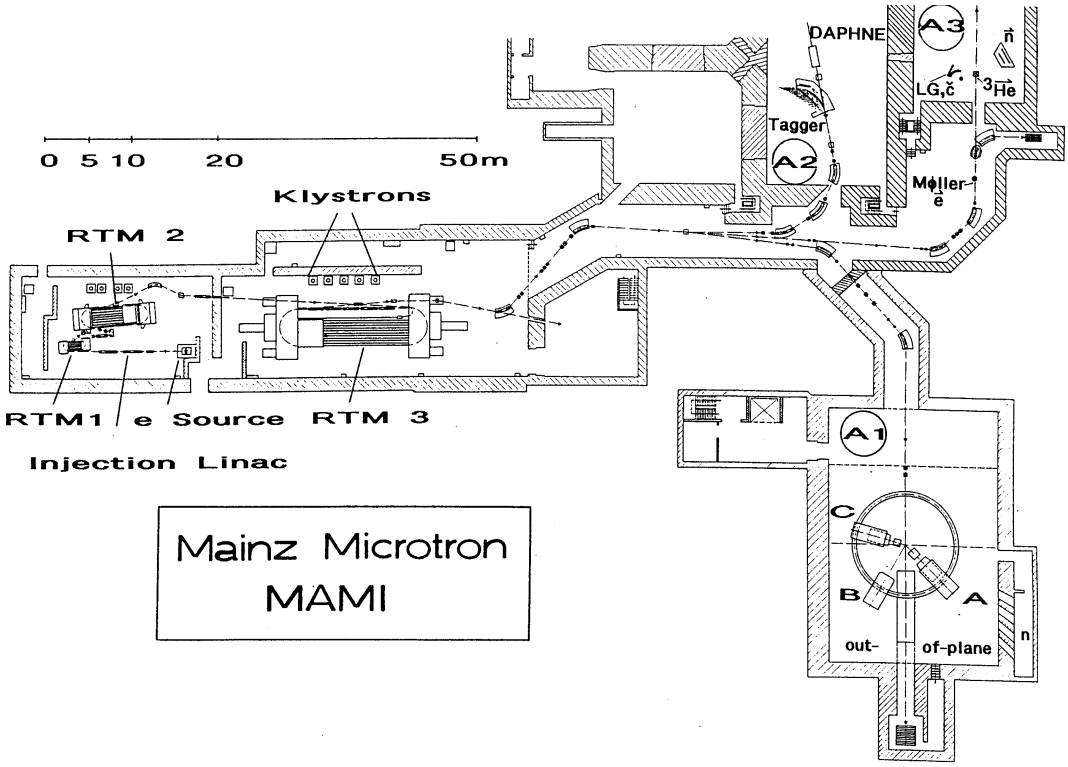

Figure 3.2: *The Mainz Microtron, MAMI, at the Institut für Kernphysik, Mainz.*

in continuous mode. Because electrons are accelerated in phase with the electric field, the beam acquires a pulsed nature. However, the frequency of 2.45 GHz is so high that for practical purposes one can regard the beam current as continuous. This continuous operation gives the beam its 100% duty factor which is so valuable in coincidence experiments. For a given average current the rate of random coincidences will be far less for a continuous beam as compared to a pulsed one. This in practice allows higher currents to be used and thus shorten the time needed to gain adequate statistics.

3.2.2 MAMI-B

A plan of the MAMI-B facility is shown in figure 3.2. A 100 keV gun followed by three linac sections injects 3.5 MeV electrons into the 18 turn RTM1, which increases their energy to 14 MeV. They are then transported to the 51 turn RTM2, which produces a 180 MeV beam. This system formed the MAMI-A accelerator which was used for experiments until 1987.

The upgrade to MAMI-B, completed in 1990, involved the addition of the 450 tonne RTM3. This stage produces the 855 MeV electron beam with a resolution of 60 keV and emittance less than 0.14 π.mm.mrad in both horizontal and vertical directions. Once extracted from RTM3, the beam can be transported to one of the three experimental halls, A1 to A3, shown in the plan. Photonuclear reaction studies proceed in the A2 hall where a radiator and tagging system are installed.

3.3 The Tagged Photon Technique

The electron beam produced by MAMI-B is focused on to a 4 μm Ni foil in the A2 hall. Bremsstrahlung radiation is produced in a forward directed cone of average semi-angle $\frac{m_e}{E_e}$ [Bet34] and with an energy distribution approximately proportional to $1/\mathrm{E}_\gamma$. A magnetic spectrometer is then used to analyse the electrons residual to the Bremsstrahlung process $(e, e'\gamma)$. Given the incident electron energy E_e (855 MeV at MAMI-B) and a measurement of the residual electron energy $\mathrm{E}_{e'}$, the associated (coincident) photon's energy can be simply reconstructed,

$$E_\gamma = E_e - E_{e'} \tag{3.1}$$

This photon beam is collimated to form a small beam spot on the target several metres downstream. Photons induce reactions in the target and thus generate experimental triggers. To bring tagging into effect, it is necessary to identify the particular residual electron coincident with any particular photon such that a proper photon energy determination can be made. This requires a timing measurement to establish a coincidence peak and thus separate prompt electrons from randoms which are not correlated with the photon. In order to obtain reaction cross sections it is necessary to know the photon flux at the target. This is achieved by counting the number of residual electrons and relating this to the number of photons by a quantity called tagging efficiency, which takes into account the effects of photon beam collimation.

The following sections look at how this technique was implemented in the current experiment.

3.3.1 The Glasgow Tagging Spectrometer

The Glasgow Tagger is shown in figure 3.3. The tagger analyses residual electrons produced when the 855 MeV electron beam undergoes Bremsstrahlung at the radiator. It also transports the main beam (the vast majority of electrons that do not interact with the radiator) to the beam dump.

The design included the following requirements [Ant91]:

- A large momentum acceptance (p_{max}:$\mathrm{p}_{min} \approx$ 16:1).

- A single field setting to cover the entire momentum range $0.06\,E_0$ - $0.95\,E_0$.
- Good intrinsic resolution - of the order of 120 keV.
- Vertical focusing to reduce the pole gap required.

To achieve this a Quadrupole-Dipole (QD) design was chosen. The quadrupole magnet provides a degree of vertical focusing and the dipole bends and focuses the electrons onto a reasonably flat focal plane.

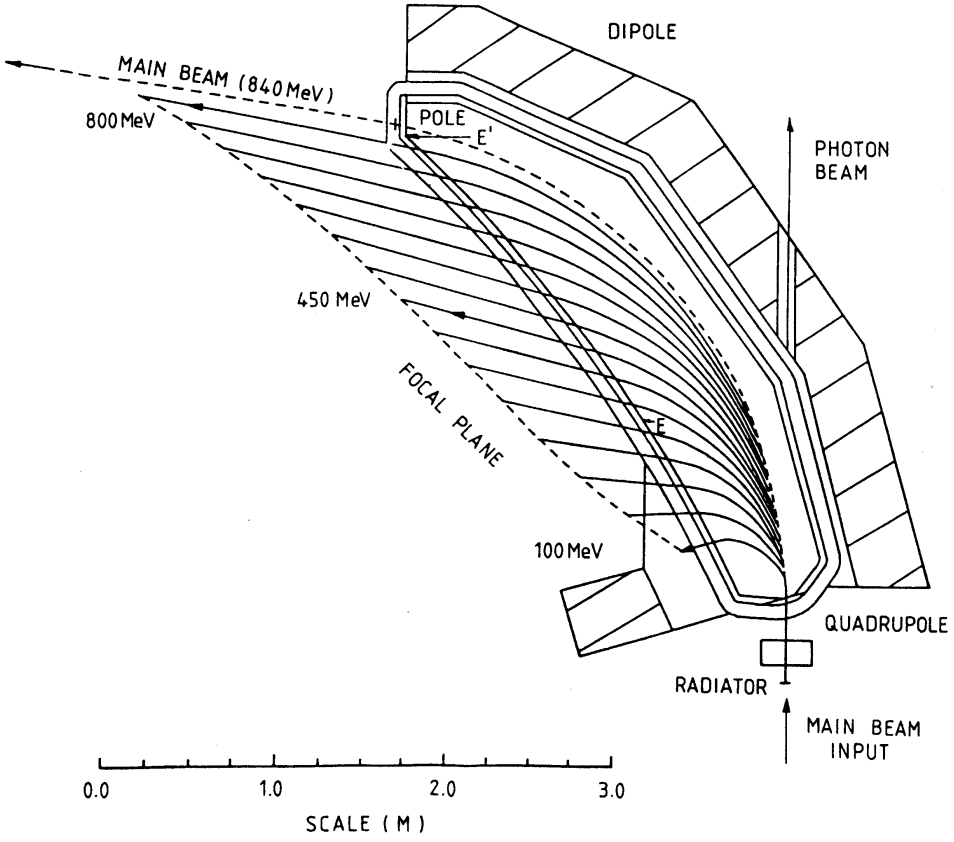

Figure 3.3: *The Glasgow Tagging Spectrometer*

3.3.2 The Focal Plane Detector

A residual electron's energy is determined by establishing the point at which it traversed the spectrometer's focal plane. This is achieved with an array of 353 scintillators spread along the plane. This Focal Plane Detector (FPD) can tag photons in the range 40-790 MeV with a resolution averaging 2.2 MeV. Each detector element is connected to a small photomultiplier (PM) tube, the output of which is fed into a dual threshold discriminator, which gives <1 ns timing resolution. The elements overlap and in order to reduce the contribution from background electrons a coincidence is demanded between neighbours. Figure 3.4 shows a diagram of the detector. The associated logic pulses are routed to the tagger electronics racks where the FASTBUS scalers and time to digital converters (TDCs) record the required information. The scalers are used to obtain a measurement of the photon flux, while the TDC's are gated by the main detector systems such that a coincidence between the photon induced reaction at the target and a residual electron at the focal plane can be identified.

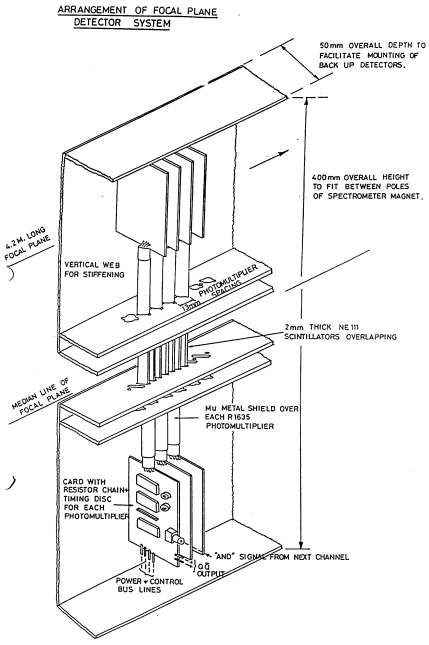

Figure 3.4: *Instrumentation of the Focal Plane Detector*

3.3.3 The Photon Beam: Collimation and Tagging Efficiency.

In order to maintain a reasonable size of photon beam spot on the target, i.e. a well defined reaction vertex, the photon beam is collimated. The majority of photons do not interact with the target and are dumped at the far end of the A2 hall. The photon beam line is shown in figure 3.5, which also shows the P2 ionisation chamber that is used to obtain a rough measurement of the photon flux.

The P2 chamber is only used as a diagnostic and in the analysis it is the tagger scalers which are used to obtain the photon flux. The scalers count the number of electrons detected in each FPD element. Some of the corresponding photons are removed from the beam by collimation and the fraction which reach the target is given by the tagging efficiency.

$$N_\gamma|_{(\text{coinc. with e}' \text{ at FPD})} = N_{e'}.\epsilon_{tagg} \tag{3.2}$$

To measure the tagging efficiency the beam current is lowered (to suppress random coincidences in the tagger) and a Pb glass detector is placed in the photon beam. The block represents 30 radiation lengths and thus has very close to 100% photon detection efficiency. Photons incident on the block generate triggers which gate the tagger TDCs. The TDCs record the time of any coincident residual electrons on the FPD. Meanwhile, the tagger scalers count the total number of residual electrons in each element. Thus the tagging efficiency for each element is obtained:

$$\epsilon_{tagg} = \frac{\text{TDC counts}}{\text{scaler counts}} \tag{3.3}$$

Tagging efficiency measurements were made several times throughout the week long experiment. The average efficiency remained stable at around 55%.

Figure 3.5: *The photon beam line*

3.4 Targets

The two main targets used in the October 1993 experiment were Carbon-12, to perform the $^{12}C(\gamma, \pi^+ n)$ measurement, and CH_2 to obtain $p(\gamma, \pi^+)$ n calibration data. The targets were mounted on a ladder coupled to a stepper motor which could be controlled from outside the experimental hall.

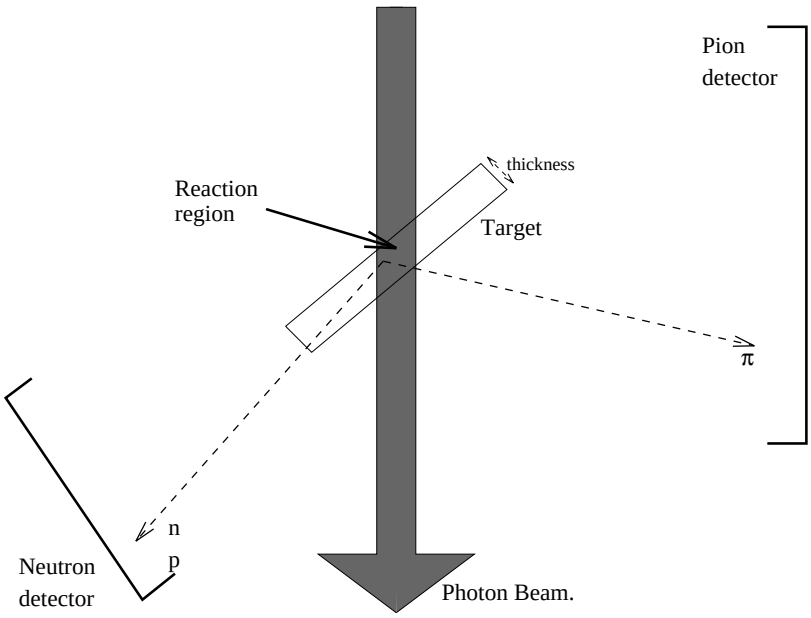

Figure 3.6: *The target installation*

The choice of target thickness is very important to the experiment. Obviously, a thicker target presents more nuclei/cm^2 to the beam thus increasing the reaction count rate. However, the increased thickness increases the uncertainty in the reaction vertex thus reducing the angular resolution of the measurement. One must also consider that the reaction products must traverse the target material before reaching the detector systems. A thicker target gives greater uncertainties in the ionisation energy loss due to this traversal and hence reduces the resolution with which the particle's energy can be determined. These effects can be seen clearly in figure 3.6.

The situation can be improved by a clever choice of target angle. The pions were mainly detected normal to the beam direction and by placing the target at a small angle to the beam one increases its effective thickness to the photon

beam while reducing the average target energy loss of the pions. For the neutrons, which are emitted at forward angles, the effect is to increase the amount of material traversed. However, due to their negligible ionisation energy loss, this does not effect the measurement.

The experiment was run with a 5 mm Carbon (graphite) target set at 20 degrees to the beam. This contributed 1.5° to the pion angular resolution and 3 MeV to its energy resolution. These contributions are less than those due to other factors, hence there is little to be gained from using a target thinner than this.

3.5 Particle Detectors

The photon can induce a wide variety of nuclear reactions in the target and this combined with the large electron background from atomic processes poses a challenge to the experimentalist. The particle detector systems used to study the $^{12}C(\gamma, \pi^+n)$ reaction products are designed to meet this challenge. The requirements include:

- **Particle identification:** the systems should be able to discriminate between electrons, pions, protons and neutrons. This is achieved using veto detectors and ΔE-E measurements.

- **Satisfactory energy resolution:** energy measurements are made either by energy deposition or time-of-flight methods. The resolution required is dictated by the need to separate p- and s-shell excitation regions in the residual nucleus. A combined (missing energy) resolution of 10 MeV is required.

- **Satisfactory angular resolution:** in order to perform sensitive comparisons with theoretical predictions, good angular resolution is required. This generally depends on detector timing properties and the quality of scintillation light collection.

Figure 3.7 shows the layout of the particle detectors in the A2 hall. The three components, the ΔE-ring, PiP and TOF are discussed in more detail below.

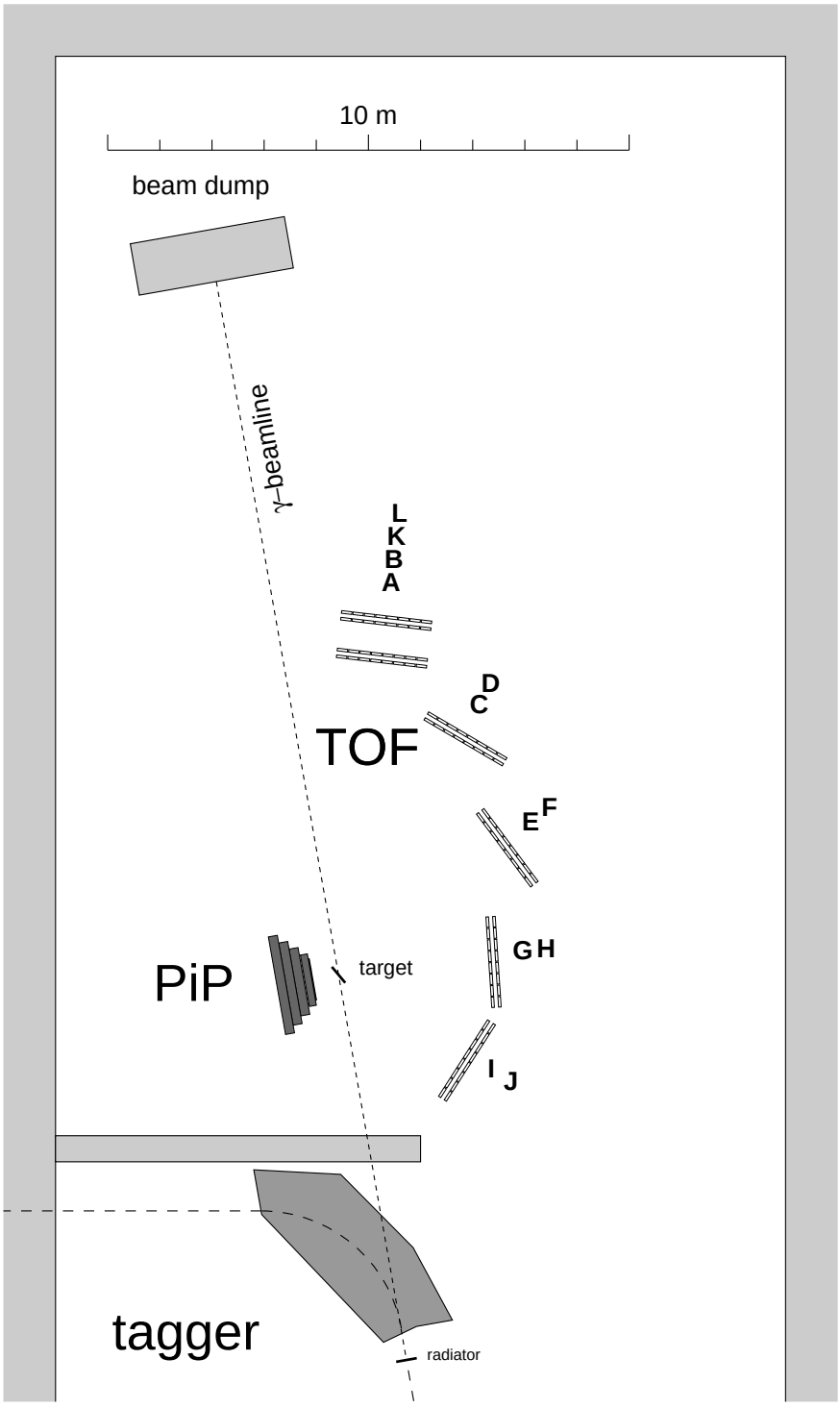

Figure 3.7: *Detector arrangement in the experimental hall*

3.5.1 The ΔE-ring

The ΔE-ring is shown schematically in figure 3.8. The ring is centred on the target and has a radius of 11 cm. Each side of the ring is composed of seven separate scintillator segments.

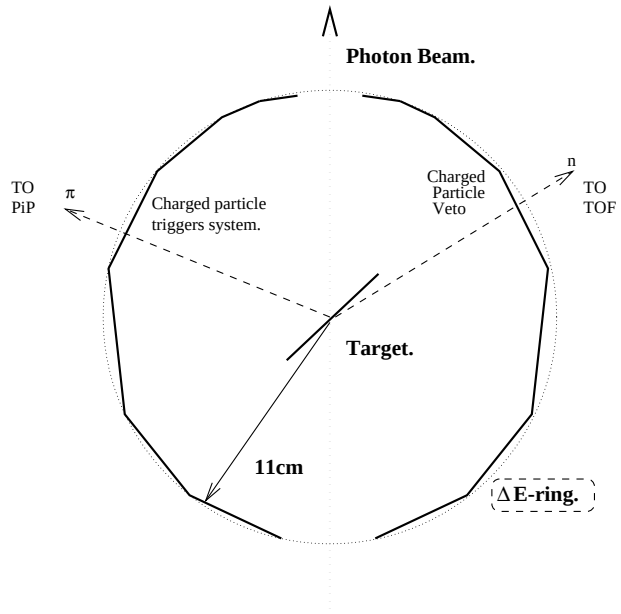

Figure 3.8: *The ΔE-ring detector*

The ring performs two main functions in the overall detection system:

- In coincidence with PiP, signals from the PiP-side of the ring form the 1st level trigger for the experiment. This guarantees a charged particle has come from the target. The time of the ΔE signal is closely correlated to the reaction time due to the detector's close proximity to the target. This signal therefore generates the 'start time' (TDC start) and all other times are measured relative to this.

- The TOF-side segments can act as a charged particle veto allowing identification of neutrals in TOF. This procedure is normally done in the offline analysis to avoid accidental vetoing by randoms.

Both ΔE signals can be used for particle identification using the ΔE-E method.

3.5.2 The PiP Detector

PiP is a Pion/Proton scintillator hodoscope. In the current experiment it was used specifically for the detection of positively charged pions. The problems specific to this method of pion detection are discussed in chapter five.

Figure 3.9 shows a graphic of the detector. It consists of a ΔE transmission layer followed by four E layers, E1 to E4. The specific scintillator used was NE110 which has very good attenuation length, viz. over 4m, making it suitable for large detector systems [Ne].

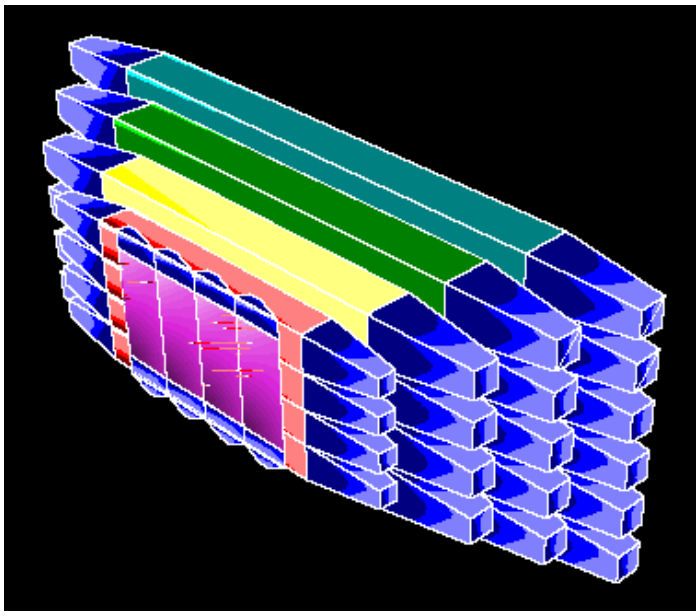

Figure 3.9: *The PiP Pion/Proton scintillator hodoscope*

The ΔE detector on the front face of PiP consists of four vertical scintillators 2 mm thick × 20 cm wide × 42 cm high. This element defines the solid angle of PiP to be ≈ 1.0 steradian at its usual position 50 cm from the target. The four E layers consist of four, four, five and six blocks respectively. The ends of the blocks are coupled to light guides which enable a more uniform collection of scintillation light. The light is guided into photomultiplier tubes. The E blocks use 130 mm diameter EMI 9823KB tubes while the ΔE blocks use the smaller 50 mm EMI 9954KB variety.

Each successive layer is larger than the previous one, to ensure that a particle

originating from the target will not pass out through the edges of the detector, even after allowance for multiple scattering [Bra91]. Their dimensions are given in table 3.1.

E layer.	No. Blocks	Block L × D × H (cm)
E1	4	100.0 × 11.0 × 13.5
E2	4	130.0 × 17.5 × 17.5
E3	5	160.0 × 17.5 × 17.5
E4	6	190.0 × 17.5 × 17.5

Table 3.1: The dimensions of the scintillator blocks in PiP.

The whole detector is constructed in modules and is supported by a strong steel framework. It is surrounded by a 5 mm steel plate box which provides a barrier against room background and a second defence against light leaks. The electronics are mounted in four racks behind the detector. The total weight of the detector assembly is $\approx$ 4 tonnes.

3.5.3 The TOF Detector

The second arm of the measurement is covered by the TOF array of 96 scintillator bars. Design goals included the optimisation of solid angle, time resolution and detection efficiency, while keeping the apparatus modular for application in different experiments [Bra91]. The height of the A2 hall and the required timing resolution dictated the $300 \times 20 \times 5\,\mathrm{cm}^3$ dimensions of the bars. Both ends are read out by 3" Phillips XP 2312B photomultiplier tubes. Time of flight is determined by the average time of both signals and position by the time difference. The bars are mounted onto frames which can contain multiples of 8 bars up to a maximum of 32 when configured 4 deep. A typical frame is shown schematically in figure 3.10.

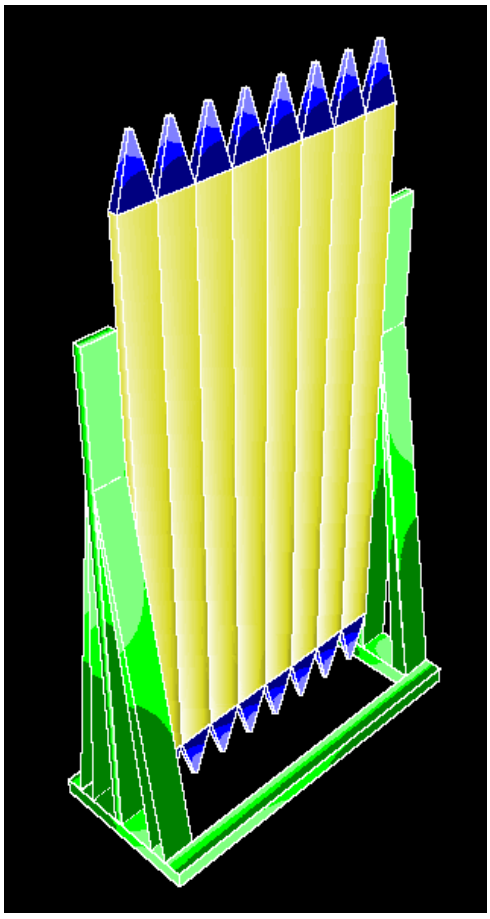

Figure 3.10: *A typical TOF detector stand*

3.6 Electronics: Event Triggering

When particles ionise the detector scintillator blocks, signals are generated at the photomultiplier (PM) tubes. The associated electronics needs to:

- Identify events of interest.
- Digitise the pulse height and time of the PM signals.
- Store all event information.

The first requirement is met by the trigger electronics which, on recognising a desired event, gates the Analogue to Digital Converters (ADCs) that are used to digitise pulse height and time information. Storage of this information is then performed by the data acquisition system which reads out these modules. The experiment is disabled while this process takes place, giving rise to experimental dead time. It is important to keep this dead time to a minimum and in practice this corresponds to making the trigger as selective as possible.

3.6.1 Event Information

For a given event (i.e. a specific reaction in the target) the experimentalist needs to know:

- the pulse height of the signals in each of the PM tubes. These are recorded in Charge to Digital Converters (QDCs) which must be gated by the trigger electronics. Due to the many channels in the experiment, Phillips Fastbus 10c2 10-bit QDCs were used. They are high density modules (32 channels) with a read out threshold and fast clear capability.
- the time of each PM signal relative to the reaction (start) time. To record this, pulses are processed by leading edge discriminators which produce a logic pulse when the input rises over a preset threshold. These logic pulses stop the Time to Digital Converters (TDCs). Philips Fastbus 10c6 10-bit TDCs were used which are similar in their specifications to the 10c2 QDCs described above.

Figure 3.11 shows the basic instrumentation supplied for each PiP, TOF and ΔE-ring block. The output from the ADCs forms the basis of the raw data, which is later analysed to reconstruct the kinematics of an event, viz. particle energies, angles and relative times. The electronic logic, which performs the function of deciding when to gate and read out these modules, is discussed next.

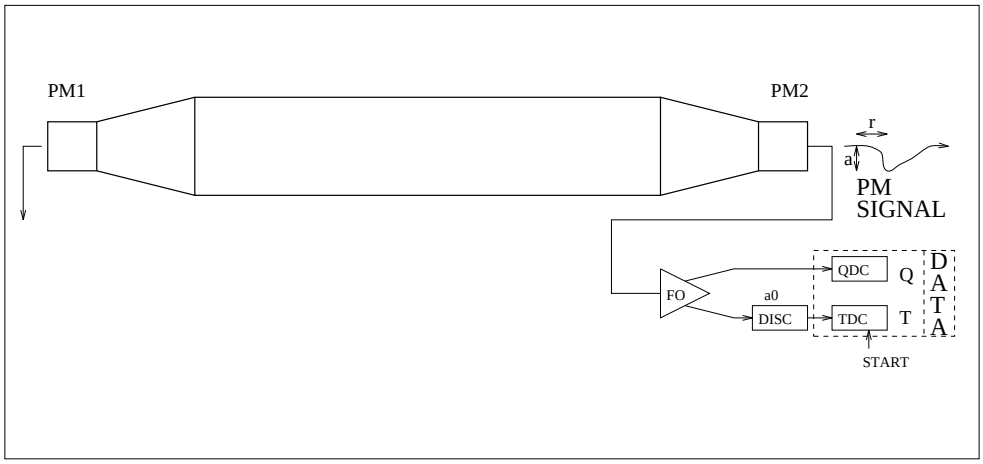

Figure 3.11: *Instrumentation of a typical scintillator block*

3.6.2 Trigger Logic

The trigger electronics use the logic pulses supplied by the discriminators to decide whether an event of interest has occurred. In the October 1993 ^{12}C(γ, π^+n) experiment, the events of interest were:

- Positive pions entering PiP which have an associated particle in the TOF array.
- Cosmic rays entering PiP which are used for calibration purposes.
- PiP and TOF flasher events which are used to monitor the gain stability of the PM tubes.

It is important to understand that the trigger logic requires time to identify these events. Meanwhile, the signals going to ADCs must be delayed in order to arrive coincident with the gate generated by the logic. The limited amount of

delay available to these signals has led to a two level trigger system. The first level makes a quick and simple decision. It provides the ADC gate, which starts the conversion of the modules. If a more complex decision is required, the first level trigger does not initiate the read out cycle but instead primes the second level trigger. After a preset time, the second level trigger decides whether to keep the event and thus initiate data acquisition (a relatively time consuming process) or alternatively, to reset the ADCs (via the Fast Clear facility) thus rejecting the event. Figure 3.12 shows a flow chart representing the decision making process implemented by the trigger logic.

Each detector (PiP, TOF, Tagger) has its own electronics racks, where its ADCs are housed in Fastbus crates. The ΔE-ring is considered part of PiP for this purpose. The trigger logic is based in the PiP racks but is fed auxiliary logic signals from the TOF and Tagger electronics. The trigger logic is implemented mainly by Camac and NIM modules. The data acquisition computer is also based in the PiP racks and data is read from the other systems via extension cables.

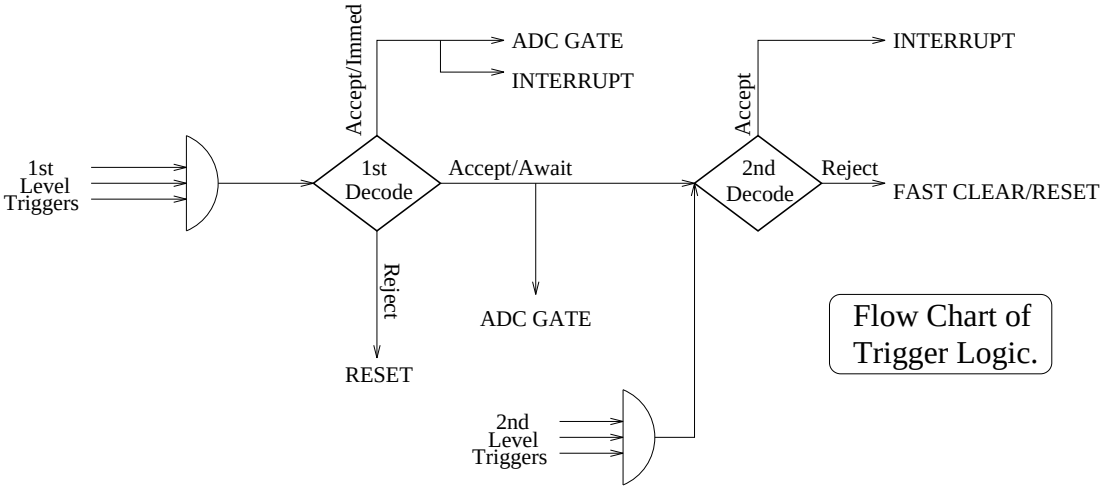

Figure 3.12: *Flow chart describing the trigger logic*

First Level Triggers

There are four varieties of first level trigger:

- **The PiP Particle Trigger:** This is the primary experimental trigger which identifies a charged particle emitted from the target and entering PiP. The time of this trigger corresponds closely to the reaction time and QDC gates and TDC starts are derived from it. Logically, it corresponds to a coincidence between the PiP-side of the ΔE-ring, the PiP ΔE and the first PiP E layer, E1.

- **The Cosmic Trigger:** For calibration purposes, PiP cosmic ray events are recorded. Only rays which traverse a single PiP layer are useful and the trigger demands that the top and bottom block of a given layer fire. This condition is implemented by a Lecroy 4508 Programmable Logic Unit (PLU), which maps an 8-bit input to an 8-bit output via a memory lookup table.

- **PiP and TOF Flasher Triggers:** In order to monitor the stability of the PM tubes in the PiP and TOF detectors, Light Emitting Diode (LED) flashers have been installed to inject a known amount of light onto the PM photocathodes. The LED output is monitored by a PIN diode. Each time the flasher is activated a trigger is generated to record the PM response.

- **Pb Glass Trigger:** During tagging efficiency runs, the Pb glass detector is placed in the beam. When a photon is detected, a trigger is generated.

The first level triggers form the inputs to a LRS4508 PLU which decodes them. When any trigger is raised, the PLU is strobed and the following output conditions can be generated:

- **Accept/Immediate:** If a Cosmic, Flasher or Pb glass trigger is present, then the relevant detectors are provided with ADC gates. No further decision is required and the data acquisition computer is interrupted such that the ADCs are read out and the event is stored.

- **Accept/Await:** If the PiP particle trigger has been raised, the ADC gates are generated but the interrupt of the acquisition computer is held off. Instead the second level trigger circuit is activated.

- **Reject:** If more than one trigger was present (an unlikely occurrence) then the event is rejected and the circuit reset.

Once a 1st level trigger has been accepted, the inputs are immediately disabled (latched) such that no more gates can be generated until the current event is processed and a reset pulse issued. The 1st level decode sub-circuit is shown in figure 3.13.

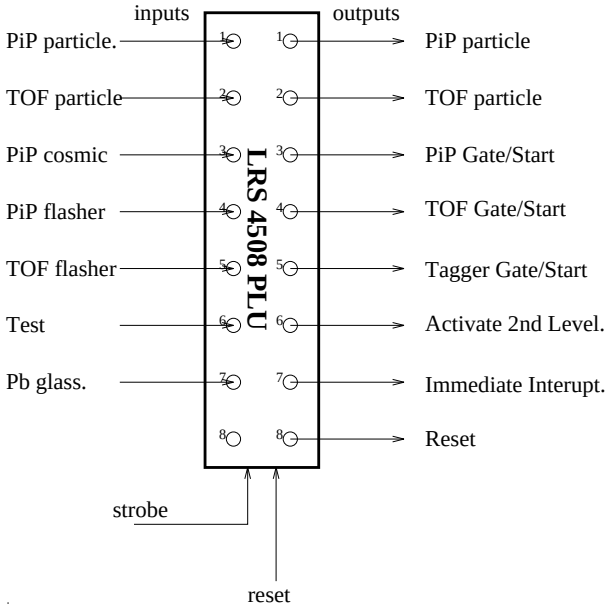

Figure 3.13: *The 1st level trigger decode circuit*

Second Level Triggers

The second level triggers are employed once a charged particle entering PiP has been identified. The 2nd level triggers correspond to more complex conditions which take more time to establish. There are four 2nd level triggers:

- **Electron Reject:** Due to atomic processes, there are a large number of low energy atomic electrons entering PiP. These generate PiP particle triggers

yet are of no value and if read out they would swamp the data. They are rejected by implementing a ΔE-E cut in hardware. Figure 3.14 shows how a ΔE vs. E plot can be used to distinguish particle types. By performing a weighted sum of the two signals and demanding the output is above a certain discriminator threshold the electrons in the bottom left corner of the plot can be rejected. The discriminator output forms the e-reject 2nd level trigger. The PiP ΔE and E1 signals are used. If the particle proceeds to the second layer (E2) then the procedure is no longer valid, due to fold back (the E1 signal no longer corresponds to total energy). The reject trigger must be overridden if an E2 signal is present hence the E2 signal is also provided as 2nd level trigger.

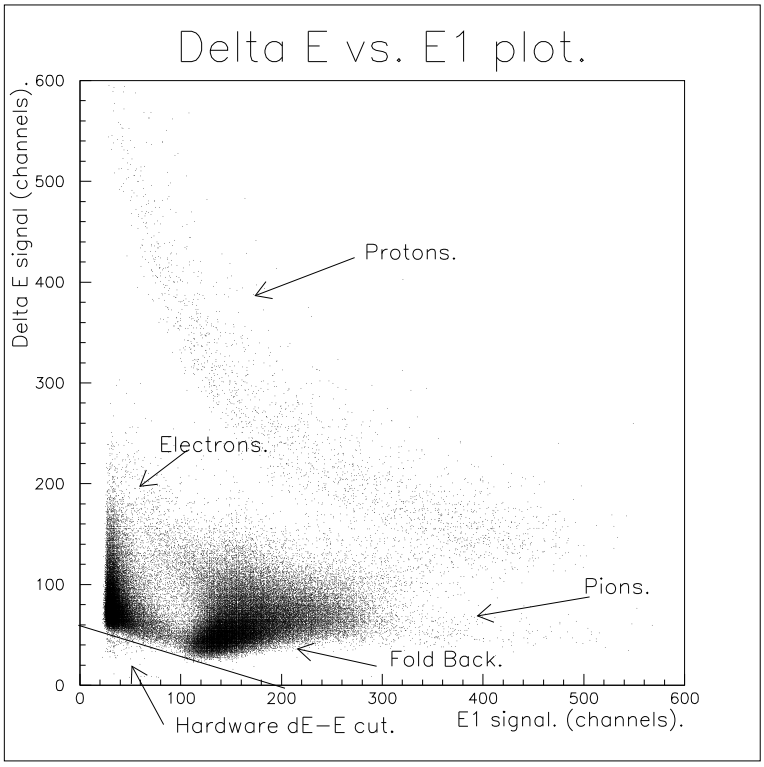

Figure 3.14: *Particle identification in a ΔE-E plot*

- **TOF-OR:** Approximately 90% of events with a particle in PiP have no corresponding particle detected in the TOF array and, if recorded, would simply be discarded in the offline analysis. The TOF-OR trigger is a gated OR of all 96 TOF blocks. It requires a particle to be detected in TOF within

400 ns of the initial PiP trigger. The increased selectivity introduced by this trigger dramatically lowers the experimental dead time.

- **Tagger-OR:** In order to reconstruct the photon energy, a prompt electron must be present in the Tagger Focal Plane Detector. The Tagger-OR is a gated OR of all 352 FPD elements. It requires an electron to be present within the 80 ns PiP-Tagger coincidence window. At normal beam currents, the trigger is effectively redundant as there are usually several randoms present within this gate and the chance of the trigger not being generated is virtually nil.

- **Afterpulse (π) Trigger:** This trigger is used in the $(\gamma, \pi\mathrm{N})$ experiments. Positive pions are identified by the presence of an afterpulse generated by the $\pi^+ \rightarrow \mu^+ \rightarrow e^+$ decay process. Once the PiP particle trigger has been raised, the PiP E-blocks are monitored for the occurrence of an afterpulse. The inspect time was variable and was set at 6 μs in the present experiment. If an afterpulse occurs, the π-trigger is generated. A second set of QDCs mirroring those for the prompt signals are used so that the pulse heights due to the afterpulse can measured. The time of the afterpulses are recorded in a multi-hit long range TDC.

Figure 3.15 shows the 2nd level decode sub-circuit. Like the 1st level circuit, it is based on a 4508 PLU. The PLU is strobed a fixed time after the 1st level trigger is generated. This time is to allow the second level triggers to be processed; in particular it depends on the inspect period required by the π-trigger. The PLU is programmed to identify certain combinations of inputs and can decide between two output states:

- **Accept Trigger:** the event has an acceptable set of second level triggers present. An interrupt is issued to the data acquisition computer and the ADCs are read out. On completion of read out, which takes a few milliseconds, the computer issues a reset to the circuit.

- **Fast Clear:** the event is rejected as it does not meet one of the acceptable input states (e.g. perhaps there was no afterpulse present). The Fastbus

ADCs, which had started conversion due to the 1st level trigger, are reset using the Fast Clear facility. The trigger logic is reset (unlatched) to allow a new event to be processed.

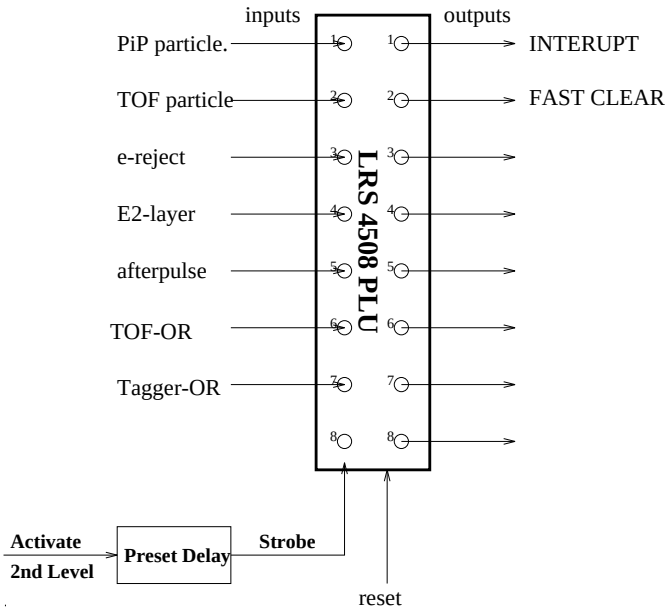

Figure 3.15: *The 2nd level trigger decode circuit*

Different trigger requirements were made depending on the nature of the run. For example, calibration runs, where an afterpulse was not required, were undertaken such that pion detection efficiency could be calculated. The main production runs were designed to optimise the collection of $(\gamma, \pi^+\mathrm{n})$ data and thus reduce dead time. The other major factor affecting dead time is the data acquisition system and this is discussed next.

3.7 Electronics: Data Acquisition

The data acquisition system controls and collects data from the electronics modules in the experiment. The task splits up into three main components:

- Initialise modules and load programmable settings e.g. discriminator thresholds and PLU lookup tables.
- Respond to event triggers (interrupts) and read out relevant modules viz. ADCs, scalers, pattern registers etc.
- Assemble raw data into recognised event format and transfer over the network for online analysis and storage to disk.

Figure 3.16 shows a schematic diagram of the electronics system. At the heart of the acquisition system is the VME crate. The crate houses an Eltec E7 single board computer - a Motorola 68040 based system running the OS9 operating system. The E7 executes the acquisition software which was coded in "C". The backplane of the crate is a VMEbus which acts as an extension of the E7's address space, facilitating memory mapped I/O between the E7 and other interface modules in the crate. These interface modules provide a two way data path to the Camac and Fastbus crate controllers. This arrangement allows software on the E7 to initialise and read out the experimental modules in a uniform and transparent way. The data collected is buffered and sent via an ethernet TCP/IP connection to a VAXstation outside the experimental hall. The VAXstation performs online analysis and stores the data to disk/tape.

Acquisition Software

The acquisition software ACQU [Ann93] running on the E7 consists of four main processes:

- **vme_supervise:** This process initialises all the modules and loads any programmable settings. It checks the integrity of the system and, if required, spawns the processes **acqu** and **store**.

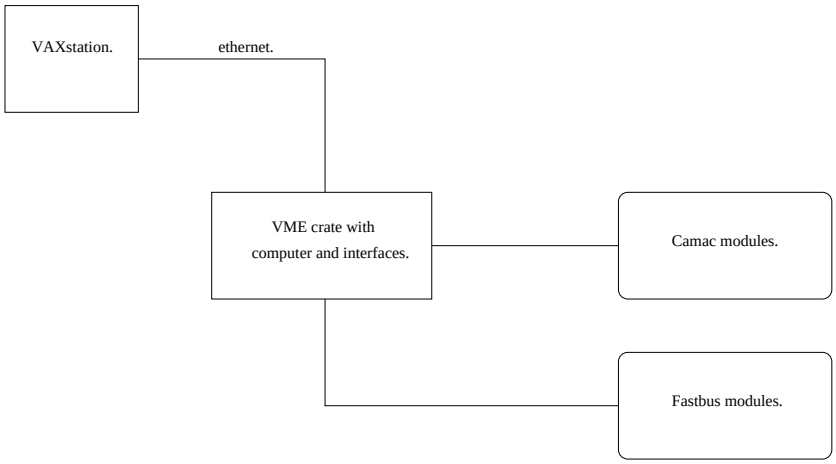

Figure 3.16: *Layout of detector electronics*

- **acqu:** The **acqu** process cycles round a readout loop. On arrival of an interrupt from the trigger logic, **acqu** proceeds to read out all the modules. The event data is a list of integer pairs giving the ADC index and contents. The data is zero suppressed i.e. ADCs with no valid data are not read out. On completion of readout, the process unlatches the trigger and returns to the beginning of the loop to await another interrupt.

- **store:** The **acqu** process fills a buffer with event information. Once this buffer is full, the **store** process is activated and proceeds to transfer the data over the network to the online analysis computer.

- **control:** The **control** process responds to requests by the experimentalist. These could involve pausing the data acquisition or starting a new run. It communicates with the other processes using intertask semaphores (OS9 events).

The software depends on the many parameter files which define the configuration of the Camac and Fastbus systems. Trigger changes can be made, for example, by editing the lookup table of the PLU and reloading this by running vme_supervise.

Online Analysis

In order to monitor the performance of the experiment, some degree of online analysis is necessary. This is performed on a VAXstation based in the experimental control room. It receives data from the VME based acquisition computer by an ethernet connection. The VAXstation also runs ACQU software written in conjunction with the VME based code. Three processes are run on the VAX:

- **vme_server:** This process makes the network connection to the VME based Eltec computer and receives data buffers from it. The data is written to disk and some fraction is passed to the **sort** process for analysis.

- **sort:** The **sort** process processes the array of ADC values which form the raw data and produces spectra which are used to diagnose the performance of the experiment.

- **control:** This process is used to display spectra generated by the **sort** process.

The above system is the same as that used offline except for the fact that offline, data will be read from tape using the **tape_server** process.

Chapter 4

Detector Calibration

A typical event obtained in the $^{12}C(\gamma, \pi^+ n)$ experiment might look like:

Event no.:256970

adc	conts	adc	conts	adc	conts	adc	conts
0	1	1	0	2	61	3	14
16	2052	17	2590	18	14082	20	1
135	332	167	617	199	6097	104	4330
417	321	421	370	446	181	462	172

The information is in the form of ADC indices and their contents in channels. The conversion of this raw data into physical quantities is the essence of the calibration process. The ADCs can be Charge to Digital Converters (QDCs), Time to Digital Converters (TDCs) and pattern registers. QDC values are proportional (once the **pedestal** has been subtracted) to the pulse heights of the photomultiplier (PM) signals. TDC values represent the time of the pulse relative to the reaction time, as obtained from the start detector. Both TDC start and stop pulses are generated from leading edge discriminators and **walk corrections** are made to correct for the time slewing introduced. To perform this correction, knowledge of the discriminator **threshold** and pulse **rise time** are required. By combining the data from each end of a scintillator block, one can derive particle energy, time and position information. In this chapter, the calibration procedure for each detector is discussed.

4.1 General Concepts

Figure 4.1 shows a typical scintillator block in the PiP-TOF system.

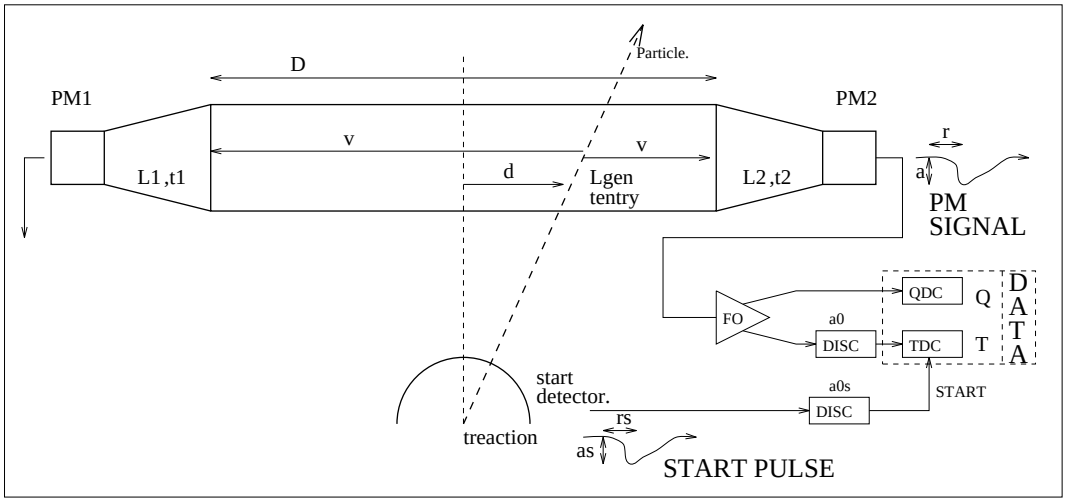

Figure 4.1: *Notation relating to a scintillator block*

The quantities used in this chapter are described as follows where the subscripts $_{1,2}$ refer to individual ends of the block:

Constants:	D	-	Length of the block.
	v	-	Velocity of light along the block.
	r_1,r_2	-	Pulse rise times (TDC channels).
	$a0_1$,$a0_2$	-	Discriminator Thresholds (QDC channels).
	p_1,p_2	-	Pedestals (QDC channels).
Raw Data:	Q_1,Q_2	-	QDC values in channel space.
	T_1,T_2	-	TDC values in channel space.
Derived:	a_1,a_2	-	Pulse heights (QDC chans).
	L_{gen}	-	Light generated by a particle in the block.
	t_1,t_2	-	Time of PM pulse relative to reaction time.
	t_{tof}	-	Time of flight of the particle.
	d	-	Hit position relative to the block centre.

4.1.1 Pedestal Subtraction

The QDC value, Q, obtained from the PM signal is not linearly proportional to the pulse height. There exists a constant offset, the **pedestal**, which must be obtained and subtracted from the raw value. The pedestal, p, arises from the integration over the gate time of the current always present at the QDC input and once obtained, the pulse height, a, can be derived:

$$a = Q - p \tag{4.1}$$

4.1.2 Light Output

The pulse heights a_1 and a_2 are proportional to the light collected at the PM tubes denoted L_1 and L_2. Relating these to the light generated by the particle, L_{gen}, is complicated by the attenuation of the light as it propagates along the block. If this attenuation is assumed exponential with decay constant k then the following relations hold:

$$\begin{aligned} L_1 &= (\frac{L_{gen}}{2})e^{-(\frac{D}{2}+d)/k} && (4.2)\\ L_2 &= (\frac{L_{gen}}{2})e^{-(\frac{D}{2}-d)/k} && (4.3)\\ L_1L_2 &= (\frac{L_{gen}}{2})^2e^{-D/k} && (4.4)\\ &= constant \times L_{gen}^2 && (4.5)\\ \Rightarrow L_{gen} &\propto \sqrt{L_1L_2} \propto \sqrt{a_1a_2} && (4.6) \end{aligned}$$

Thus the light generated is proportional to the geometric mean of the pulse heights. In reality, the attenuation is not exactly exponential and a residual droop correction must be made to account for position dependence in the geometric mean:

$$L_{gen} = constant \times [\sqrt{a_1a_2}/f_{droop}(d)] \tag{4.7}$$

The droop function must be obtained, along with the calibration coefficient, from the data. The light generated is expressed in units of electron equivalent energy (MeV_{ee}) i.e. a 20 MeV electron would generate 20 MeV_{ee} of light. The conversion to the energy lost by the particle is particle type and energy dependent, due to quenching effects in the scintillator.

4.1.3 Quenching

When a particle comes to the end of its track, the energy loss per unit length increases rapidly, as shown by the Bragg curve in figure 4.2. In plastic scintillators, the correspondingly higher ionisation density leads to a quenching effect whereby the light generated is no longer proportional to the energy deposited by the particle. The effect can be expressed in differential form [Cra70]:

$$\frac{dL}{dx} = \frac{S(dE/dx)}{1 + kB(dE/dx)} \tag{4.8}$$

where dL represents the light generated by the particle for a loss of energy dE. S is the scintillation efficiency and kB is a parameter which depends on the particular scintillator. Figure 4.3 shows dE/dx vs. E for protons and pions in NE110 plastic scintillator. Where a particle stops in the scintillator, the above relation can be integrated to give the total light output associated with a particle of energy E:

$$L = S\int_0^E d\epsilon[\frac{1}{1 + kB(dE/dx)}] \tag{4.9}$$

which can be fitted with the following parameterisation:

$$L = B(E) = a_1E - a_2(1 - exp(-a_3E^{a_4})) \tag{4.10}$$

which is known as Birk's Law. The coefficients are particle and medium dependent. Figure 4.4 shows this curve for pions and protons in NE110. In the experiment, it is the light output that is measured and the energy deposited is derived using the inverse relation:

$$E = B^{-1}(L) \tag{4.11}$$

which is performed by an iterative procedure. Where a particle does not stop in a block, knowledge of the energy after traversing the block, E_f, is required in order to calculate the energy deposited within it, ΔE. The energy deposited can be derived as follows:

$$L_f = B(E_f) \tag{4.12}$$

$$L_{tot} = L_{\Delta E} + L_f \tag{4.13}$$

$$E_i = B^{-1}(L_{tot}) \tag{4.14}$$

$$\Delta E = E_f - E_i \tag{4.15}$$

where $L_{\Delta E}$ is the measured light output from the block. Quenching effects can be quite large for protons but for lighter particles such as pions it is often sufficient simply to add a constant to the energy deposited in the last layer and apply a factor to the electron equivalent light output.

$$E_{last} = [factor \times L_{ee}] + constant \quad (4.16)$$

$$\Delta E = [factor \times L_{ee}] \quad (4.17)$$

where E_{last} is the energy deposited in the last layer and ΔE is that deposited in earlier layers.

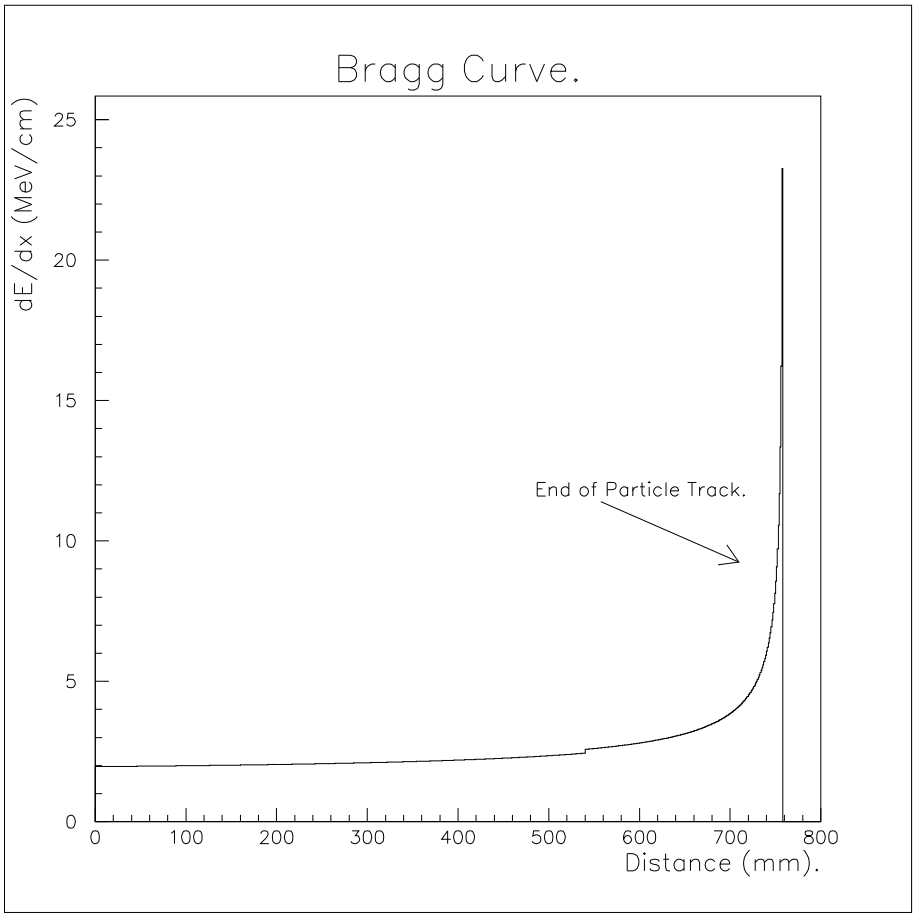

Figure 4.2: *Example of the Bragg curve for a pion stopping in NE110 scintillator*

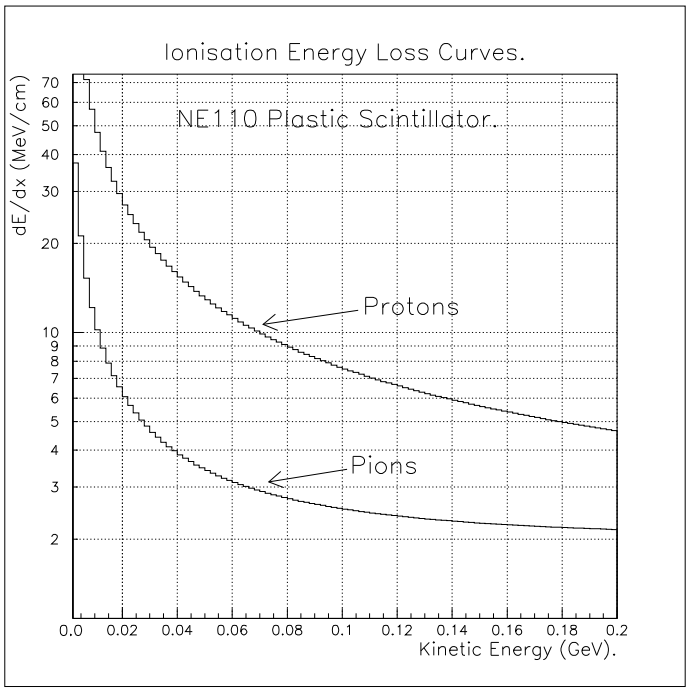

Figure 4.3: *Energy Loss Rates of Pions and Protons in Scintillator*

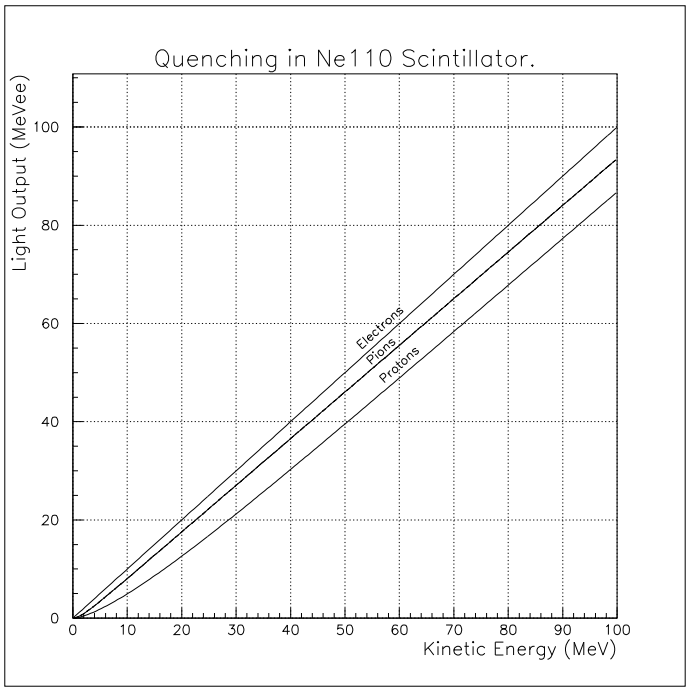

Figure 4.4: *Light output versus energy for particles stopping in scintillator*

4.1.4 Energy Losses in Dead Layers

When a particle travels between the target and the detector (and between layers of the detector) it loses energy in the material traversed. To calculate these losses, the range method was used. The particle range in the given material is parameterised using the function:

$$R = aT^k$$

where R is range and T is the particle kinetic energy. The coefficients a and k are found for each particle type and medium. The simple inverse of this parameterisation viz. $T = (\frac{R}{a})^{\frac{1}{k}}$ allows energy losses to be calculated. If T_i is the initial particle energy and d is the length of material traversed then the energy loss is derived as follows:

$$R_i = aT_i^k \tag{4.18}$$

$$R_f = R_i - d \tag{4.19}$$

$$T_f = (\frac{R_f}{a})^{\frac{1}{k}} \tag{4.20}$$

$$E_{loss} = T_i - T_f \tag{4.21}$$

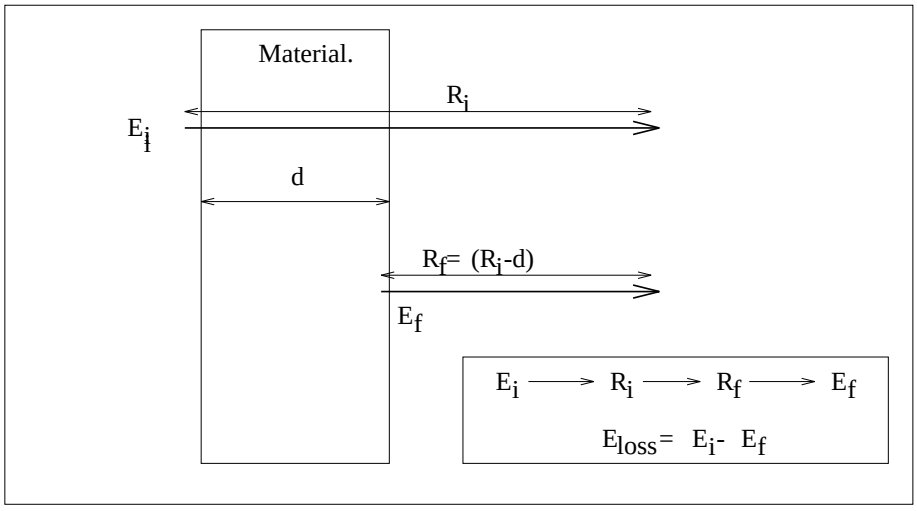

Figure 4.5: *The range method for calculating energy losses*

4.1.5 Thresholds

In order to generate a TDC stop, a PM signal must exceed its discriminator threshold. Thresholds are normally set as low as possible in order that all events of interest are detected. The main restriction is that the threshold must be above the noise level inherent in all electronic systems. The threshold value is required in order to perform discriminator walk corrections and is obtained by plotting the PM's QDC spectrum under the condition that the associated TDC has valid data. Figure 4.6 shows a QDC spectrum with and without this condition. The threshold channel can easily be read off and with the pedestal subtracted it becomes the value a_0 used in walk corrections.

4.1.6 Discriminator Walk Corrections

The recorded TDC channel, T, represents the time of the pulse relative to the TDC start. Leading edge discriminators were used to create the TDC stops which are generated when the input exceeds the discriminator threshold. This time depends on the pulse height as shown in figure 4.7 and the effect is known as walk. Pulse shapes are approximately parabolic and independent of height hence the following parameterisation can be used to correct for the walk:

$$T' = T + r(1 - \sqrt{\frac{a_0}{a}}) \tag{4.22}$$

T′ is the corrected TDC channel, the rise time r is in TDC channels and the pulse height and threshold, a and a_0, are in QDC channels. The rise time must be obtained from the data and different methods are used for each detector. This time can be expressed in physical space (nanoseconds) by applying a calibration coefficient (in ns/chan) which is obtained for each TDC by the use of a precision pulser. Once a correction for variation in the start pulse, Δt_{start}, is added, the time of the pulse relative to the reaction, t, is obtained (up to some arbitrary constant):

$$t = [T' \times (ns/chan)] + \Delta t_{start} \tag{4.23}$$

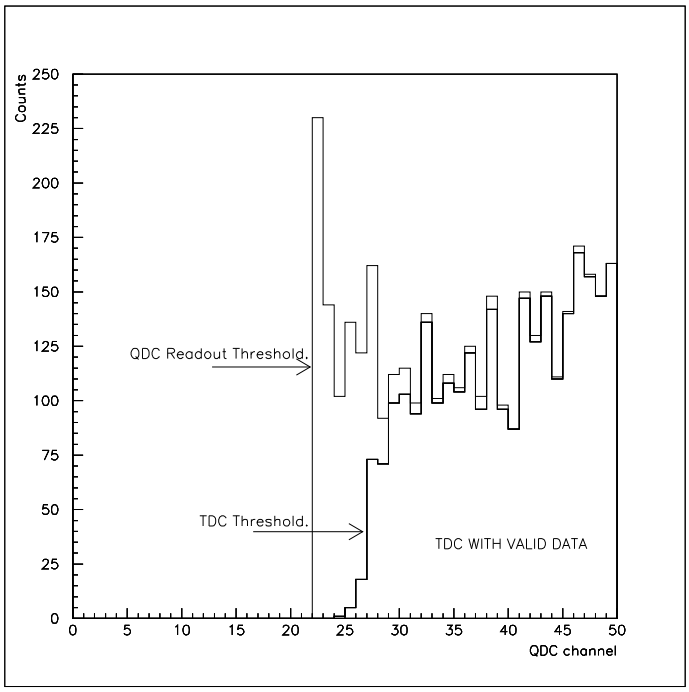

Figure 4.6: *Determination of discriminator thresholds*

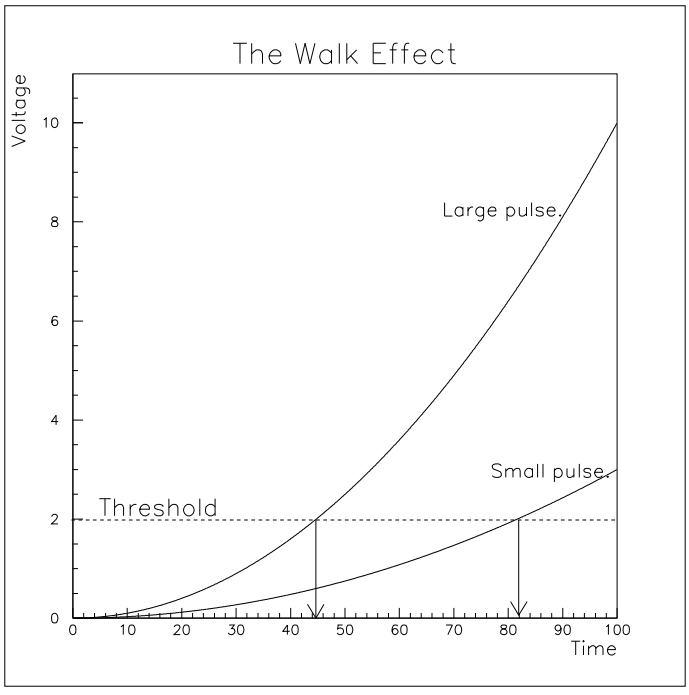

Figure 4.7: Walk corrections.

4.1.7 Time of Flight

The time at which light reaches a PM tube is related to the time the particle enters a block, t_{entry}, by the time for the light to propagate along it:

$$t_1 = t_{entry} + (\frac{D}{2} + d)/v \quad (4.24)$$

$$t_2 = t_{entry} + (\frac{D}{2} - d)/v \quad (4.25)$$

$$\Rightarrow t_{entry} = \frac{(t_1 + t_2)}{2} - \frac{D}{v} \quad (4.26)$$

$$= \frac{(t_1 + t_2)}{2} + constant \quad (4.27)$$

The time of flight can then be related to the mean of the individual times by finding the correct offset referred to as the t_{zero}:

$$t_{tof} = t_{entry} - t_{reaction} \quad (4.28)$$

$$= t_{mean} - t_{zero} \quad (4.29)$$

The t_{zero} values are obtained from the data, the method depending on the detector in question. In the TOF detector, for example, relativistic particles, which travel at the velocity of light, are used to identify the t_{zero} values.

4.1.8 Position

The particle hit position relative to the block centre can be obtained by taking the difference in pulse times:

$$t_2 - t_1 = 2d/v + constant \quad (4.30)$$

$$\Rightarrow d = (v/2).(t_2 - t_1) + constant \quad (4.31)$$

$$= [factor \times (t_2 - t_1)] + constant \quad (4.32)$$

The constant reflects cable delays etc. in the system. Notice the start pulse correction Δt_{start} cancels in the subtraction, hence only the walk corrected TDC times need be used. The factor and constant are obtained from the data.

4.2 The Start Detector

The start detector (PiP-side of the ΔE-ring) is central to the PiP-TOF-Tagger system; coincidence gates and TDC starts are generated from it. It surrounds the target and the start pulse generated by the detector is designed to occur at a fixed time relative to the reaction time, $t_{reaction}$. In practice, this is not achieved due to the transit time of the particle between target and detector, walk at the discriminators and misalignments in timing between the seven elements which constitute the detector. The corrections are put in a term Δt_{start}:

$$t_{reaction} = t_{startpulse} - \Delta t_{start} \tag{4.33}$$

$$\Delta t_{start} = \Delta t_{flight} + \Delta t_{walk} + \Delta t_{align} \tag{4.34}$$

The flight correction depends on the variation in the particles velocity over the energy range of interest. For pions between 20 and 180 MeV, the variation amounts to only 0.3 ns and was neglected. The walk correction was established by plotting the pulse height from a start detector element versus a tagger element TDC.

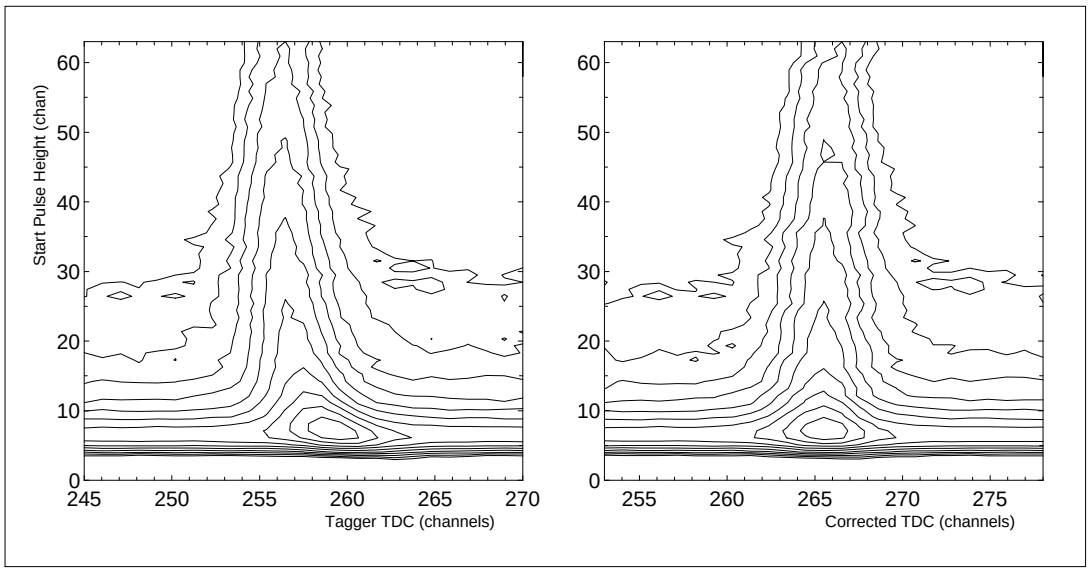

Figure 4.8: *The start detector walk correction*

The peak in the TDC spectrum reflects the difference in the transit times of the photon (from radiator to target) and electron (from radiator to Tagger Focal Plane). This should be constant as both are relativistic particles and any variation with start detector pulse height is due to walk at the discriminator. The threshold is obtained and the rise time calculated to correct the walk. Figure 4.8 shows the pulse height vs. the uncorrected and corrected TDC. This procedure is performed for all the elements of the start detector and a rise time and offset (to align the elements) is obtained for each.

4.3 The Tagger

The Tagger measures the energy of electrons residual to the Bremsstrahlung at the radiator and also their time of arrival at the Focal Plane relative to the reaction (start) time. Each Focal Plane Detector (FPD) element detects a small range of electron energies. This range is a function of the field strength of the bending magnet which is measured precisely by a Nuclear Magnetic Resonance (NMR) probe. The value is used by a ray tracing program to calculate the energy bite of each element. Given the initial electron beam energy (855 MeV), the results can be simply related to photon energies.

Electrons correlated with the absorbed photon form a coincidence peak in an element's TDC spectrum. This peak is sharpened by applying the start detector walk correction. The 352 corrected spectra are aligned to form a single peak in the combined spectrum. The prompt electrons i.e. those in the peak are selected when deriving the photon energy. The flat random background results from electrons not correlated with the photon which induced the reaction. Figure 4.9 shows the combined tagger time spectrum.

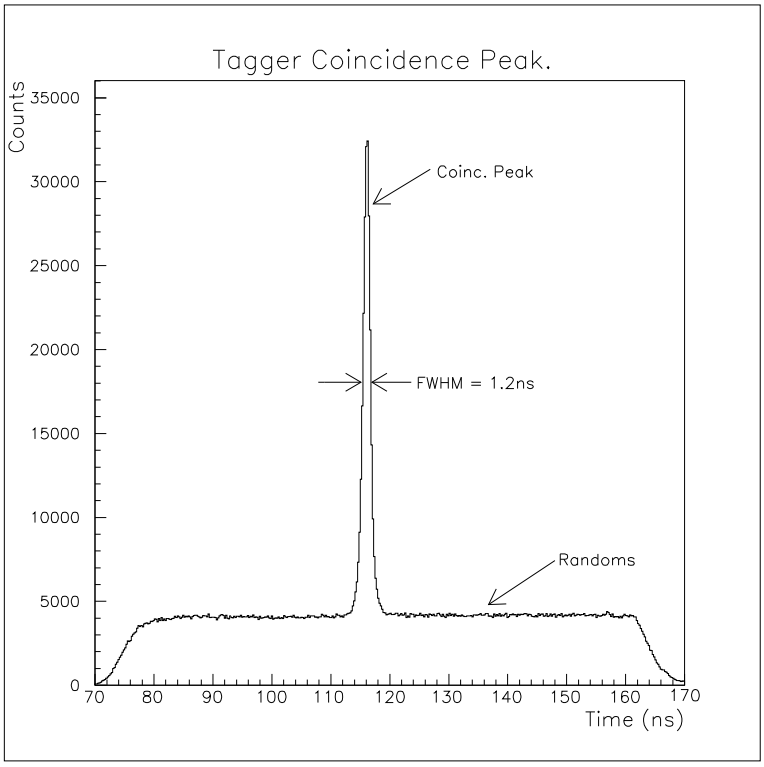

Figure 4.9: *The aligned Tagger time spectrum*

4.4 The PiP Detector

PiP covers the pion arm of the coincidence measurement. PM tubes on the ends of the scintillator blocks measure light output which is related to particle energy. The time difference of pulses at either end of a block is used to derive the hit positions from which particle angles can be calculated. The calibration process is described below.

Position Calibration

As stated in equation 4.32, the particle position is related to the time difference by two calibration coefficients. These coefficients can be obtained (for the PiP E blocks) by gating on the PiP ΔE elements and interpreting the t_{diff} spectra of the E blocks. The intersections of the distributions correspond to the joins between ΔE elements, the positions of which are known. Figure 4.10 shows how

this method was implemented. The converse process (gating on E blocks) is used to calibrate the ΔE elements. From the combined vertical and horizontal position information given by ΔE and E layers the particle's spherical polar angles (θ, ϕ) can be derived.

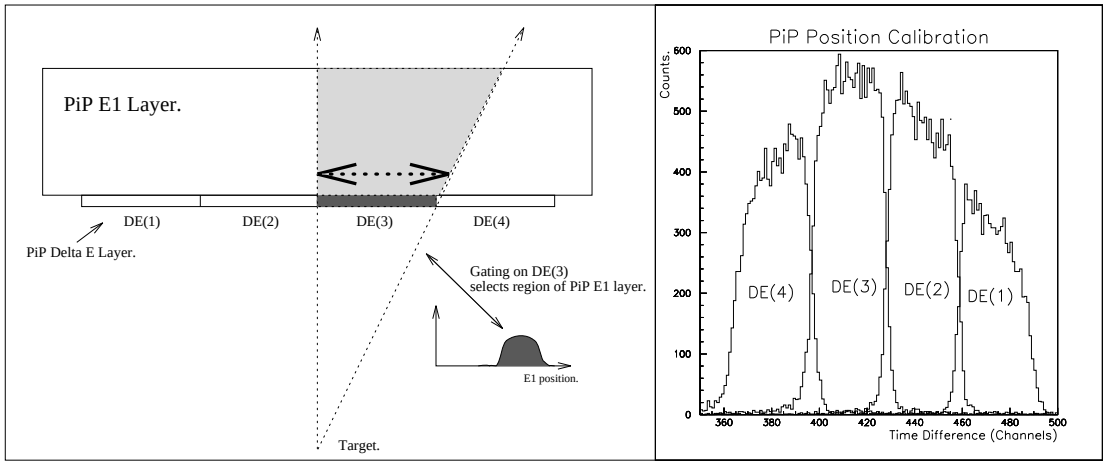

Figure 4.10: *The PiP position calibration process*

The walk corrections to the times have a second order effect - they effectively cancel when the difference is taken. Rise times were taken from a previous experiment [Cro94] as they are expected to be fairly stable.

Energy Calibration - Cosmic Rays

Cosmic rays have previously been used to calibrate scintillator hodoscopes [Bor89]. They consist mainly of ultra-GeV minimum ionising muons. A special trigger (see section 3.6) was used to record cosmic ray events simultaneously with the pion data. Figure 4.11(a) shows a cosmic ray traversing a PiP E layer. Only events that traverse a single layer are analysed. The path length through a block is calculated from the angle of the ray. The path length normalised pulse height mean $\sqrt{a_1 a_2}/cm$ displays a characteristic Landau distribution. Any dependence of this quantity on the position along the block must be due to residual droop and by plotting $\sqrt{a_1 a_2}/cm$ versus position the droop function f_{droop} can be found as is shown in figure 4.11(b). The droop corrected pulse height is proportional to the light output generated by the muons and such a spectrum is shown in figure

4.11(c). The light output half way up the leading edge of the Landau distribution is known to correspond to 1.87 MeV_{ee}/cm thus the required calibration coefficient can be extracted from the spectrum.

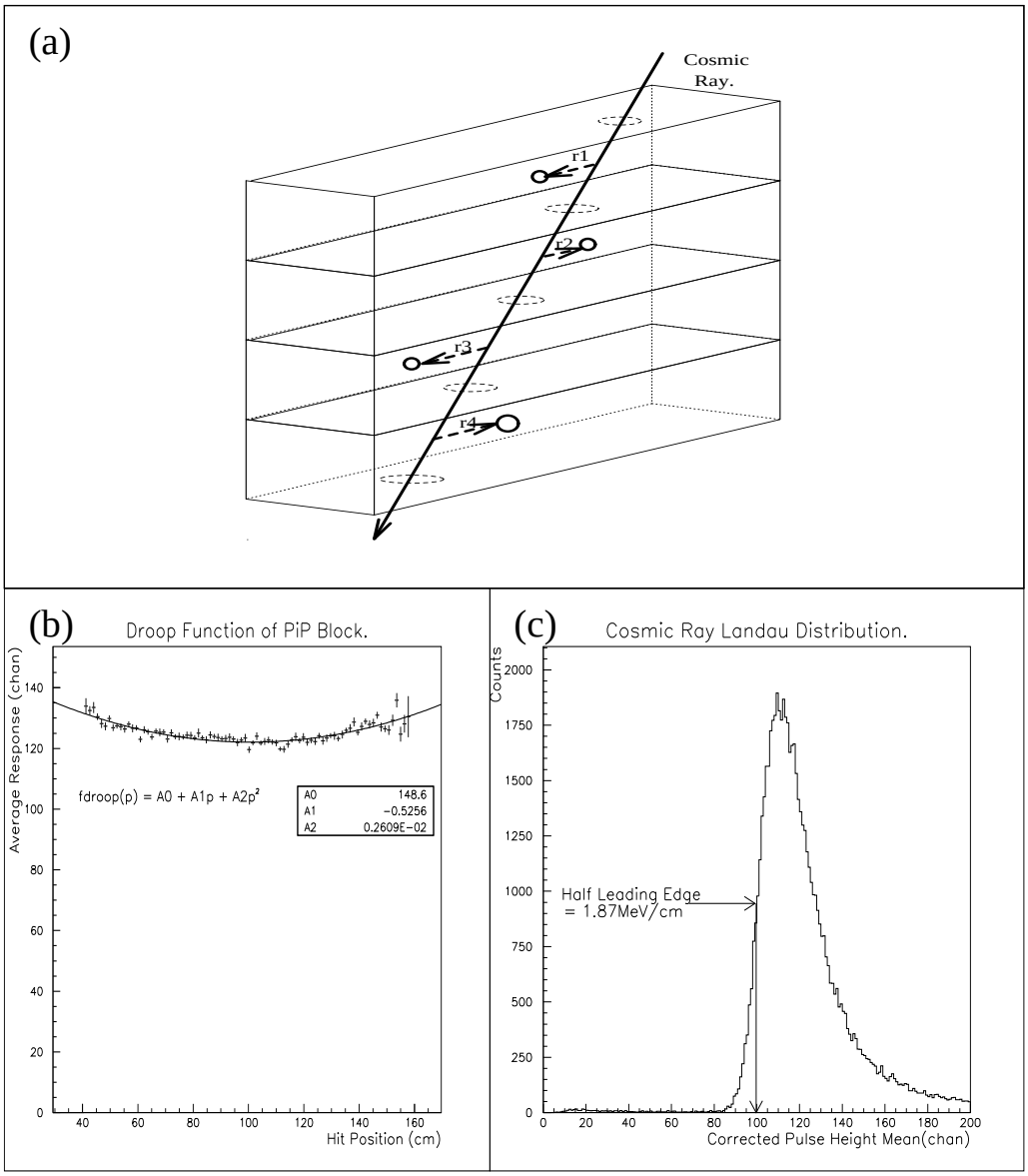

Figure 4.11: *Calibrating PiP using cosmic rays*

In converting from light output to pion energy loss, equations 4.16 and 4.17 are used. The factor can be initially estimated and later refined using the calibration data from the CH_2 target. Once the energy deposited in the final PiP layer is known, the initial pion energy can be established by working back along the track to the target, accumulating energies deposited in dead and active layers along the way. Energy losses in the dead layers (detector wrappings etc.) were calculated using the range method discussed earlier. In measuring the loss in the target, it was assumed the particle originated from the centre. This introduces an error, which combined with the intrinsic detector energy resolution forms the overall resolution of the pion energy measurement.

4.5 The TOF Detector

The TOF array covers the neutron arm of the measurement. The neutron angle is obtained by combining the position of a bar with the hit position along it. The energy of a particle is derived from its time of flight hence precise walk corrections of both the start detector and the TOF bars are required to maintain good energy resolution. Fortunately this was made possible using the LED flashers installed to monitor the gain of the PM bars.

TOF Walk Corrections

The LED flashers inject a pulse into each TOF PM tube while simultaneously generating a trigger from which the TDC start is derived. This means there is a fixed time relationship between start and stop and the TDC spectrum display a peak reflecting this. By varying the flasher intensity this peak is shifted due to walk at the discriminator. Figure 4.12(left) shows a bar's QDC plotted vs. its TDC. The pulse rise time can be extracted from this and figure 4.12(right) shows the same plot using the walk corrected TDC channel.

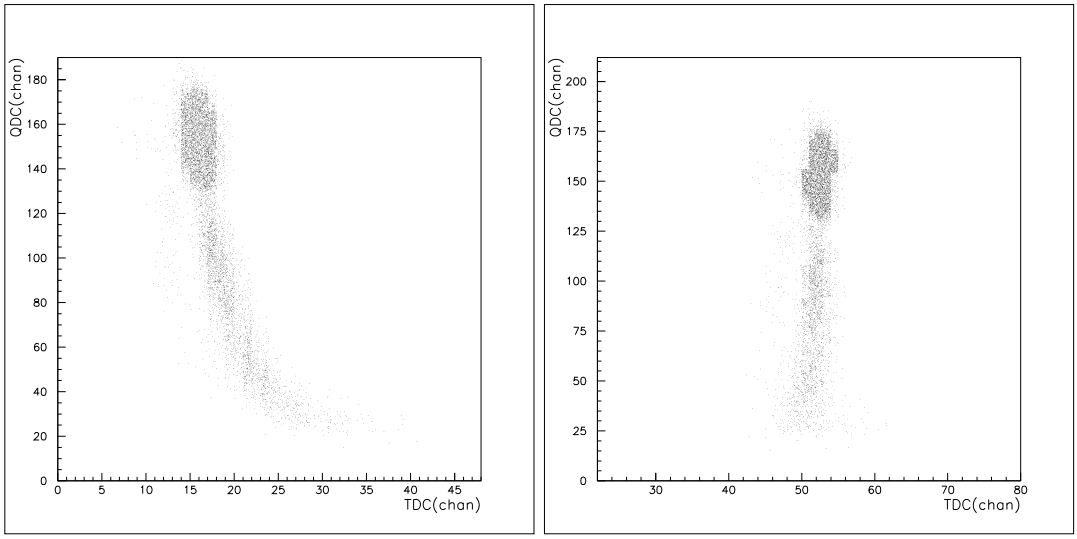

Figure 4.12: *Walk correcting a TOF bar using LED flashers*

Time of Flight

The particle time of flight from target to TOF bar is given as in equation 4.29 i.e.:

$$tof \quad = \quad t_{mean} - t_{zero} \tag{4.35}$$

where t_{mean} is the mean time from the PM tubes once walk and start corrections are made. It is expressed in nanoseconds, the conversion from channel space being achieved using a precision pulser to measure the ns/chan of each TDC. The start correction was discussed earlier and accounts for variations in the TDC start pulse. The t_{zero} is the point in the t_{mean} spectrum corresponding to zero time of flight. The t_{zero} value for each bar is obtained from the gamma flash corresponding to relativistic particles. If one makes a spectrum of the quantity:

$$t_{cal} = t_{mean} - (flightpath/c)$$

then the gamma flash is projected back onto the t_{zero} which can simply be read from the spectra. Figure 4.13 shows such a spectrum.

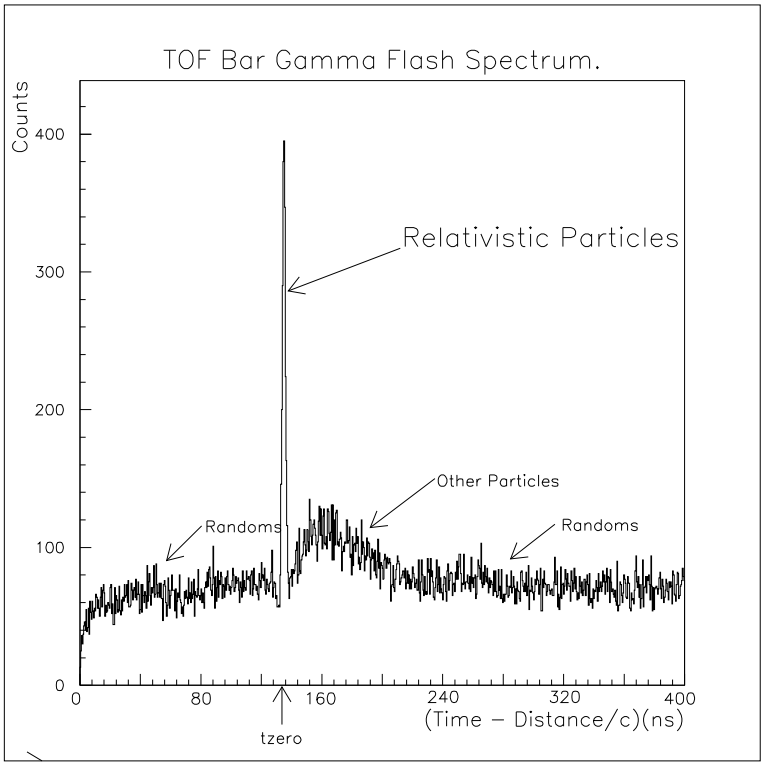

Figure 4.13: *Obtaining the t_{zero} from the gamma flash*

Energy Calibration

The kinetic energy, T, is simply related to the time of flight:

$$\beta = flightpath/tof \tag{4.36}$$

$$\gamma = \frac{1}{\sqrt{1-\beta^2}} \tag{4.37}$$

$$T = (\gamma - 1) \times m \tag{4.38}$$

where m is the particle mass. This is exact for neutral particles such as the neutron, For charged particles, a correction must be made for the fact that they slow down over the flight path and what is actually measured is the average velocity not the initial velocity.

The energy deposited in a TOF bar is of secondary importance to the time of flight measurement. It is however required to calculate the neutron detection efficiency of a bar. The efficiency depends on the threshold applied to the light output and the calibration is required such that a uniform threshold (in MeV_{ee})

can be applied to each bar in the array. The procedure is similar to that used for the PiP blocks except in the case of TOF there is no cosmic ray data available. Instead, an Am/Bi source was employed and the Compton edge at 4.2 MeV was used to obtain the necessary calibration coefficient. This can be checked by finding the punch through energy for protons incident on the TOF bars, which should be at 78 MeV.

Position Calibration

The position calibration is needed to determine particle angles. The method used is simply to plot the time difference spectrum and assume the extremes of the distribution correspond to the ends of the blocks. The actual position of each bar is measured accurately with a ultra sound device and this combined with the position along the bar allows the spherical polar angles of a hit to be determined.

4.6 Detector Performance

The calibration can be checked and the performance of the system evaluated using the free pion production p(γ, π^+n) events collected using the CH_2 target. The kinematics of the two-body final state are over defined in that once the photon energy and pion (or neutron) angle are known the other kinematical variables can be derived by applying the principle of conservation of energy and momentum. This allows the calibration to be independently checked and refinements made if required. By comparing measured and derived values, the energy and angular resolution of the detectors can be extracted. In doing this it is, however, important to unfold the error in the derived quantity. Ultimately, information from each detector is combined to form missing energies and opening angles and the resolution of these quantities are of key importance.

The kinematical variables involved are:

$$E_\gamma, E_\pi, \theta_\pi, \phi_\pi, E_n, \theta_n, \phi_n$$

In the following paragraphs, superscripts will be used to denote whether a quantity has been directly measured e.g. E_π^{meas} or derived from other quantities e.g. $E_\pi^{pred} = f(E_\gamma, \theta_n)$. In order to check the calibration, measured quantities were plotted versus their predicted values. To obtain the overall resolution of a measurement, the difference of predicted and measured values was plotted. The error in the predicted value was determined using a Monte Carlo i.e. given the error in E_γ and θ_n the error in E_π^{pred} can be deduced. This error σ_{pred} is unfolded from the error in the difference σ_{diff} (as taken from the spectrum) to give the actual resolution of the measured quantity:

$$\sigma_{meas} = \sqrt{\sigma_{diff}^2 - \sigma_{pred}^2} \tag{4.39}$$

Before the resolution can be determined the p(γ, π^+n) events must be separated out from the Carbon events.

Identifying Hydrogen Events

Figure 4.14(a) and (b) show spectra of $(\theta_n^{pred} - \theta_n^{meas})$ and $(E_n^{pred} - E_n^{meas})$ where the predicted values were derived from E_γ and θ_π.

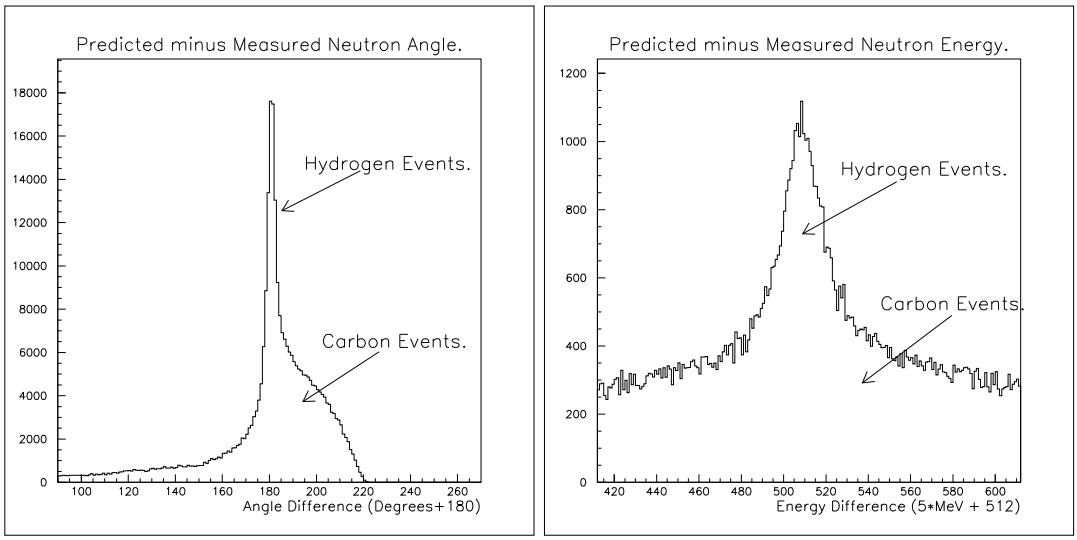

Figure 4.14: *Identifying Hydrogen $p(\gamma, \pi^+ n)$ events*

Both spectra display a peak at zero corresponding to reactions induced on the proton and a background due to the Carbon content in the CH_2 target. By cutting on these peaks, a very clean sample of $p(\gamma, \pi^+ n)$ data can be selected. This allows the quantity E_π^{pred} to be compared with the measured value E_π^{meas} for a sample of Hydrogen events, without any cut being made on E_π itself. Variants of this technique were used to obtain calibration ridges and resolutions for all the kinematical variables.

Pion Measurement

For a sample of Hydrogen events, figure 4.15 shows the calibration ridge E_π^{meas} vs. E_π^{pred}. The calibration is valid up to 180 MeV after which pions punch through the detector. The overall resolution of the pion measurement is shown by plotting the difference of these quantities as in figure 4.16. A resolution of 7 MeV FWHM is obtained for the measured pion energy.

The resolution in the pion angular measurement was determined by the po-

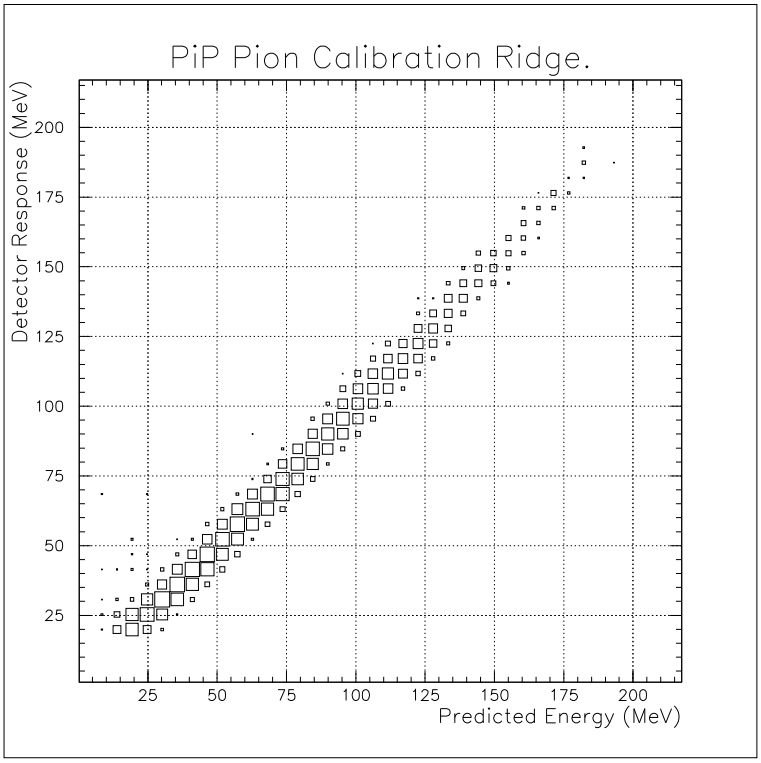

Figure 4.15: *Pion energy calibration ridge*

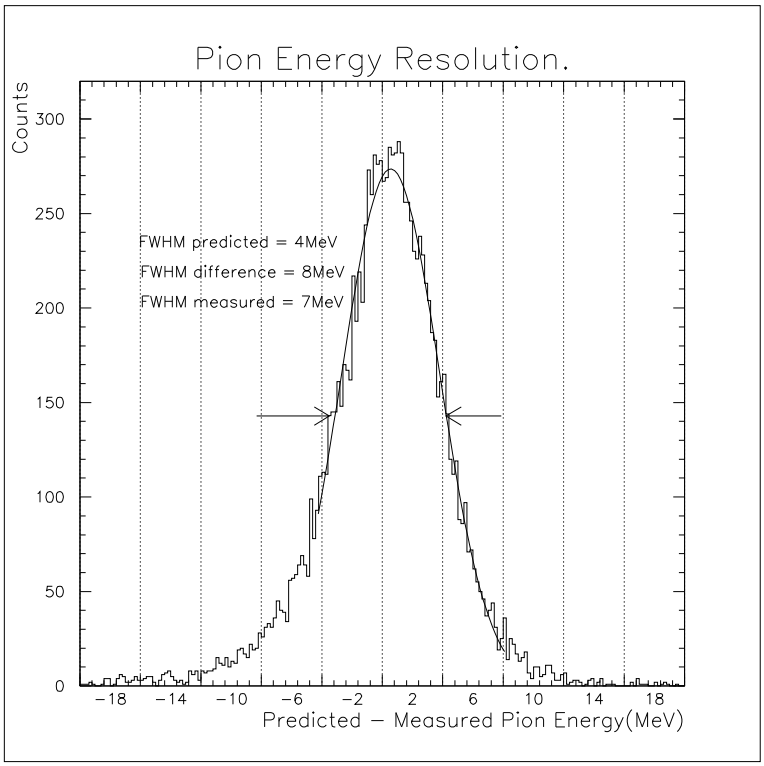

Figure 4.16: *The pion energy resolution*

sition resolution of the PiP ΔE and E layers. The θ value is largely determined by the horizontal position measured by the E layers whose position resolution of 3 cm gives an angular resolution (at 50 cm from the target) of $\Delta\theta_\pi \approx 3^\circ$. The ΔE has a much worse position resolution of 9 cm which gives an azimuthal angular resolution $\Delta\phi_\pi \approx 10^\circ$. The values correspond to the Full Width Half Maximum (FWHM) resolutions.

Neutron Measurement

As can be seen from the gamma flash spectrum, figure 4.13, the time of flight resolution of the TOF detector is 1.2 ns. For a 6 m flight path this leads to a 1 MeV neutron energy resolution at 50 MeV rising to 6 MeV at neutron energies of 150 MeV. The overall resolution i.e. folded over the energy distribution is 3.5 MeV as shown in figure 4.17.

The neutron angular resolution is mainly defined by the width of a TOF bar viz. 20 cm which at a distance of 4 m leads to a resolution of about 2 degrees.

Combined Quantities

Missing energy is defined,

$$E_{miss} = T_\gamma - T_\pi - T_n - T_{recoil} \tag{4.40}$$

$$= E_X + Q \tag{4.41}$$

For the p$(\gamma, \pi^+$n) reaction there is no recoil, hence the excitation energy $E_X = 0$ and the missing energy becomes simply the Q value for the reaction:

$$Q = M_n + m_\pi - m_p = 140.8\, MeV \tag{4.42}$$

Figure 4.18 shows a plot of the missing energy for the Hydrogen events. The resolution is 8 MeV which is sufficient to resolve the p and s shell excitation regions in the ^{12}C$(\gamma, \pi^+$n) reaction.

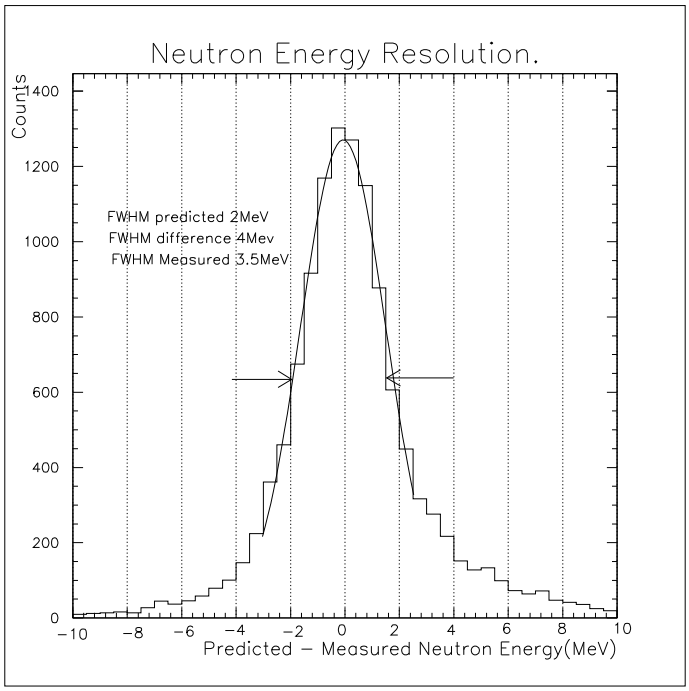

Figure 4.17: *The neutron energy resolution*

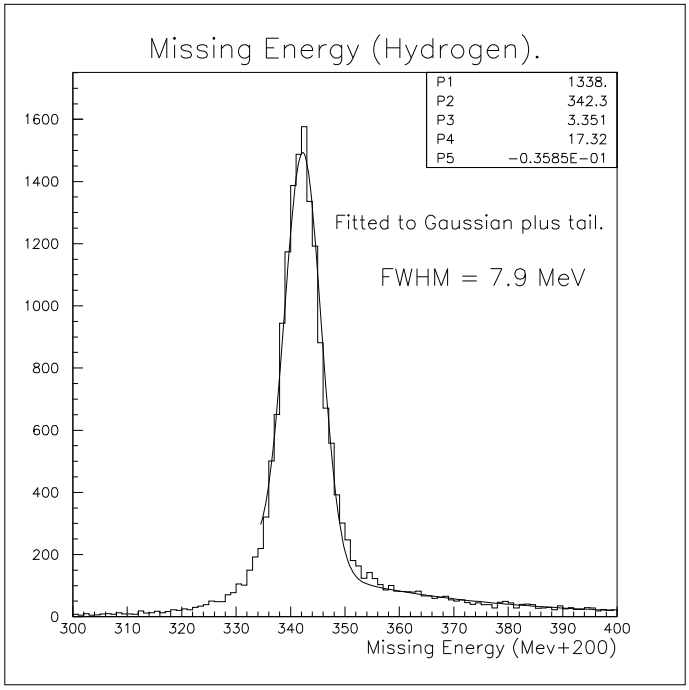

Figure 4.18: *Observed missing energy (Hydrogen events)*

Summary

Table 4.1 presents a summary of the detector parameters.

Detector	Particle	Quantity	Acceptance	Resolution (FWHM)
Tagger	γ	E_γ	115→792 MeV	2 MeV
PiP	π^+	E_π	20→180 MeV	7 MeV
		θ_π	52→128°	3°
		ϕ_π	-24→24°	10°
TOF	n	E_n	>15 MeV	3.5 MeV
		θ_n	10→150°	3°
		ϕ_n	160→200°	3°
Combined		E_{miss}	-	8 MeV

Table 4.1: *Summary of detector performance*

Chapter 5

Pion Detection Using The PiP Scintillator Hodoscope

This chapter describes the details of the pion detection technique employed in the experiment. The advantages offered by a scintillator hodoscope are discussed along side the problems associated with the detector. The methods by which these problems were overcome are described.

5.1 Pion Detection Methods

Pions are light mesons which form an isospin triplet with charges 1,0 and -1. Charged pions have mass of 139.5 MeV and decay weakly in the semi-leptonic process $\pi^{+(-)} \rightarrow \mu^{+(-)} + \bar{\nu}_\mu$ with a mean time $\tau \approx 2.6 \times 10^{-8}$s. The neutral pion is slightly lighter having mass 135 MeV and it can decay electromagnetically to two gammas with mean time $\tau \approx 10^{-18}$s. The neutral pion is detected indirectly through its decay gammas. The charged pions live long enough to be detected directly and the following methods have been used [Nag91]:

- **The $\pi^+\mu^+e^+$ Method:**
  In this technique [Aud77], the pion and also the muon into which it decays are stopped in the target and the positron, the muon decay product, is detected. The 2.2μs lifetime of the muon makes it possible to count after the beam pulse. Only the presence of the pion is established hence the

technique is inclusive and only applicable near threshold where the pion stops in the target.

- **The Activity Method:**
  Here the radioactivity of the residual nucleus is detected and selected final states can be identified giving the measurement an exclusive nature [Rao70]. An example being the reaction $^{12}\mathrm{C}(\gamma,\pi^-)^{12}\mathrm{N}$ where the final nucleus has only one stable state.

- **Pion Magnetic Spectrometer:**
  The pion magnetic spectrometer constitutes a major advance relative to the above detection techniques. Its ability to make differential cross section measurements provides a much more sensitive test to theoretical predictions than can be made using total cross sections.

- **Scintillator Hodoscope:**
  This technique, developed for this experiment, uses a plastic scintillator hodoscope to measure the pion angle and energy deposition. Compared with the spectrometer it offers a larger solid angle and energy bite. The hodoscope, however, can not achieve the same energy resolution as a spectrometer. The technique is less clean and methods need to be developed to accomplish pion charge identification and unscramble the effect of inelastic scattering of the pions in the detector. The description of these methods form the content of this chapter.

5.2 Pion Identification

Identification of pions in the PiP detector was achieved in two stages. Firstly, a dE-E plot was used to separate pions from electrons and protons. For a given total kinetic energy E, particles of different mass will deposit different amounts of energy dE in a thin transmission detector. Figure 5.1 shows a plot of the energy deposited in the PiP transmission detector dE versus the total energy deposited E. The ridge corresponding to pions can be identified and selected for analysis.

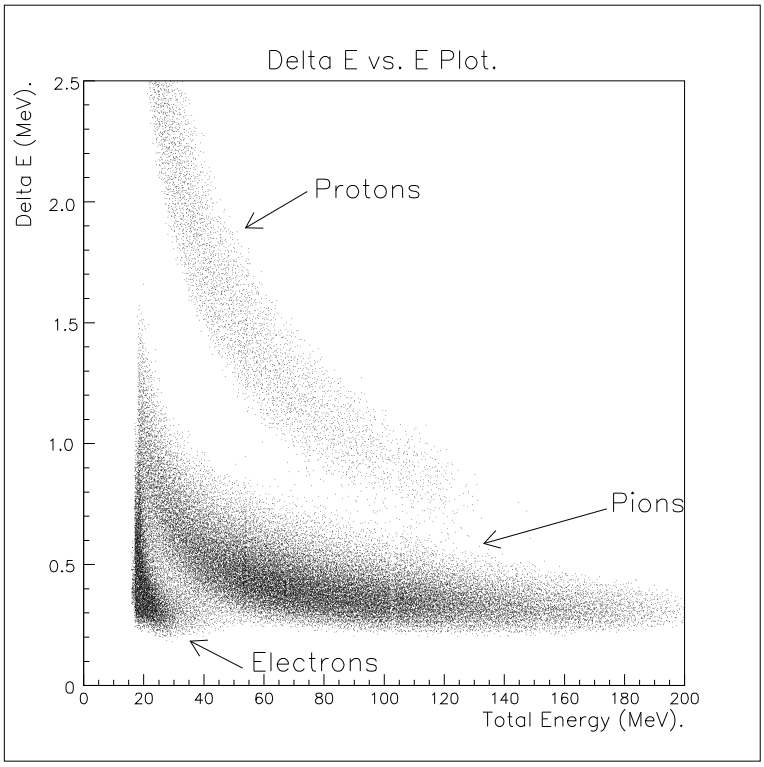

Figure 5.1: *Particle ridges in a plot of ΔE vs. E*

The events in the pion ridge correspond to positive and negative pions. The key to the identification of the positive pions lies in their decay mechanism:

$$\pi^+ \rightarrow \mu^+ + \bar{\nu}_\mu \tag{5.1}$$

$$\mu^+ \rightarrow e^+ + \bar{\nu}_e + \nu_\mu \tag{5.2}$$

Once in the detector, the negative pions are quickly absorbed onto nuclei releasing 140 MeV of energy whereas the positive pions decay into muons. The

lifetime for this process, 26 ns, is too small to be resolved by the detector and the 4.2 MeV kinetic energy of the muon is combined with that of the pion. The positive muons associated with the positive pions remain at rest until they decay into positrons. This decay has a lifetime of 2.2 μs and can be resolved by the system. There are three particles in the final state, the positron and two neutrinos. The kinetic energy distribution of the positron is shown in figure 5.2 [Bur79] which shows that the vast majority of positrons are of quite high energy and thus should have no problem overcoming the detector thresholds which are of the order of a few MeV for each block.

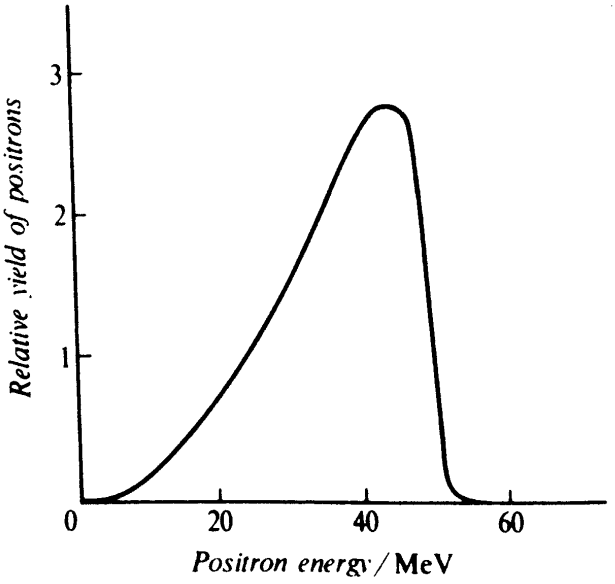

Figure 5.2: *Kinetic energy distribution of muon decay positrons*

The hardware used to identify the afterpulses is discussed in Chapter 3. An LRS2277 multi-hit long range TDC was used to measure the decay time. The TDC is started by the PiP particle trigger and stopped each time an afterpulse occurs in one of the E blocks. Random afterpulses occur if another particle enters PiP within the 6 μs inspect period triggered by the initial particle. Two methods were used to suppress these randoms:

- **Target Veto:** Signals from the PiP-side of the ΔE-ring were used to veto afterpulses, since they suggest the afterpulse was due to a particle coming

from the target and not the decay of the pion.

- **Position Consistency:** In the offline analysis, the block in which an afterpulse occurs is compared with the block in which the pion stops. If they are not even neighbours, this suggests that the afterpulse is unconnected with pion.

These techniques reduce the random content considerably. The decay spectrum allows a quantitative assessment of the residual random content to be made. The multi-hit TDC can record the times of up to three afterpulses. This means that the combined decay spectra displays an exponential decay curve due to the positive pions superimposed on a flat random background. If a normal TDC were used, the randoms would form a exponential distribution. From the spectrum, the percentage of events where the afterpulse was random can be calculated as follows. Defining the total number of events as N_{events} and the number with a decay afterpulse detected as N_{decay}, one proceeds to fit the decay spectrum, as shown in figure 5.3, with the function:

$$f(t) = A_0 + A_1 e^{-t/\tau_\mu} \tag{5.3}$$

where τ_μ is the 2.2μs muon decay time. In fact, the decay curve is not purely exponential due to the fact that the muon decay is the second in the $\pi^+\mu^+e^+$ chain. The distortion is only observable at small times due to the pion's 26 ns lifetime and is neglected in these calculations. If the afterpulse inspect circuit detects afterpulses within the time interval (t_1,t_2) then the number of afterpulses connected with pion decays is:

$$\begin{aligned} N_{decay} &= A_1 \int_{t_1}^{t_2} e^{-t/\tau_\mu} dt & (5.4) \\ &= N_{afterpulse} - A_0(t_2 - t_1) & (5.5) \end{aligned}$$

where $N_{afterpulse}$ is the total number of afterpulses in the spectrum.

There remains a small correction factor to be applied before one can ascertain the number of positive pions detected, N_{π^+}. This is due to the fact that a pion may have decayed outside the inspect period (t_1, t_2) but a random afterpulse may have occurred within it, thus satisfying the trigger requirement. If the pion creation

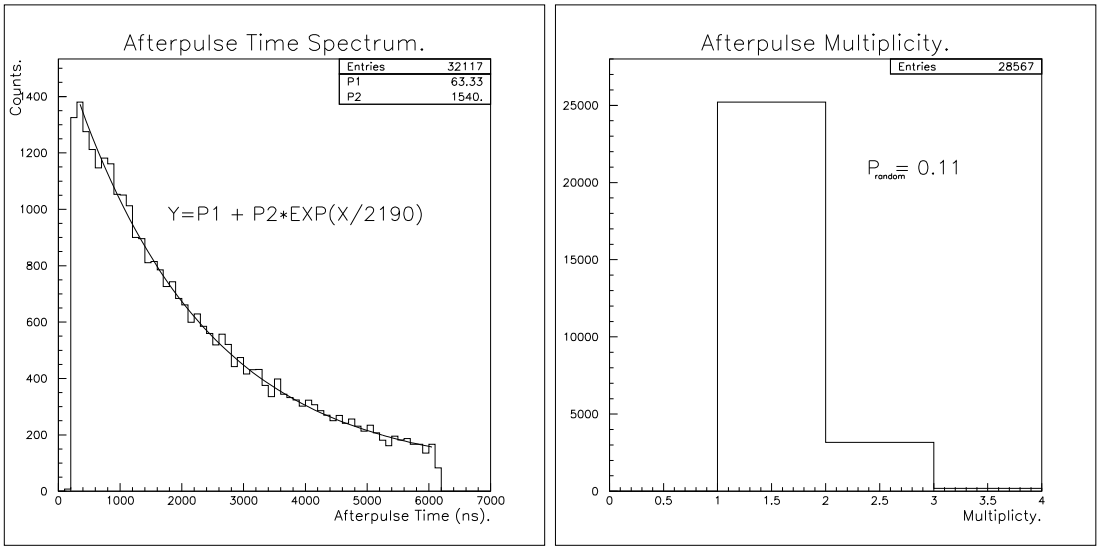

Figure 5.3: *Afterpulse Time and Multiplicity spectra*

time is denoted t_0 then the proportion of decays occurring inside the inspect period is:

$$F_{inspect} = \int_{t_1}^{t_2} e^{-(t-t_0)/\tau_\mu}\, dt \tag{5.6}$$

If the probability of a random occurring inside the inspect period is P_{random}, the proportion of decays outside then the inspect period but nevertheless detected is simply the product of (1-$F_{inspect}$) and P_{random}. The actual number of pions detected N_{π^+} and the ratio of positive pion events R_{π^+} are therefore given by the relations:

$$N_{\pi^+} = N_{decay}(1 + \frac{P_{random}(1 - F_{inspect})}{F_{inspect}}) \tag{5.7}$$

$$R_{\pi^+} = N_{\pi^+}/N_{events} \tag{5.8}$$

The remainder (N_{events} - N_{π^+}) correspond to events where the pion charge has been misidentified. The data can be corrected by carrying out a random subtraction method discussed in the next chapter. The proportion of misidentified events was about 10% of the total data set, but where cuts were made e.g. on the excitation energy of the residual nucleus, this proportion is dramatically reduced.

5.3 Pion Energy Measurement

As a pion traverses the scintillator blocks which form the PiP detector, it loses energy through ionisation of the medium which in turn generates scintillation light proportional to this energy loss. The collection and measurement of this light is the basis of the determination of energy deposited in the detector. The measurement should correspond to the pion's initial energy however this is not true if one of the following occurs:

- The pion does not stop in the detector. This can happen if the pion has enough energy to simply punch through the whole detector, which in PiP corresponds to pions above 180 MeV. Alternatively, if a pion scatters in the scintillator it may escape out the sides of the detector. In these cases, the initial pion energy cannot be reconstructed because the energy with which the pion leaves the detector is unknown.

- The pion undergoes an inelastic process with the scintillator material. In particular, the Carbon nuclei of the plastic scintillator. Energy is absorbed or released in the process. Hence, the energy deposited in the detector will not correspond to the initial pion energy.

The first problem can be easily overcome, given the fact that the detection of the decay afterpulse guarantees the pion stopped in the detector. The second problem is more complex and the challenge for the analyst is to reject events where inelastic scattering has occurred. In order to understand the nature of the problem the detector was simulated using the GEANT package.

5.3.1 Detector Simulation Using GEANT

The PiP detector's response to pions was simulated using the CERN library package GEANT [Bru82]. The detector geometry and materials were loaded into the package and an event generator 'fired' pions at the detector. The pions were tracked through the detector and any decays were recorded and their products also tracked. Physical processes could be switched on and off in order to isolate the effect of each. The response of the detector for pions of differing energies and

angles could be estimated. The information obtained proved valuable in planning the experiment and guiding the analysis.

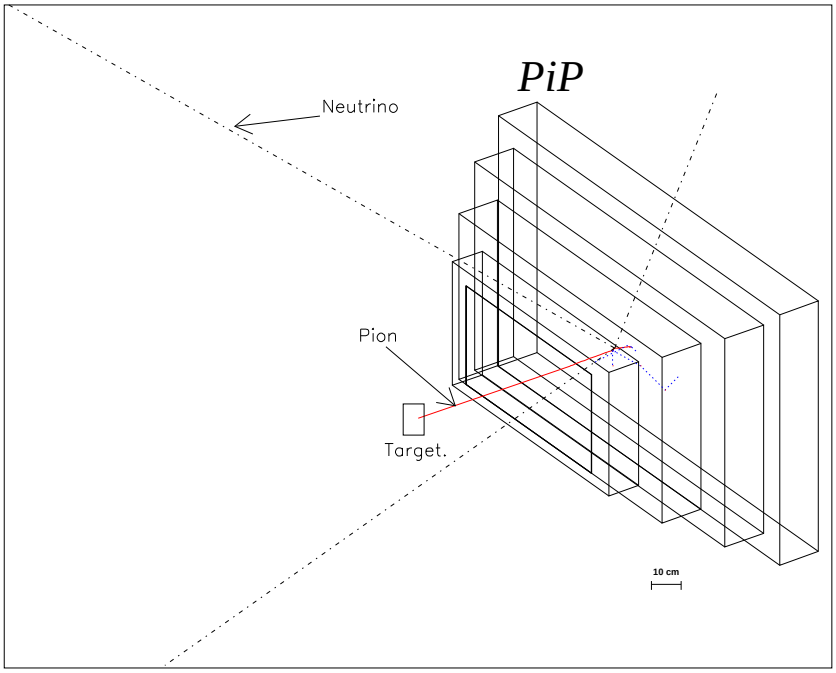

Figure 5.4: *A simulated event in the PiP detector*

Figure 5.4 shows the geometry which was loaded into GEANT and a typical event with the pion and its subsequent decay products. The response of the detector to pions of 50, 100 and 150 MeV is shown in figure 5.5. As the pion energy increases it is more likely to undergo inelastic scattering and the response is degraded i.e. less pions are in the peak corresponding to a correct energy measurement.

The pion decays to a muon which subsequently decays to an electron or positron depending on the pion charge. These decay curves are shown in figure 5.6(left) for both positive and negative pions. The negative pion case shows virtually no decays in the inspect period as the pion rapidly undergoes an interaction with the medium. The response of the detector to particles with an afterpulse is shown in figure 5.6(right) where one can see that those negative pions that do generate an afterpulse have undergone inelastic scattering and can be rejected by other methods (as discussed next).

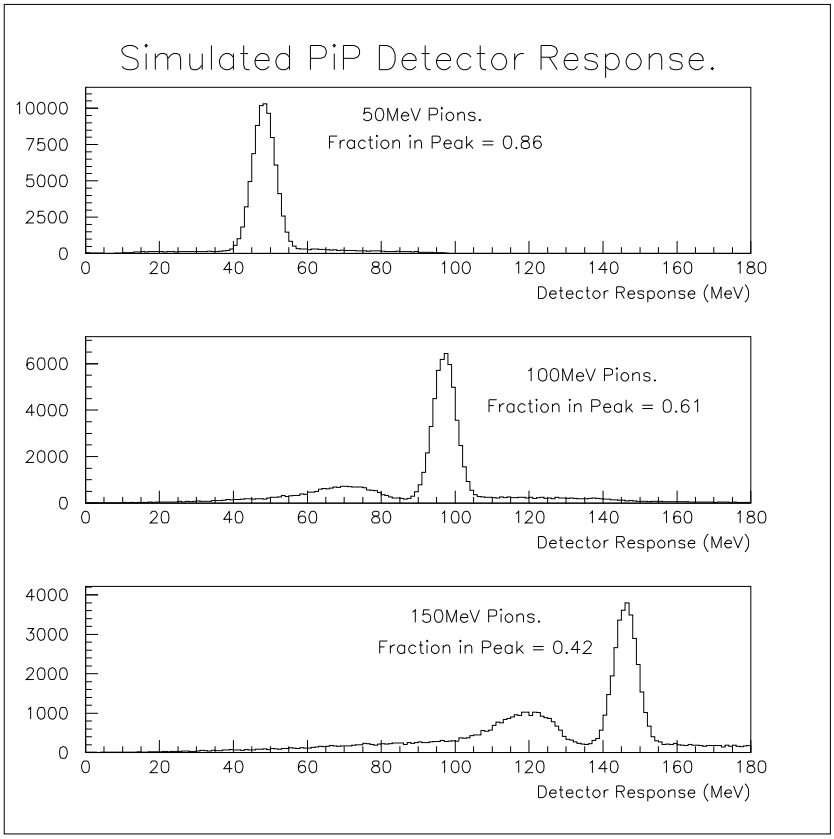

Figure 5.5: *Simulated PiP response to 50, 100 and 150 MeV positive pions*

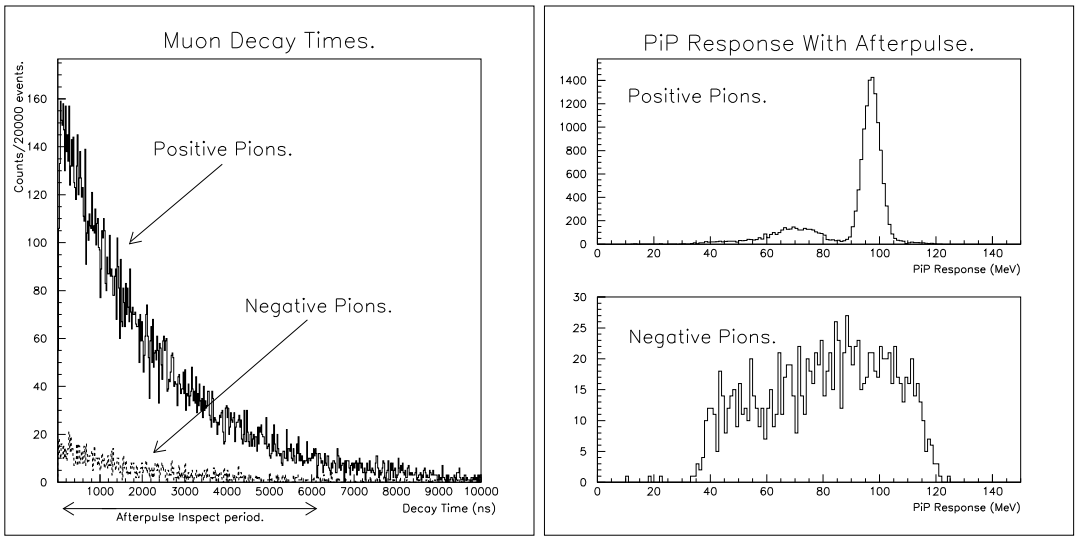

Figure 5.6: *PiP response to positive and negative 100 MeV pions*

5.3.2 Rejecting Inelastic Events

In order to be an effective detector, a method is needed to identify events where the pion has undergone inelastic scattering. This was achieved by checking to see if the energy loss in individual PiP layers is consistent with a pion coming to rest by ionisation alone. Figure 5.7 shows the predicted energy loss in each PiP layer versus initial pion energy. Any deviation from these values which is larger than the 20% one might expect due to straggling suggests the pion has scattered inelastically and the event should be rejected.

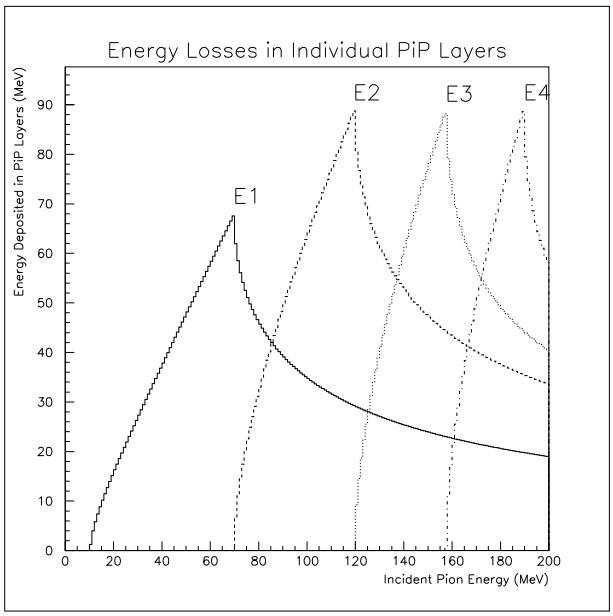

Figure 5.7: *Predicted energy losses in individual PiP layers*

The predicted energy losses could have been used to compare with the detector energy losses in each layer, but this proved over complex due to dependencies on particle angle and the dead layers between the blocks. Instead, the predicted values were obtained from the data itself by using the calibration reaction $p(\gamma, \pi^+n)$ to obtain a sample of events which were known to be 'clean' i.e. the PiP energy response was as predicted by the two body kinematics of the reaction. Using these events, a plot of the energy loss in a layer versus total pion energy was made. Most of the angular dependency was removed by multiplying the energy loss in a layer by a path factor $(1/\sin\theta\cos\phi)$ which represents the effective thick-

ness of a layer for a pion with spherical polar angles θ and ϕ. Sets of parameters were then obtained for given pion energy and angle intervals. For example, figure 5.8 shows the path factor normalised response of the E1 layer for events where the pion stops in the E2 layer. The ridge is fitted to a polynomial and the coefficients recorded. In the real analysis, this polynomial is used to generate the predicted loss on the E1 layer given the total energy deposited. If the difference between predicted and measured E1 energy loss is greater than certain limits, the event is regarded as unclean and rejected under the assumption that inelastic scattering has occurred.

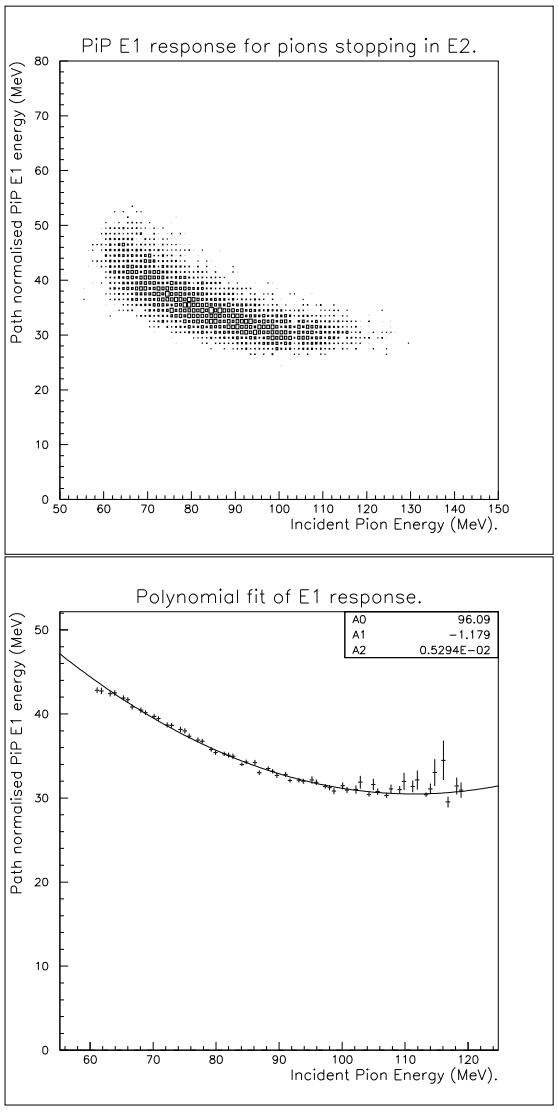

Figure 5.8: *PiP E1 layer response for 'clean' pion events*

5.4 Pion Detection Efficiency

The algorithm described above is used to reject pion events corrupted by inelastic scattering. In order to calculate cross sections, it is necessary to know what proportion of pion events are undetected either due to lack of an afterpulse or because of inelastic scattering. This quantity is the pion detection efficiency, ϵ_{π^+}. If the probability of a positive pion generating an afterpulse is $P_{\pi^+}(afterpulse)$ and the probability that it does not inelastically scatter is $P_{\pi^+}(clean)$, then the probability that it generates an afterpulse and does not scatter is given by the law of conditional probability:

$$\epsilon_{\pi^+} = P_{\pi^+}(afterpulse \cap clean) \tag{5.9}$$

$$= P_{\pi^+}(afterpulse).P_{\pi^+}(clean|afterpulse) \tag{5.10}$$

where $\mathrm{P}_{\pi^+}(clean|afterpulse)$ is the probability that the pion is 'clean' given that it has generated an afterpulse.

The two probabilities were evaluated separately, principally because there is more CH_2 data with the afterpulse trigger requirement. Firstly, the probability of an afterpulse occurring, $P_{\pi^+}(afterpulse)$, was evaluated as follows:

- CH_2 data with afterpulse trigger deactivated was collected.
- Events corresponding to the $\mathrm{p}(\gamma, \pi^+\mathrm{n})$ reaction (Hydrogen events) were selected by cutting on the peak of the predicted minus measured neutron energy spectrum, where the neutron energy was derived from the neutron angle i.e. independently of the PiP detector.
- For a given range of predicted pion energies the number of neutrons in this peak was counted and denoted N_{neut}. The spectrum was recreated for those events which generated an afterpulse and the new number in the peak denoted $\mathrm{N}_{neut}^{afterpulse}$. The probability of an afterpulse is simple:

$$P_{\pi^+}(afterpulse) = \frac{N_{neut}^{afterpulse}}{N_{neut}} \tag{5.11}$$

The observed afterpulse efficiency is shown in figure 5.9 as a function of pion energy. It falls off at high pion energies, presumably due to the fact that as

inelastic scattering increases there is more chance of the pion being absorbed or scattered out of the detector hence being unable to generate an afterpulse. The curve was fitted to a cubic polynomial for use in the analysis.

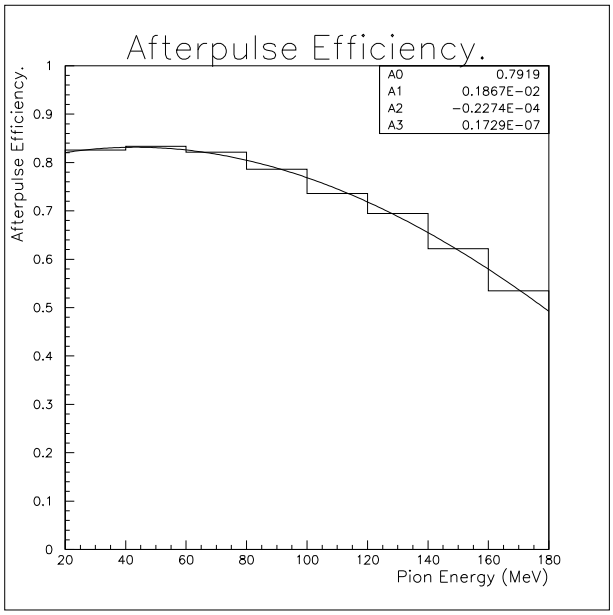

Figure 5.9: *Pion afterpulse efficiency versus pion energy*

The second quantity, $P_{\pi^+}(clean|afterpulse)$, was measured using the following method:

- CH_2 data with the afterpulse trigger activated was collected.
- Hydrogen events were selected as above using the predicted minus measured neutron energy spectrum. For a given predicted range of pion energies the number of neutrons in the peak were counted and denoted $N_{neut}^{afterpulse}$.
- The proportion of 'clean' events was found by counting the number of events in the peak of the missing energy spectrum, denoted $N_{\pi^+}^{clean \cap afterpulse}$. The required probability is simply:

$$P_{\pi^+}(clean|afterpulse) = \frac{N_{\pi^+}^{clean \cap afterpulse}}{N_{neut}^{afterpuse}} \tag{5.12}$$

An example is shown in figure 5.10(left) and the results as a function of pion energy are shown in figure 5.10(right). The curve is also fitted to a polynomial for ease of use in the analysis.

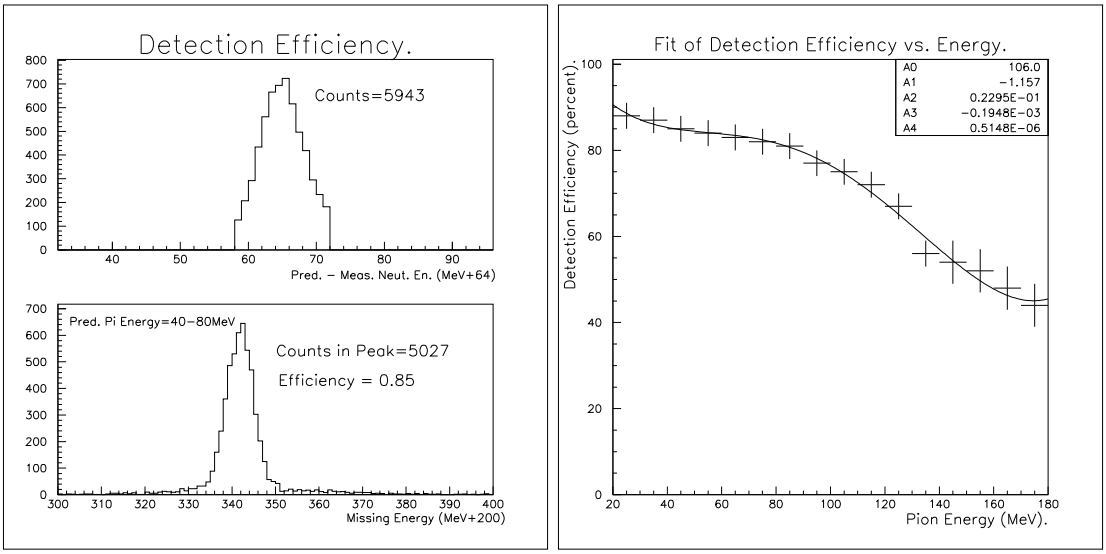

Figure 5.10: *Probability of inelastic scattering for afterpulse events*

One final point of interest is to look at the probability of an afterpulse given that the event is 'clean', $P_{\pi^+}(afterpulse|clean)$. One would expect almost all 'clean' pion events to generate an afterpulse as the pion has not been absorbed or scattered out of the detector. The reason that an afterpulse can be undetected is if it came outside the inspect period which was from 100 ns to 6 μs. The proportion of decays inside this period is simply:

$$F_{inspect} = \int_{100}^{6000} e^{-t/\tau_\mu} dt \quad (5.13)$$

$$= 0.89 \quad (5.14)$$

where the muon decay time τ_μ is 2190 ns. This value of 89% agrees exactly with that observed, which was found by looking at the missing energy peak for events with and without an afterpulse. This is shown in figure 5.11. The result was also found to be independent of pion energy.

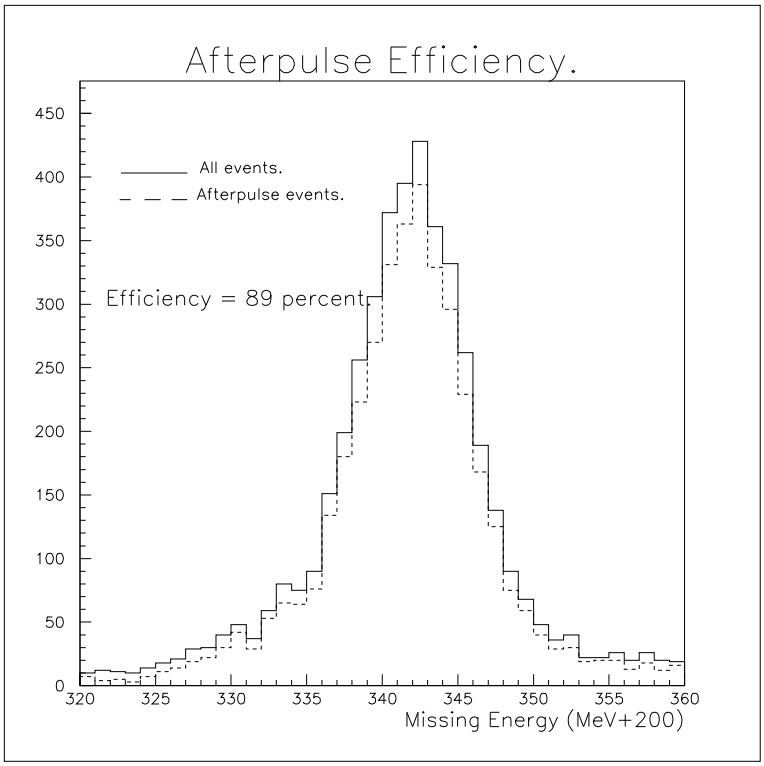

Figure 5.11: *Afterpulse efficiency for clean pion events*

Chapter 6

Data Analysis

This chapter describes the method by which single and double arm differential cross sections for the exclusive $^{12}C(\gamma, \pi^+n)$ reaction were extracted from the data collected. Once the π^+n channel is selected, the procedure involves accounting for various particle detection efficiencies and performing randoms and background subtractions. Knowledge of photon flux and target density are also essential to make the absolute cross section measurement.

The analysis was performed using the ACQU package [Ann] and spectra were loaded into the CERN PAW application mainly for presentational purposes. Thousands of lines of code were written to perform the analysis and a general description of the approach taken is given below.

6.1 Analysis Code

The ACQU analysis package was developed at the Kelvin Lab, University of Glasgow. The package provides the general features required in performing any data analysis viz. tape handling, reduced data output and spectrum storage and display facilities. Code specific to a particular experiment must be developed by the user in the form of 'C' user defined spectrum (uds) functions. For the purposes of analysing the PiP-TOF-Tagger (γ, π^+n) experiment the "experim" uds was developed. In order to meet the challenge of analysing a system involving 4 detectors containing a total of 500 scintillator bars corresponding to $\approx$ 1000 ADC channels,

a highly structured, uniform and object oriented approach to the problem was required.

Four types of object were identified in the problem:

- The Experiment - the whole system containing detectors.
- The Detector - a particle detector containing sub-units.
- The Layer - a sub-unit of a detector e.g. a layer in PiP.
- The Block - a scintillator block.

The objects form a nested tree structure - the experiment contains detectors, each of which contains layers, each of which contains blocks. Figure 6.1 shows how the present experiment was organised in this fashion.

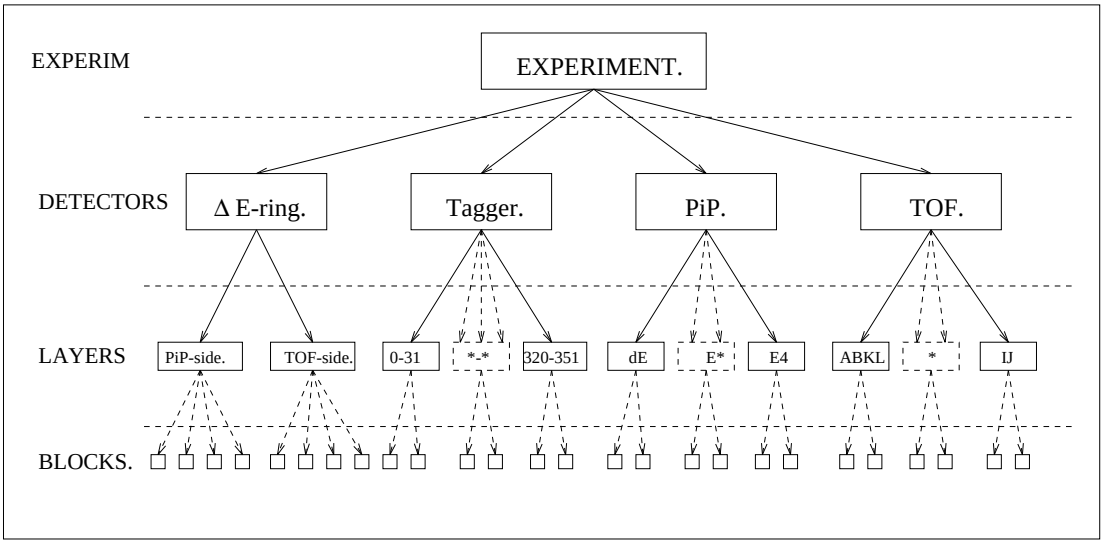

Figure 6.1: *The structure of the experiment and its sub-systems*

There are a vast number of calibration coefficients and event details associated with the system and a data structure was developed which mirrors the above nested structure. A sub-structure was defined for each object, one of the entries being an array of pointers to the objects below it in the tree. The object oriented approach was maintained in the coding where functions were written to operate on specific object types. The uniformity of the data structure allowed for the

maximum reusability of code. For example, the fact that both PiP and TOF block information were stored in the same type of data structure meant that the same function could be used to analyse both. As a rule, when a function is analysing an object it only works with information contained within that object in the nested structure. This avoids 'tangled' data interdependencies e.g. when analysing a PiP layer, information relating to that layer and the blocks within it is used and no reference is made to other layers or detectors. This approach allows for a very elegant looping round of the system. The code basically loops round the blocks in a layer, the layers in a detector and the detectors in the system until finally the whole system is analysed.

The code fills the data structure with event information and then 'child' uds functions can be called to access desired entries in the structure and pass them to ACQU for histogramming.

6.2 Data Reduction

The aim of the data reduction process is to isolate those events corresponding to the exclusive $(\gamma, \pi^+\mathrm{n})$ process. Although part of this process is achieved in hardware by the event trigger, events from other reaction channels still form the majority of the data. It is always safer to reject events in the offline analysis as a strict hardware trigger runs the risk of rejecting desired events.

The first step in the reduction is to remove the various calibration events such as cosmic ray and LED flasher data. This is done by inspecting the contents of the pattern registers which record the trigger type. These pattern registers are actually the LRS4508 PLUs discussed in chapter 3, which allow the state of their inputs to be read out by the data acquisition system. The next stage is to identify positive pions in PiP and neutrons in TOF.

PiP Pion Selection

As discussed in chapter 5, pion selection is made by cutting on the pion ridge in the ΔE-E plot shown in figure 3.14. The requirement of an afterpulse (which is performed in hardware) selects positively charged pions. There was a large back-

ground of low energy electrons recorded and in order to remove them a software threshold was applied to the pion kinetic energy, T_π >20 MeV. Inspection of the afterpulse decay spectrum showed the resulting sample to be 90% pure π^+ data. The contamination can be removed by a randoms subtraction method discussed later.

TOF Neutron Selection

All particles produced at the target and entering TOF must pass through the TOF-side of the ΔE-ring. Charged particles generate a signal in one of the detector elements and it is by the absence of this signal that neutral particles (in this case neutrons) are identified. Photons can be rejected due to their relativistic velocities. Figure 6.2 shows a time spectrum of one of the ΔE elements; the peak corresponds to charged particles correlated with the PiP particle trigger. The reduction process demands that none of the elements have any hits in the peak. Only hits in the peak are considered, the background is due to uncorrelated randoms and their component underneath the peak actually causes true neutron events to be rejected thus a correction for this must be made.

One final point must be made. Even though a π^+ and a neutron have been identified, the experimentalist does not know whether or not other particles were produced in the reaction. That is to say, there is no guarantee that the data is exclusive. There are two possible approaches to this problem. One is to live with it and demand that theoretical calculations include contributions from other multiparticle channels. This is possible using Carrasco theory with its Monte Carlo event generation approach. The second method is to guarantee exclusivity by making a cut on missing energy. By demanding that the residual system was in a low excitation state e.g. by cutting on the p-shell region shown in figure 6.3 one guarantees the measurement was exclusive, as the existence of undetected particles would lead to a much higher observed missing energy.

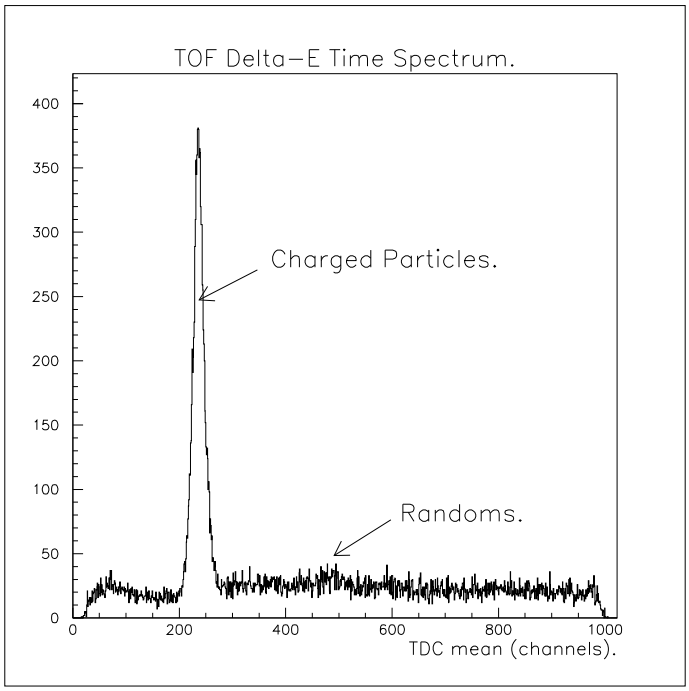

Figure 6.2: *The time spectrum of a TOF-side ΔE element*

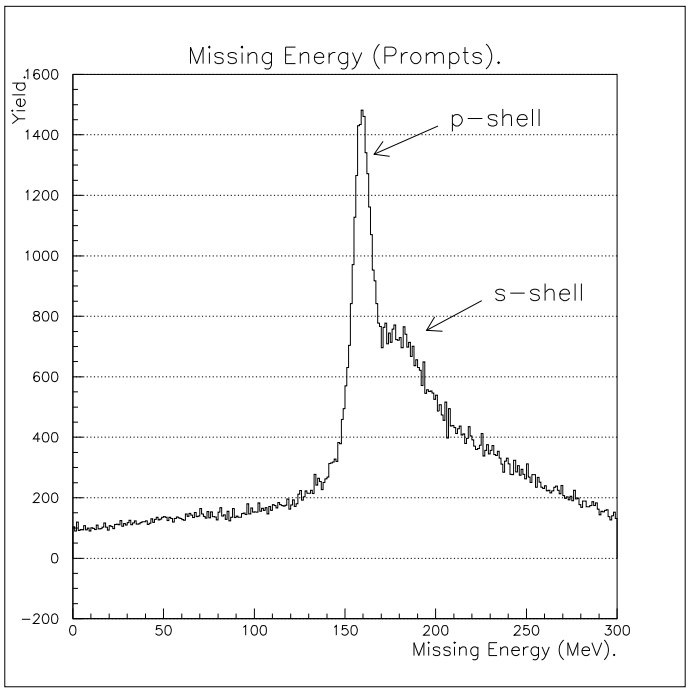

Figure 6.3: *Observed $^{12}C(\gamma, \pi^+ n)$ missing energy spectrum*

6.3 Randoms Subtraction

In each of the PiP, TOF and Tagger detection systems there is contamination by randoms. Randoms are detector hits not correlated with the reaction which generated the trigger. In the Tagger, random electrons fire focal plane detector elements. In PiP, random particles can generate afterpulses. Lastly, in TOF, randoms fire elements of the array. Even though efforts are made to select the prompt (correlated) hits, there remains a random component which must be subtracted. In order to effect this, a separate sample of random hits is required. These hits are given an appropriate (negative) weight and thus the total spectrum including events from prompt and random regions corresponds to the correlated hits alone.

6.3.1 Detector Random Samples

Random samples and the weight attached to them are derived for each detector system as follows.

Tagger

The correlated Tagger hits form a peak in the coincidence spectrum and events from this peak are labelled 'prompts' and chosen for analysis. As can be seen in figure 6.4, there is a component of random hits within this region. To subtract this component two random regions are defined in the spectrum and hits in these region are also analysed. The region from which a hit originated is recorded and a weight is ascribed to the hit according to the relative size of the regions:

$$wgt^{\gamma}_{prompt} = 1.0 \tag{6.1}$$

$$wgt^{\gamma}_{random} = \frac{-1.0 \times \Delta T_{prompt}}{\Delta T_{random_1} + \Delta T_{random_2}} \tag{6.2}$$

The negative randoms weight ensures that spectrum entries originating from randoms in the prompt region are subtracted by entries coming from randoms in the random region.

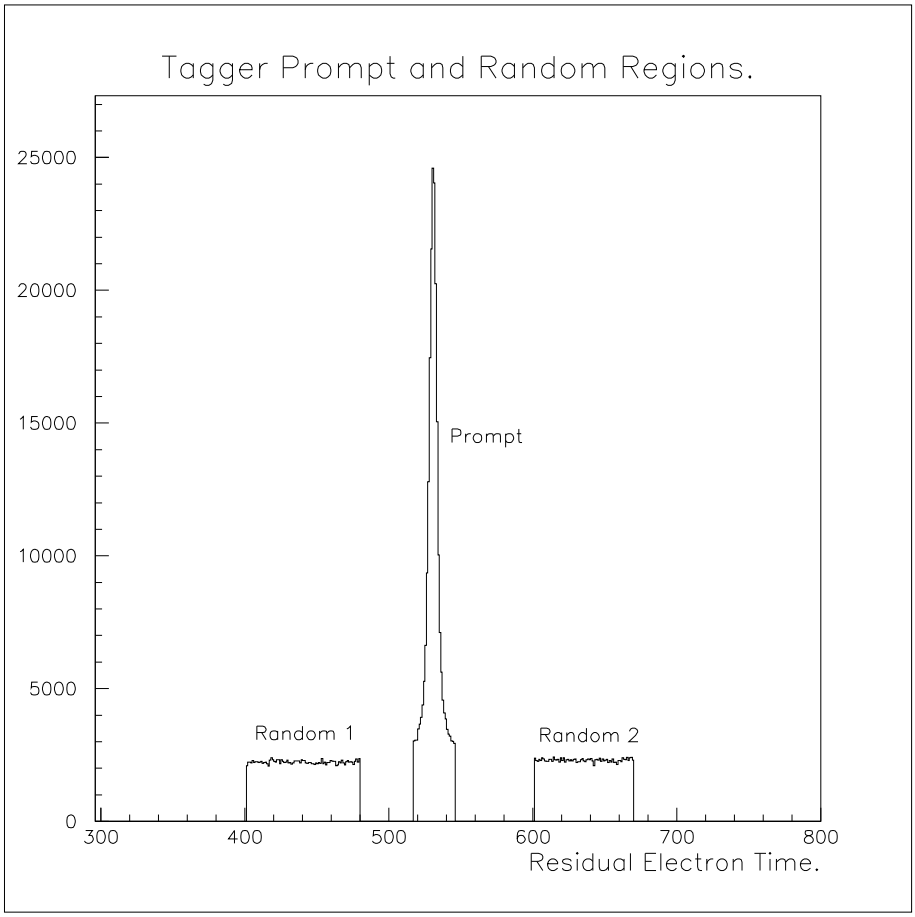

Figure 6.4: *Prompt and randoms region in the Tagger time spectrum*

PiP

Randoms in PiP are defined as afterpulses generated not by the decay of the pion but by the entrance of another uncorrelated particle into the detector. The proportion of random events can be calculated by measuring the flat background underneath the exponential decay curve of the afterpulse TDC.

Having ascertained the proportion of random events the problem of their subtraction is more complex than the Tagger case because it is impossible to obtain a purely random sample. One can however obtain a sample with a higher ratio of randoms to decay afterpulses. The method is then to split the decay spectrum into two regions, 'pseudo-prompt' and 'pseudo-random' as shown in figure 6.5. The multi-hit nature of the TDC guarantees the randoms form a flat background and the random subtraction is performed by giving the afterpulses weights in

proportion to the pseudo-prompt and pseudo-random regions:

$$wgt^{\pi}_{random} = \frac{-wgt^{\pi}_{prompt} \times (t_2 - t_1)}{(t_3 - t_2)} \tag{6.3}$$

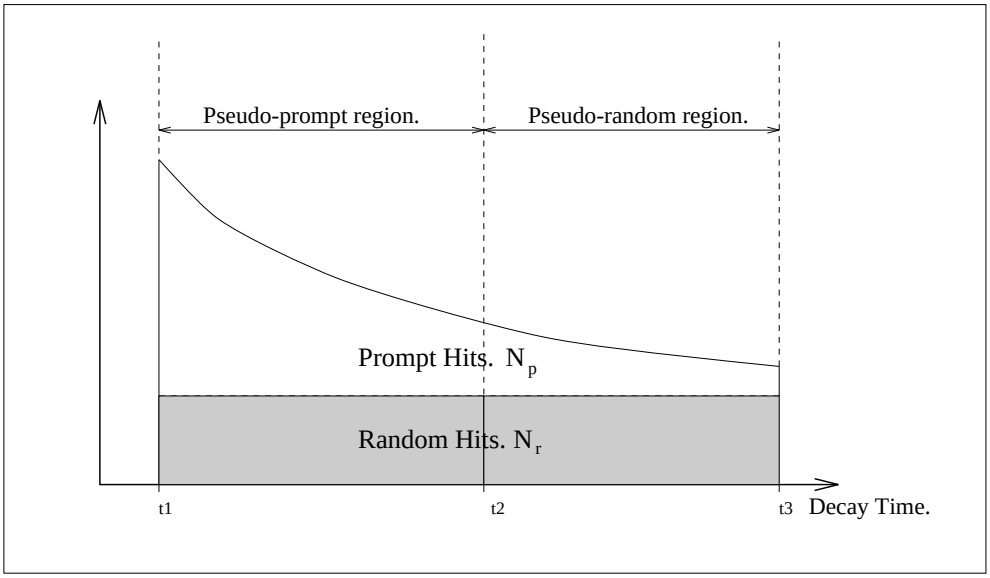

Figure 6.5: *Features of the PiP afterpulse spectrum*

Due to the fact that the pseudo-random region also contains prompts, some prompt events are subtracted from the prompt region. The prompt weight is set greater than one to compensate for this. The prompt region is from t_1 to t_2 and the random region from t_2 to t_3. The true number of prompt hits i.e. those above the flat background are defined N_p. The number of randoms in the flat piece of the spectrum is define N_r. By setting the condition that the weighted sum gives the true number of prompts N_p, the prompt weight can be derived.

$$wgt^{\pi}_{prompt} = \frac{1 - e^{-(t_3 - t_1)}}{\{(1 - e^{-(t_2 - t_1)}) - \frac{(t_2 - t_1)}{(t_3 - t_2)}(e^{-(t_2 - t_1)} - e^{-(t_3 - t_1)})\}} \tag{6.4}$$

TOF

Randoms in TOF can be seen as a flat background in the time of flight spectrum. Prompt and random regions are defined as shown in figure 6.6.

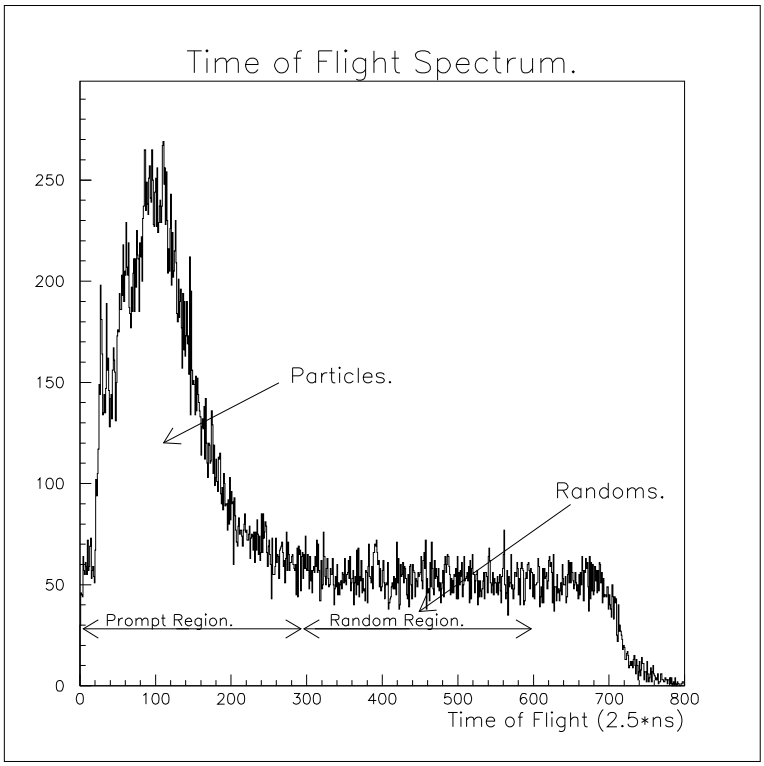

Figure 6.6: *Prompt and Random regions in TOF*

Detector hits in the random region correspond to time of flights so large they cannot be physical - a neutron with such a low energy would not exceed the software threshold imposed on the detector pulse height. Hits in this random region are flagged as such and their time of flight is shifted to bring it into the prompt region. These hits are then analysed in the same manner as those in the prompt region. Weights are associated with the hits in proportion to the time of flight windows:

$$wgt^n_{prompt} = 1.0 \tag{6.5}$$

$$wgt^n_{random} = \frac{-1.0 \times \Delta T_{prompt}}{\Delta T_{random}} \tag{6.6}$$

6.3.2 Combining Hits - Subevents

The existence of randoms gives rise to multiple hits in each detector. These hits are combined, one from each detector, in all possible combinations to form what have been termed subevents. Note that in the case of PiP, the multiplicity refers to the number of afterpulses, not the number of particles detected which is always unity. Where the number of Tagger, PiP and TOF hits is denoted N_γ, N_π and N_n respectively, the number of subevents which can be formed is simply:

$$N_{subevents} = N_\gamma . N_\pi . N_n \tag{6.7}$$

Each subevent is analysed as if it were an independent event except that when spectra are incremented the weight the event is given corresponds to the weight of the hits which constitute the subevent:

$$wgt_{subevent} = wgt^\gamma . wgt^\pi . wgt^n \tag{6.8}$$

where the detector weights are those discussed above and depend on whether the hit was in a detectors prompt or random region. If spectra are formed in this way, the final contents represent a random subtracted distribution. Figure 6.7 shows the Carbon missing energy with and without randoms subtraction.

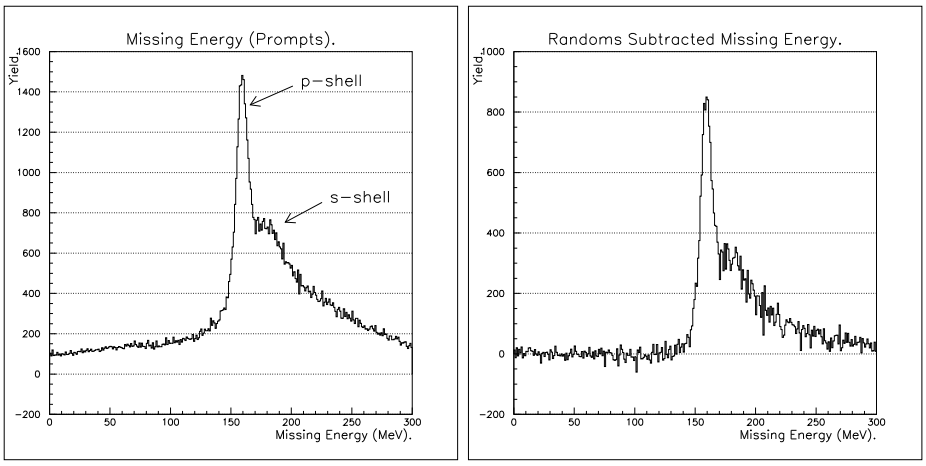

Figure 6.7: *Missing energy spectrum with and without randoms subtraction*

6.4 Detection Efficiencies

The weights facility described above in the implementation of randoms subtraction has also proved very useful in accounting for various detection efficiencies. Each detector is described in turn.

Tagging efficiency ϵ_{tagg} has been described previously in section 3.3.3. It is dependent on the photon energy. This is due to the fact that higher energy photons will form a smaller angular cone than low energy ones thus suffering less collimation. Figure 6.8 shows the obtained tagging efficiency as a function of Focal Plane Detector element.

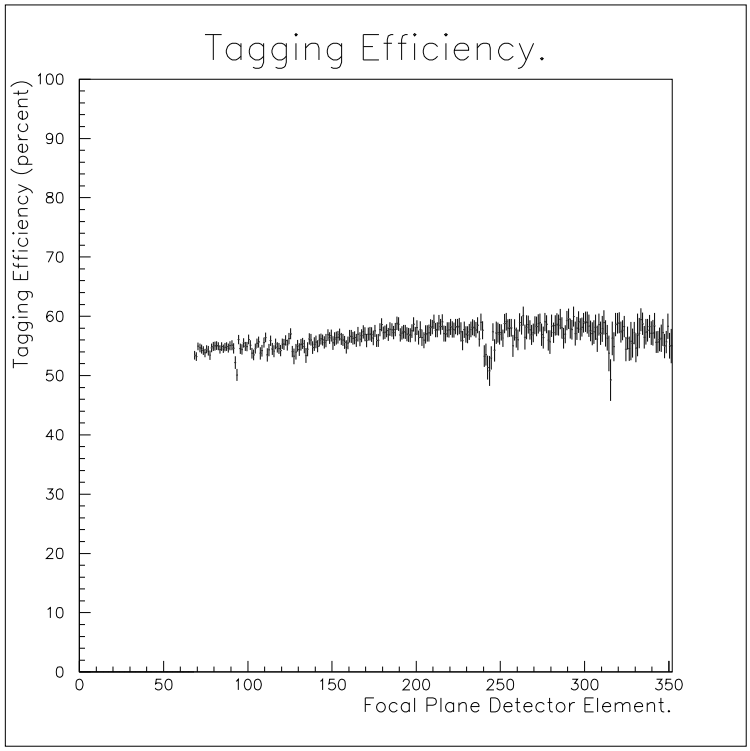

Figure 6.8: *Tagging Efficiency along the Focal Plane*

In the calculation of cross sections, the photon flux is derived from the number of electrons detected at a FPD element. This would be sufficient if all the associated photons were incident on target, however this is only true for the proportion ϵ_{tagg}.

Pion Detection efficiency, ϵ_{π} was described in Chapter 5. Due to the inelastic

processes undergone by the pion in the scintillator and the algorithm rejecting such events, ϵ_π is a function of pion energy. The pion detection efficiency, which is a product of the probability of generating an afterpulse and the probability that, given an afterpulse, the event does not inelastically scatter, is shown in figure 6.9.

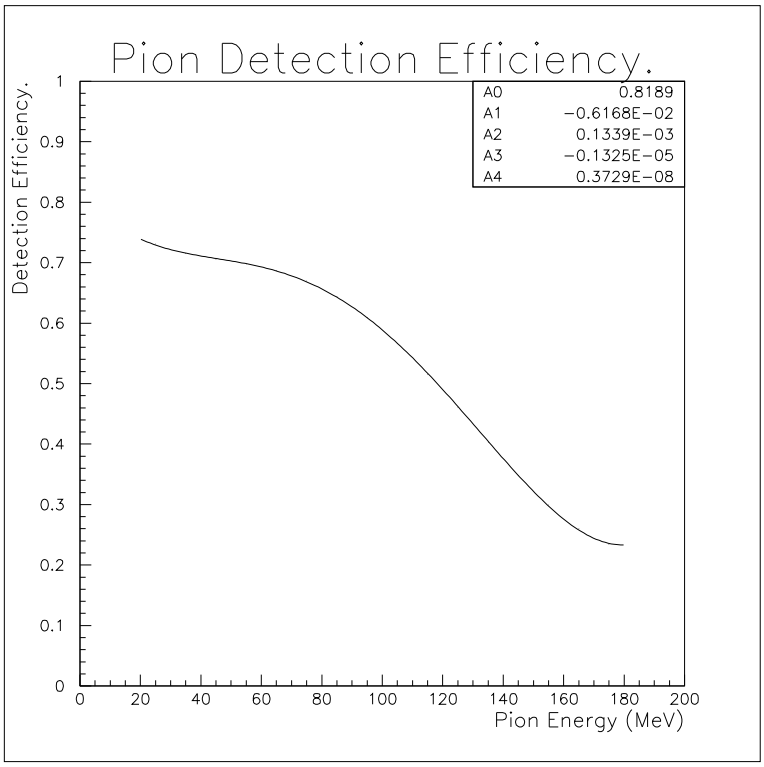

Figure 6.9: *Pion Detection Efficiency*

Neutron detection efficiency, ϵ_n, is also energy dependent due to the fact that ionisation loss is not caused by the neutrons themselves but mainly by knock on protons in the scintillator. The probability of the neutron interacting with the scintillator is energy dependent. In order to calculate the efficiency the Monte Carlo code STANTON [Cec79] was used. The results for a $5\,\mathrm{MeV}_{ee}$ TOF bar threshold are shown in figure 6.10. Where a TOF stand has more than one layer, the neutron can pass through more than one bar. If the efficiency for a single bar is ϵ_n^{bar} then the total efficiency for a stand of N layers, $\epsilon_n(N)$, can be derived from the recurrence relation:

$$\epsilon_n(N) \quad = \quad \epsilon_n(N-1) + \epsilon_n^{bar}(1. - \epsilon_n(N-1)) \tag{6.9}$$

$$\epsilon_n(0) \quad = \quad 0.0 \tag{6.10}$$

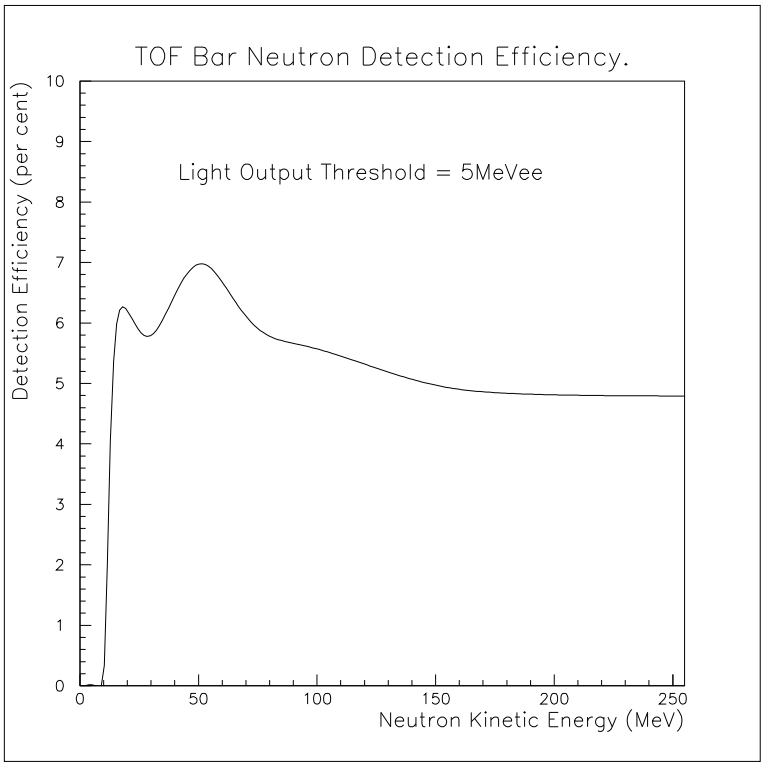

Figure 6.10: *Neutron Detection Efficiency for a TOF bar*

The efficiency also depends on the effective thickness a bar presents to the particle which is angle dependent. There was very little variation in effective thicknesses and it was assumed that ϵ_n^{bar} depended linearly upon it.

All the above detection efficiencies are taken into account when calculating the weight of a subevent which is now redefined:

$$wgt_{subevent} = \frac{wgt^{\gamma}.wgt^{\pi}.wgt^{n}}{\epsilon_{tagg}(E_{\gamma}).\epsilon_{\pi}(E_{\pi}).\epsilon_n(E_n,\theta_n,\phi_n)} \tag{6.11}$$

6.5 Background Subtraction

There remains one further subtraction which cannot be implemented using the weighted subevent method discussed. This is the subtraction of background events stemming from photoreactions with the air surrounding the target. In order to perform this subtraction data was collected with the target removed. This data is analysed in the same manner as the target-in data and the subtraction performed spectrum by spectrum. Both spectra must be suitably normalised by dividing out the number of incident photons - this is the case for the cross section spectra which are presented in this thesis.

One of the important decisions facing the experimentalist is what fraction of the beam time should be allocated to target-out data collection. The objective is to minimise the relative error in the result i.e. the subtracted spectrum content. If the ratio of the background (target-out) to foreground (target-in) event rate, R_{bf}, is known then the optimum fraction of the beam time devoted to target-out runs, F_{out}, can be derived as follows. Setting the total beam time, T, and the foreground rate, $Rate_f$, to be unity then the number of foreground and background events collected (denoted N_f and N_b) is simply:

$$N_f = (1 - F_{out}).T.Rate_f \tag{6.12}$$

$$= (1 - F_{out}) \qquad (Rate_f = 1\ ,\ T = 1) \tag{6.13}$$

$$N_b = F_{out}.T.R_{bf}.Rate_f \tag{6.14}$$

$$= F_{out}.R_{bf} \tag{6.15}$$

Assuming that the photon flux is constant then the subtraction is performed simply by weighting the background counts with the the ratio of target-in to target-out collection times:

$$N_{sub} = N_f - \frac{(1 - F_{out})}{F_{out}}.N_b \tag{6.16}$$

The error in this quantity is derived simply as:

$$\sigma_{N_f} = \sqrt{N_f} \tag{6.17}$$

$$\sigma_{N_b} = \sqrt{N_b} \tag{6.18}$$

$$\sigma_{N_{sub}} = \sqrt{\sigma^2_{N_f} + \frac{(1-F_{out})^2}{F^2_{out}}.\sigma^2_{N_b}} \tag{6.19}$$

$$= \sqrt{N_f + \frac{(1-F_{out})^2}{F^2_{out}}.N_b} \tag{6.20}$$

The relative error is simply the absolute error divided by the number of counts, N_{sub}. The optimum fraction of target-out time is found by differentiating the relative error w.r.t F_{out} and solving for the case where the derivative is zero (the minimum). The resultant expression is:

$$F_{out} = \frac{\sqrt{R_{bf}}}{\sqrt{R_{bf}}+1} \tag{6.21}$$

The result is shown in figure 6.11. In the experiment, it was estimated that the ratio of background to foreground rates was 0.05 thus the fraction of time spent with the target out was 0.18.

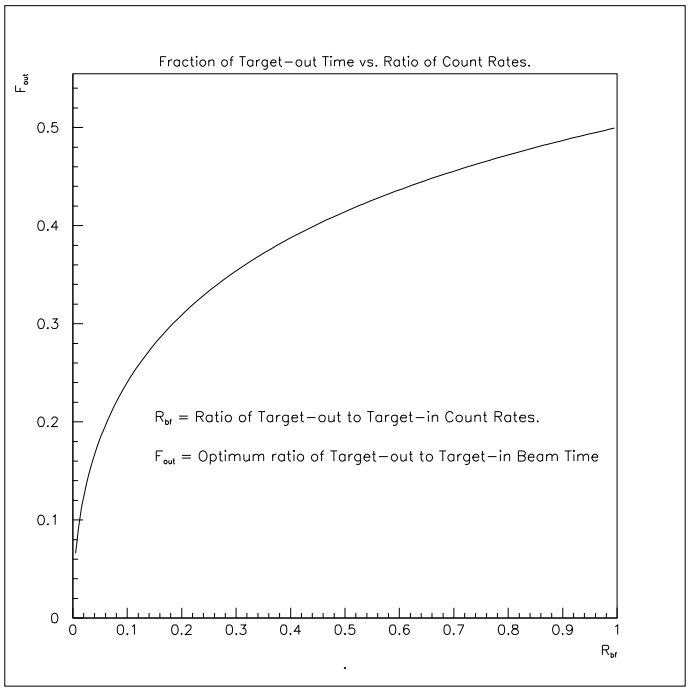

Figure 6.11: *Evaluation of optimum target-out beam time*

6.6 Derivation of Cross Sections

The basic probability of a nuclear reaction is measured by finding the yield of reaction products under well defined geometrical conditions for a known incident flux of particles. The probability is expressed as a cross section, σ. It is related to the yield, $\mathcal{Y}$, i.e. the number of reactions which take place, by the relation,

$$\mathcal{Y} = N_\gamma . n_{target} . \sigma \tag{6.22}$$

where N_γ is the number of incident photons and n_{target} is the number of target nuclei per unit area which can expressed as,

$$n_{target} = N_A . \rho_s / A \tag{6.23}$$

where N_A is Avogadro's number (6.02×10^{23}) and A is the atomic weight of the nucleus. The quantity ρ_s is the target mass per unit area, the element of area being defined normal to the incident beam. This is simply the product of the target density, ρ, and its effective thickness, t_{eff},

$$\rho_s = \rho . t_{eff} \tag{6.24}$$

$$= \rho . \frac{t}{sin\theta_{target}} \tag{6.25}$$

where t is the target thickness and θ_{target} is the angle between the beam axis and the target plane.

A cross section has the dimensions of an area and can be thought of as that area through which an incident particle must pass if it is to cause the specified reaction in the target nucleus. The most commonly used unit is the barn where 1b $= 10^{-28}\mathrm{m}^2$. Naturally, a reaction cross section is dependent on the energy of the incident particle and it may, for example, show resonance behaviour as is the case in pion photoproduction. The measurement of a specific reaction cross section is actually rather difficult as it requires a detector with an acceptance sufficient to cover all possible angles and energies of the reaction products. It is far more common, therefore, to measure differential cross sections where the reaction products are limited to some specified region of phase space. Taking for example the $\mathrm{p}(\gamma, \pi^+)\mathrm{n}$ reaction at a given incident photon energy, the kinematical quantities

involved are the kinetic energies and spherical polar angles of the produced pion and neutron,

$$T_\pi, \theta_\pi, \phi_\pi, T_n, \theta_n, \phi_n$$

The differential cross section at specific pion polar and azimuthal angle, (θ_π, ϕ_π), is found by measuring the reaction yield, $d\mathcal{Y}$, for pions in the element of solid angle $d\Omega_\pi$,

$$\frac{d\sigma}{d\Omega_\pi} = \frac{N_\gamma . n_{target} . d\mathcal{Y}}{d\Omega_\pi} \tag{6.26}$$

in units barns/steradian (b/sr). The element of solid angle $d\Omega$, in steradians, is defined in terms of the elements of polar and azimuthal angles, in radians, as,

$$d\Omega = sin\theta d\theta d\phi \tag{6.27}$$

In the case of the $p(\gamma, \pi^+)n$ reaction, the two-body final state dictates that once the pion angles have been specified the other quantities are determined i.e. an element of pion solid angle $d\Omega_\pi$ corresponds to an element of phase space in the final state system. In the case of nuclear pion photoproduction, such as the $^{12}C(\gamma, \pi^+n)$ reaction studied here, the above kinematical restraints no longer apply due to the presence of a third particle, the residual nucleus, in the final state. An element of phase space is now defined by specifying five of the six kinematical quantities and if one chooses the set $\{T_\pi, \theta_\pi, \phi_\pi, \theta_n, \phi_n\}$ then the differential cross section is denoted,

$$\frac{d^3\sigma}{dT_\pi d\Omega_\pi d\Omega_n}$$

in units b/MeV.sr^2. This triple differential cross section is a function of five variables, although due to the system's azimuthal symmetry it depends only on the difference of pion and nucleon azimuthal angles, not on each independently. To represent the quantity, it is necessary to fix four variables and plot it as a function of the remaining one. This for example can be seen in the Tomsk data of figure 1.4 where pion and proton angles were fixed and the differential cross section plotted versus proton energy. To do this requires a lot of statistics as one is limited to such a small region of phase space that only a small fraction of events will fall in each bin. For this reason, it is common to integrate over one or more of the variables. For example, if one integrates over the pion energy one obtains

the double differential cross section,

$$\frac{d^2\sigma}{d\Omega_\pi d\Omega_n} = \int \frac{d^3\sigma}{dT_\pi d\Omega_\pi d\Omega_n} dT_\pi \tag{6.28}$$

Due to detector thresholds it is only possible to integrate over some range of energies and it is important to state these integration limits if comparison of theory and experiment is to be made possible.

The data obtained in this experiment will be presented mainly as integrated double differential cross sections. The integration limits, T_π^{min}=20 and T_π^{max}=180 MeV, are wide enough to cover almost all the produced pions. Some triple differential cross sections will be presented, though with inferior statistical error bars. Data was taken on the Carbon target for a total of 45 hours. The photon flux was approximately 10^6/s for each tagger element (i.e. 2 MeV photon energy bin). The yield was extracted from the data using weights to perform randoms subtraction and to compensate for the various detection efficiencies,

$$\mathcal{Y} = \sum_{events} \sum_{subevents} wgt \tag{6.29}$$

$$wgt = \frac{wgt_\gamma . wgt_\pi . wgt_n}{\epsilon_\pi . \epsilon_n} \tag{6.30}$$

The number of incident photons, N_γ, was obtained from the tagger scalers combined with the tagging efficiency.

$$N_\gamma = N_{e'} . \epsilon_{tagg} \tag{6.31}$$

The scalers were gated such that they did not count while the system was dead. This means that no explicit dead time correction need be made to the data. Cross sections were derived for both Carbon and Hydrogen. The quantity n_{target} was obtained for each target as detailed in table 6.1

Target	Mass (g)	Area (cm^2)	ρ_s	Atomic Wgt	$\sin\theta_t$	n_{target}
CH_2	-	-	0.915	14.01	0.342	$2\times1.150\times10^{23}$ (H)
C	26.86	2.00	0.839	12.01	0.342	1.23×10^{23}

Table 6.1: *Target Details*

6.6.1 Hydrogen Cross Sections

In order to test the system, data from the CH_2 target was used to obtain differential cross sections for the free pion production process p(γ, π^+)n. The differential cross section was obtained for four photon energy regions, each 50 MeV wide, between 225 and 425 MeV. It was plotted as a function of pion polar angle in the centre of mass system θ^*_π,

$$\frac{d\sigma}{d\Omega^*_\pi} = \frac{\Delta\mathcal{Y}}{N_\gamma . n^H_{target} . \Delta\Omega^*_\pi} \tag{6.32}$$

This represents the differential cross section averaged over the solid angle bin $\Delta\Omega^*_\pi$. The solid angle bins were defined by using 5° CMS pion polar angle bins and one 30° azimuthal angle bin. There is only need for one azimuthal angle bin as the differential cross section is constant w.r.t. ϕ_π as demanded by symmetry. Only data points where the corresponding neutron angle lies within the TOF detector array were used i.e. only those points where there is 100% geometrical efficiency. The reactions on Hydrogen were separated from the Carbon events by requiring that particle energies and angles were consistent with two body kinematics. A cut was also made on the missing energy peak. The data were compared with predictions of the B-L free pion photoproduction operator [Blo77] which have compared well with previous data [Bet68]. The B-L predictions were also averaged over the large photon energy bins. The comparison of data and theory is shown in figures 6.12 and 6.13. An overall normalisation factor of 1.25 was applied to all spectra to improve agreement. This corresponds to a loss of 20% of the events, which could be reasonably be expected from effects such as unaccounted dead time, rejection of events due to randoms contamination and pion decay before entering the PiP detector. The latter effect is estimated to be a 10% effect at

T_π=20 MeV falling to 5% at pion energies above 100 MeV. As can be seen from the graphs, the agreement is generally quite good. The few data points that are in particular disagreement may be due to the fact that the pion detection efficiency is modelled by a smooth curve but may show more intricate structure. In the case of the integrated double differential cross sections to be presented in the next chapter, the pion energy is integrated over and sensitivity to the finer details of the pion detection efficiency should be greatly reduced.

The Hydrogen results give credibility to the detection technique and should promote confidence in the Carbon results which were obtained in an identical experimental setup. The main uncertainty lies in whether to apply the same normalisation constant to the Carbon results and this issue is discussed more fully in section 6.6.3.

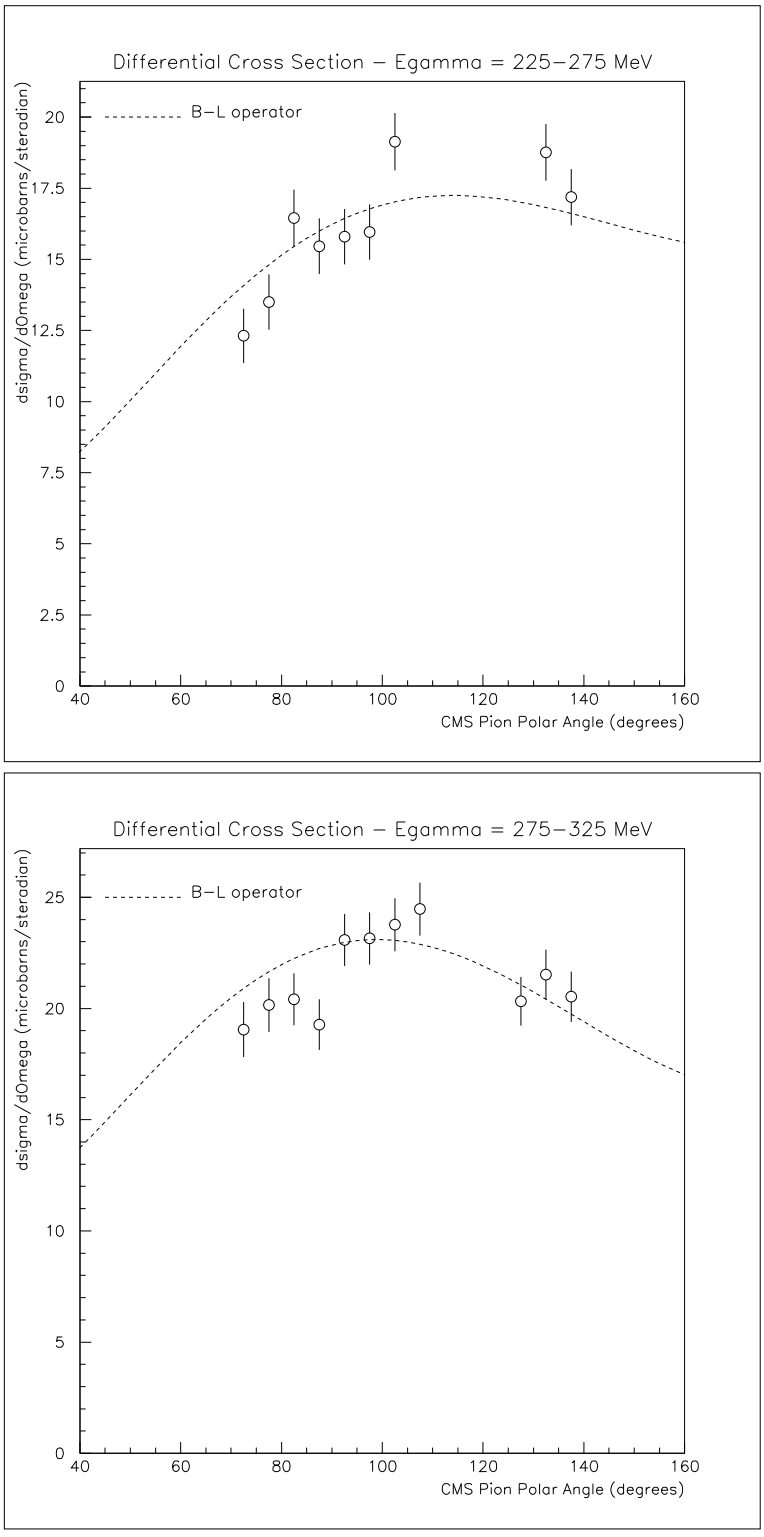

Figure 6.12: *Comparison of Hydrogen cross sections with theory*

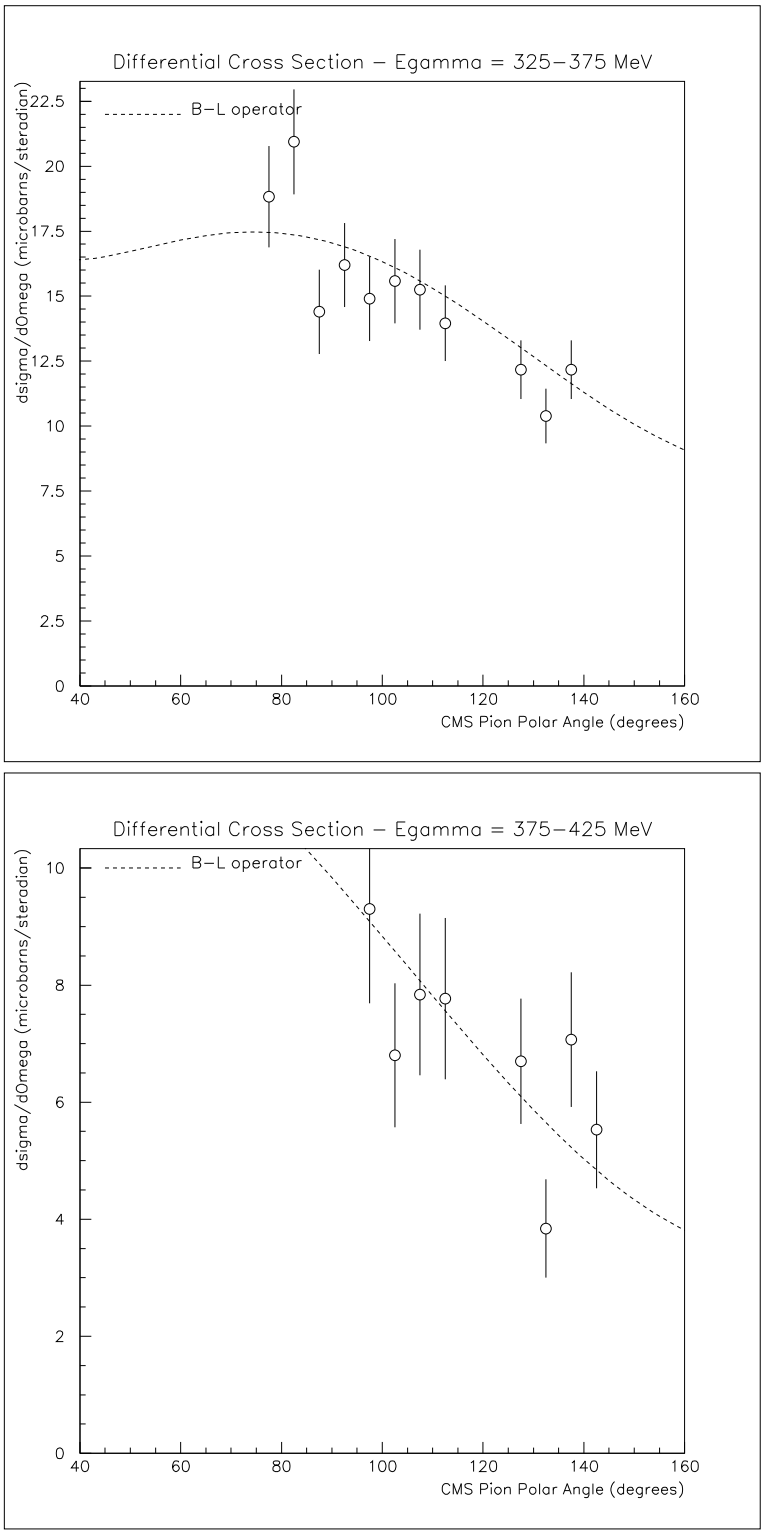

Figure 6.13: *Comparison of Hydrogen cross sections with theory*

6.6.2 Carbon Cross Sections

The differential cross section for a given photon energy is defined as,

$$\frac{d^3\sigma}{dT_\pi d\Omega_\pi d\Omega_n} = \frac{\Delta\mathcal{Y}}{N_\gamma . n_{target} . \Delta T_\pi . \Delta\Omega_\pi \Delta\Omega_n} \tag{6.33}$$

This represents the average differential cross section over the given energy and angular bins. The cross section was obtained for four photon energy regions, each 40 MeV wide, between 240 and 400 MeV. The binning recipe used is shown in table 6.2.

Quantity	Range	Bin Size	No. of Bins
T_π	20-180 MeV	10 MeV	16
θ_π	60-120°	15°	4
ϕ_π	(-15)-15°	30°	1
θ_n	10-150°	5°	28
$\phi_n - \phi_\pi$	170-190°	20°	1

Table 6.2: The binning recipe employed in extracting Carbon cross sections

The last condition exploits the azimuthal symmetry of the system. It demands that the neutron is emitted approximately in the reaction plane defined by the pion. It amounts to a 20° neutron azimuthal angle bin if one imagines that at each event the system is rotated around the beam axis such that the pion is at $\phi = 0°$. The integrated double differential cross sections were obtained simply by summing over all pion energy bins. The target-out background was found to display similar behaviour to the target-in data. The missing energy spectrum suggests that Nitrogen and Oxygen were the main contributions. Figure 6.14 shows the target-out missing energy spectrum and figure 6.15 show a typical cross section measurement for both the target-in and target-out data set. The target-out contribution is only 2% of the target-in and was therefore neglected as it is well below the systematic errors in the measurement.

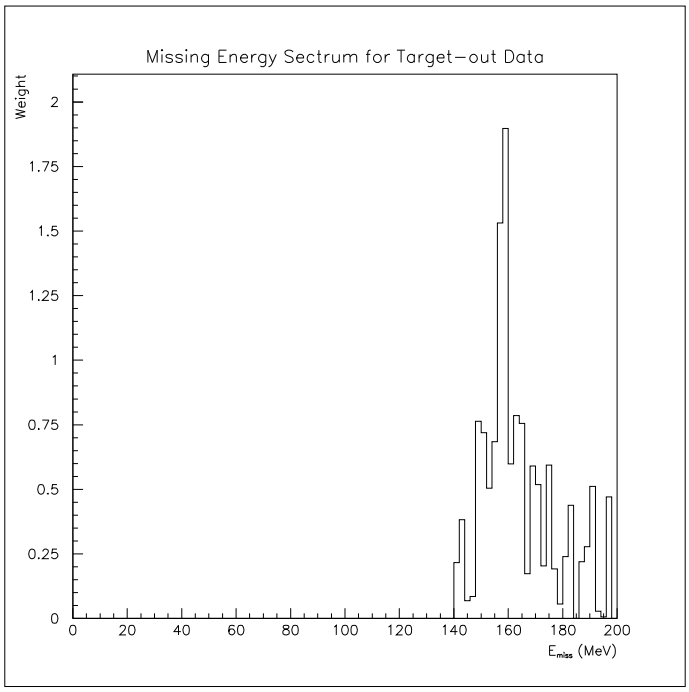

Figure 6.14: *Missing Energy Spectrum for Target-Out Data*

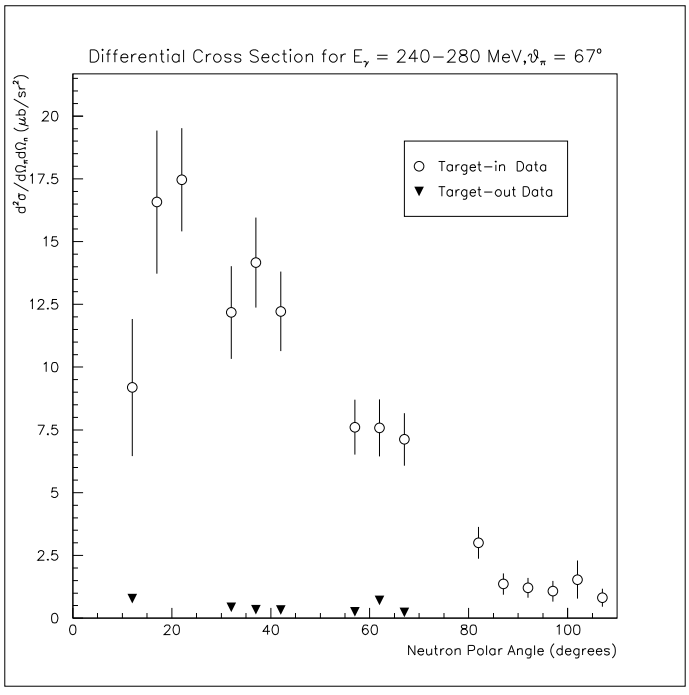

Figure 6.15: *Cross section contributions of target out and in data*

6.6.3 Evaluation of Uncertainties

Experimental data is meaningless without error bars and this section is devoted to a discussion of the various factors which contribute to the uncertainty in the results. There are two types of error, statistical and systematic, and they have very different natures.

Statistical Errors

Statistical errors simply reflect the fact that the experiment measures probabilities and in the same way that it would require many throws of a die to precisely test the probability of a particular outcome, the experimentalist needs to detect many events to precisely measure a reaction cross section. In the simplest case of a spectrum bin containing N counts, the associated statistical error is simply $\sqrt{N}$. In the current experiment, the situation is complicated by the need to perform randoms subtraction and also to compensate for detection efficiencies. This is done by assigning a weight to each event. In this case, the contents of a spectrum bin, W, and the associated statistical error, σ_W, are given by the relation [McG94]:

$$W = \sum wgt \tag{6.34}$$

$$\sigma_W = \sqrt{\sum (wgt)^2} \tag{6.35}$$

This reduces, in the case where all the weights are unity, to the simple $\sqrt{N}$ rule described above. Statistical errors can be reduced either by collecting more data or by using larger bin sizes. In fact, the bin sizes are often determined by the desire to obtain a certain level of statistical uncertainty. The data presented in the current experiment was binned in order to achieve statistical errors below 15%.

Systematic Errors

Systematic uncertainties are more difficult to calculate than statistical ones. They stem from uncertainties in the calibration procedure and there is no simple formula to evaluate them as is the case for statistical uncertainties. In the current experiment, much of the systematic uncertainty is removed by comparison to the

known cross section for the p(γ, π^+n) reaction. The sources of systematic error and their estimated sizes are listed below.

1) **Tagging Efficiency:** Tagging efficiency was measured at various times during the experimental period and found to be stable. Although the tagging efficiency for a given tagger element was obtained with a statistical uncertainty of 2-3%, by fitting the results over the whole focal plane to a smooth function, the uncertainty was reduced to the 1% level.

2) **Pion Detection Efficiency:** Calibration data was used to obtain the detection efficiency which was fitted to a smooth function of pion energy. The limited amount of data available for this procedure led to an estimated 5% uncertainty in the result obtained.

3) **Neutron Detection Efficiency:** The authors of the code STANTON [Cec79], which was used to evaluate the efficiency, quote an uncertainty of 5% in their result.

4) **Target Density:** The target was precisely weighed and measured hence the error in the density should be negligible, certainly below 1%.

5) **Randoms Contamination:** The presence of a random particle may cause a genuine event to be rejected. For example, a random in the TOF-side ΔE can mean that the event fails to satisfy the 'neutral particle in TOF' condition. Such effects have been estimated to have a 5% effect.

6) **Solid Angle:** In calculating differential cross sections, cuts in polar and azimuthal angles are made to define elements of solid angle. Uncertainties in the position calibrations lead to uncertainties in the size of the solid angle element. This uncertainty is estimated to be about 6%.

7) **Pion Decay in Flight:** the decay of pions before arrival in PiP will corrupt the angular information. The effect can be reduced by demanding consistency between the start detector and PiP positions. This leads to an maximum loss of events of 10% at 20 MeV falling to 5% above 100 MeV.

Although the normal procedure would be to combine the above factors to achieve an overall systematic uncertainty, the use of the Hydrogen calibration reaction allows much of the uncertainty to be removed by application of a normalisation factor to achieve agreement between current and previously established data. A normalisation factor of 1.25 was applied to the Hydrogen data. This gave reasonable agreement with the Blomqvist-Laget model [Blo77]. Blomqvist and Laget claim that their model fits the previous data with 'a great degree of accuracy'. The data of Betourne *et al.* [Bet68], which agrees with the B-L model and the current normalised data, was quoted with systematic errors of 4%. The normalisation was performed on a limited amount of calibration data and the statistical error in the normalisation factor was found to be 10%. The overall uncertainty in the normalisation is therefore 12%, where the above two values are added in quadrature.

The only remaining uncertainty is whether the same normalisation applies to the Carbon measurement as was used for the Hydrogen data. Of the systematic errors listed above, items 1) to 5) apply equally to the Carbon and Hydrogen measurements. In the case of the Carbon measurement, there exists the additional uncertainty in the element of neutron solid angle as the data are presented as double differential cross sections. This depends on the uncertainty in the TOF azimuthal angle calibration, which is estimated to be about 5%. There is also an uncertainty in the effect of pion decay in flight. In the Hydrogen data, some of these events may be rejected if they fail to meet the constraints of two-body kinematics. In the Carbon data, however, such constraints are not present and some of these events will be accepted. The associated uncertainty is estimated to be approximatedly 7%. These two effects lead to an uncertainty of 9% in the relative normalisations of the Carbon and Hydrogen data sets. Combined with the error in the normalisation factor itself, the total systematic error for the Carbon data is found to be 15%.

Chapter 7

Results and Discussion

In this chapter, the experimental results are presented and compared with theoretical predictions. The form chosen to express the results depended partly on experimental considerations viz. thresholds, geometry and the level of statistics and partly on the nature of the theoretical predictions. Two theoretical models were considered, a factorised DWIA approach embodied in the code THREEDEE [Cha77] and a full microscopic approach as calculated by the code of Carrasco and Oset [Car94]. The comparison of the data with each model is treated separately in the sections below.

7.1 Comparison of Data with DWIA Predictions

As discussed in Chapter Two the Distorted Wave Impulse Approximation (DWIA), as applied to nuclear pion photoproduction, involves three main model ingredients; an elementary production operator, a bound state wave function and optical model potentials to describe the final state interactions of the produced particles. The expression for the cross section is given in equations 2.46 and 2.47. In the code THREEDEE, which was modified by G. van der Steenhoven in order to describe the $^{16}O(\gamma, \pi^- p)$ reaction [Pha91], the Blomqvist-Laget production operator [Blo77] was chosen to describe the free pion photoproduction process. The bound state wave function is generated from a mean field potential represented by a (real) Woods-Saxon form. The potential is varied to reproduce the observed

binding energy of the struck nucleon. The optical potentials incorporated in the THREEDEE code are fairly old parameterisations. Ideally, one would like to use the DWIA formalism of Li, Wright and Benhold [Li93] who use the pion-nucleus optical potential of Carr *et al.* [Car82] and the nucleon-nucleus potential of Scwhandt *et al.* [Sch82]. Hopefully, this comparison will be made once the data is published. A comparison with THREEDEE is, however, useful as long as the limitations of the optical potentials are borne in mind. In the code, the distorted pion wave was generated using the Cottingame-Holtkamp pion-nucleus optical potential [Cot80]. The potential was extracted from pion scattering data for a variety of nuclei, including Carbon-12, for incident pion energies above 100 MeV. For the sake of comparison, two nucleon-nucleus optical potentials were employed, the Jackson-Abdul potential [Abd79] and that of Nadasen *et al.* [Nad81]. The Jackson-Abdul potential was extracted from p-^{12}C scattering at incident proton energies between 50 and 150 MeV. The Nadasen potential, which has faired preferably in more recent literature [Ste95], is a global parameterisation based mainly upon proton scattering from Calcium, Zirconium and Lead at incident energies between 80 and 180 MeV. In order to look at p-shell production, a $1p_{3/2}$ bound state wave function is used with a spectroscopic factor of 2.6, as extracted from $(e, e'\mathrm{p})$ scattering data [Li93]. The code was used to extract predictions of the triple differential cross section which were then integrated over the experimental pion energy and neutron out-of-plane angle limits to enable comparison with experiment. The integrated double differential cross sections were therefore,

$$\frac{d^2\sigma}{d\Omega_\pi d\Omega_n}(\theta_\pi, \theta_n) = \int_{T_\pi=20}^{T_\pi=180} \frac{d^3\sigma}{dT_\pi d\Omega_\pi d\Omega_n} dT_\pi \tag{7.1}$$

The cross sections are averaged over the 20 degree ϕ_{diff} bin. The cross sections are presented for four energy regions, each 40 MeV wide, between 240 and 400 MeV. At each energy, they are plotted as a function of neutron polar angle for four pion angles corresponding to θ_π at 67, 82, 97 and 112° ±7.5°. The double differential cross section results and integrated DWIA predictions are shown in figures 7.1 to 7.8. The error bars reflect the statistical uncertainty of a data point. The systematic uncertainty was discussed earlier, in section 6.6.3, and found to be approximately 15%. Only those data points where the TOF detector gave 100%

geometrical detection efficiency are shown i.e. the missing points correspond to gaps between stands of the TOF array. Triple differential cross sections are shown in figures 7.9 to 7.11. They are presented for each of the four photon energy regions. Two pion angles were selected, 67 and 112°, with the neutron angle chosen such that it be conjugate to the pion, viz. 40 and 20°, in order to maximise statistics. At the higher energies the statistical errors are large but at lower energies the quality of the data is good.

DISCUSSION

The first impression gained from studying the double differential cross sections presented is that the DWIA predictions do very well at reproducing the form of the data. The Abdul-Jackson potential does particularly well while the predictions based on the Nadasen potential fall below the data, particularly at low photon energies. It would be dangerous, however, to draw strong conclusions from this as the predictions depend equally on the pion optical potential and the agreement found using the Jackson potential could be due to the cancellation of errors in both. More importantly, the validity of the comparison at the lowest photon energy must be questioned due to the bulk of the neutrons being at energies lower than that for which the potentials were designed. At higher photon energies, this objection is no longer valid and in fact the Jackson and Nadasen predictions tend to converge. Setting the debate on the magnitude of the cross section aside, there can be no doubt that the shape is well reproduced. Figure 7.2 shows this particularly well. This gives weight to the conclusion that the data really do constitute quasi-free pion production and that the Impulse Approximation is appropriate in this domain.

The presentation of triple differential cross sections certainly provides much more information but unfortunately the quality of data is inferior. To make matters worse, the region where the data does have good statistics, i.e. the lowest photon energies, is exactly the region where the theory is suspect because the optical potentials are being applied at energies below that for which they were designed. This deficiency in the theory will hopefully be rectified by the application of more recent optical potentials as discussed above. One can at least say that

the data presented at and above 300 MeV photon energies is not inconsistent with the theory and good agreement can be seen at 300 MeV. At 340 and 380 MeV, the forward angle data is of better quality and it seems that the predictions fall below the data at higher pion energies.

One of the main points of interest to come out of the data is that it provides no support for previous claims that there is a dramatic reduction in the cross section at forward pion angles. The experiment of L.D. Pham *et al.* [Pha91], which was described in chapter 1, studied the ^{16}O$(\gamma, \pi^-$p) reaction at a photon energy of 360 MeV. They found that the integrated cross section at pion angle $\theta_\pi = 64^\circ$ and proton angle $\theta_p = 40^\circ$ was a factor three lower than the predictions of THREEDEE. In this experiment, the data actually seems to exceed the predictions as can be seen in the upper plot of figure 7.5. This is not a direct comparison as the present experiment is studying the ^{12}C$(\gamma, \pi^+$n) reaction. However, the two reactions are expected to show similar trends.

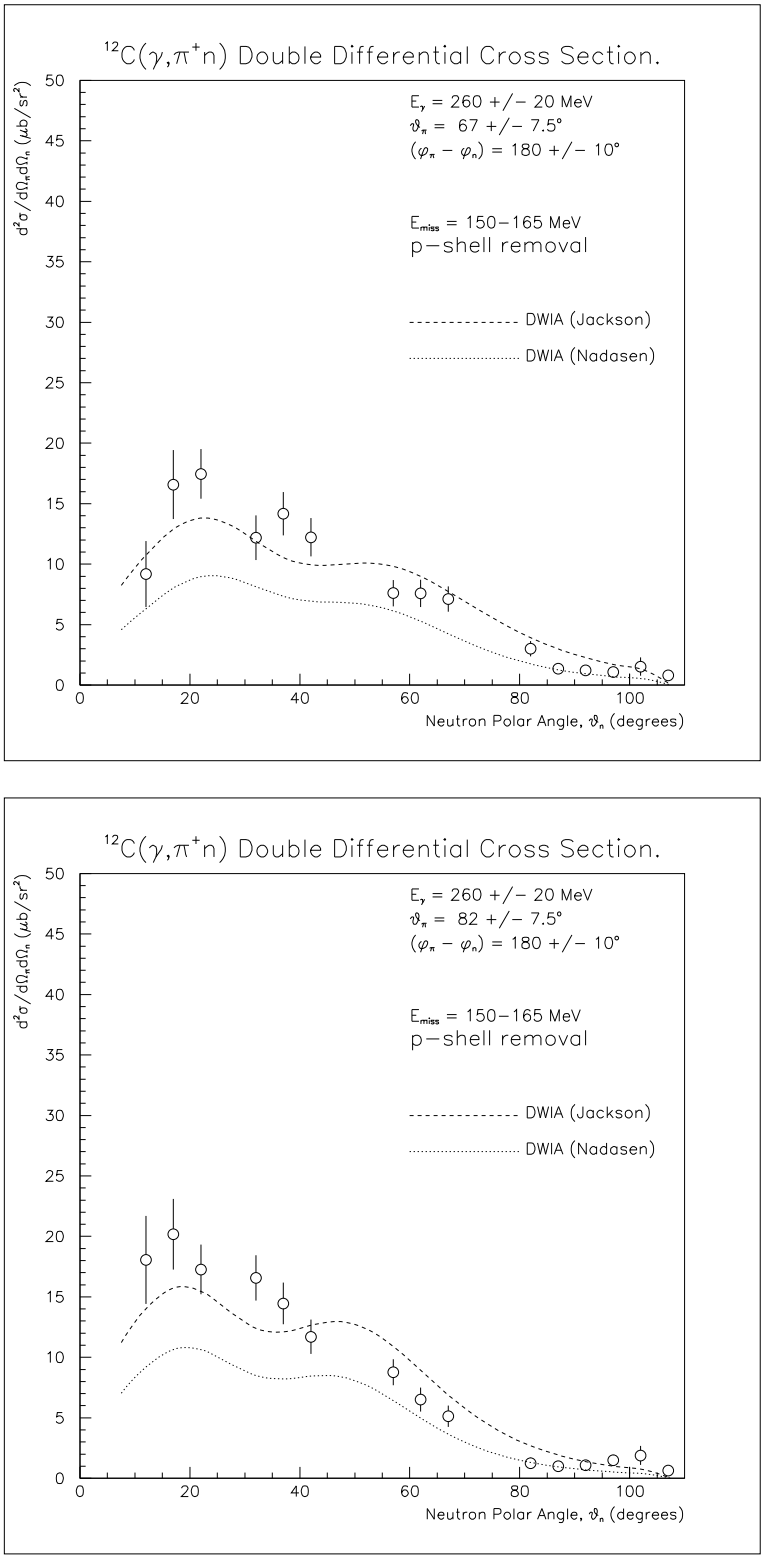

Figure 7.1: *Double Differential Cross Section Data*

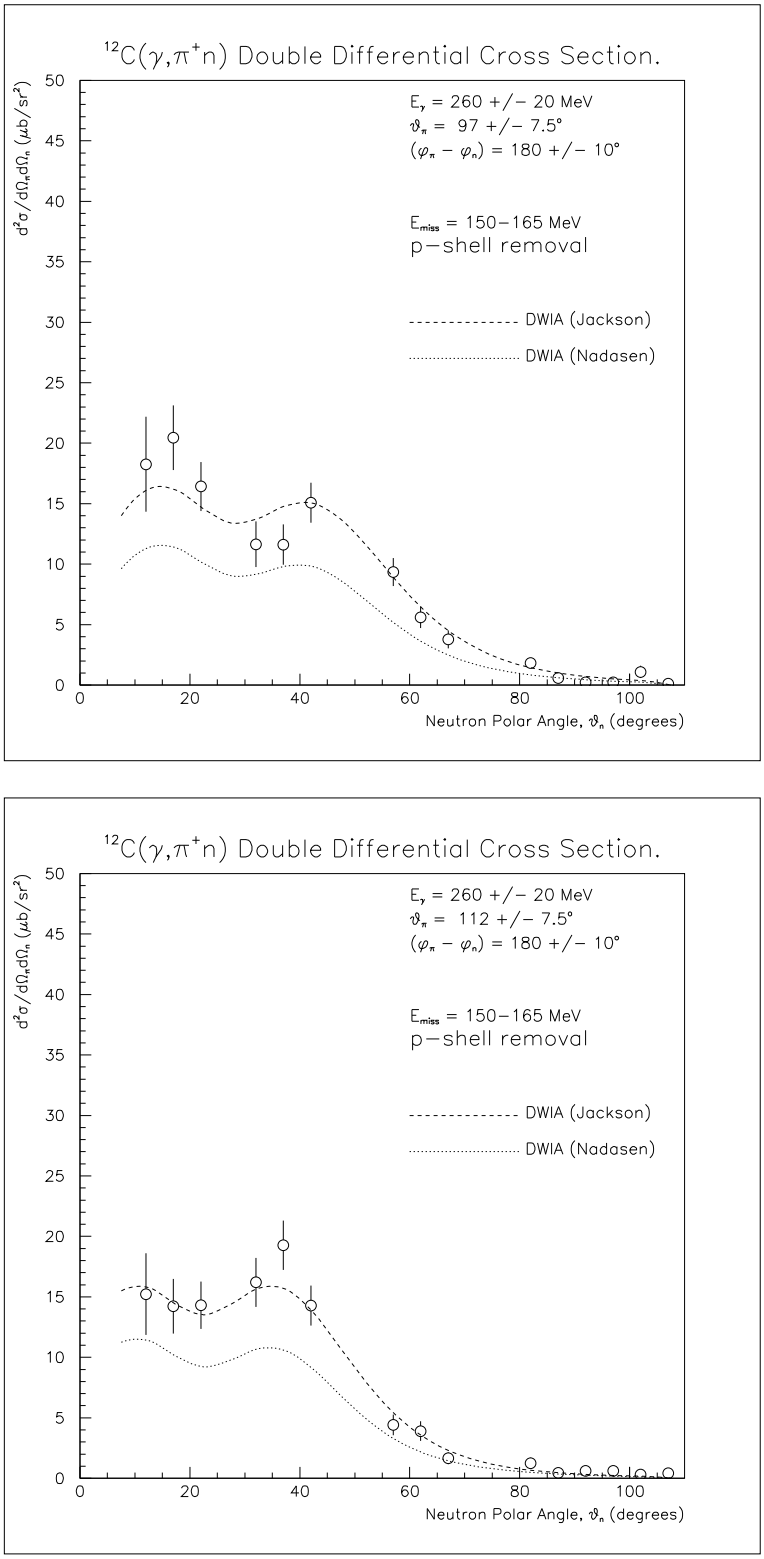

Figure 7.2: *Double Differential Cross Section Data*

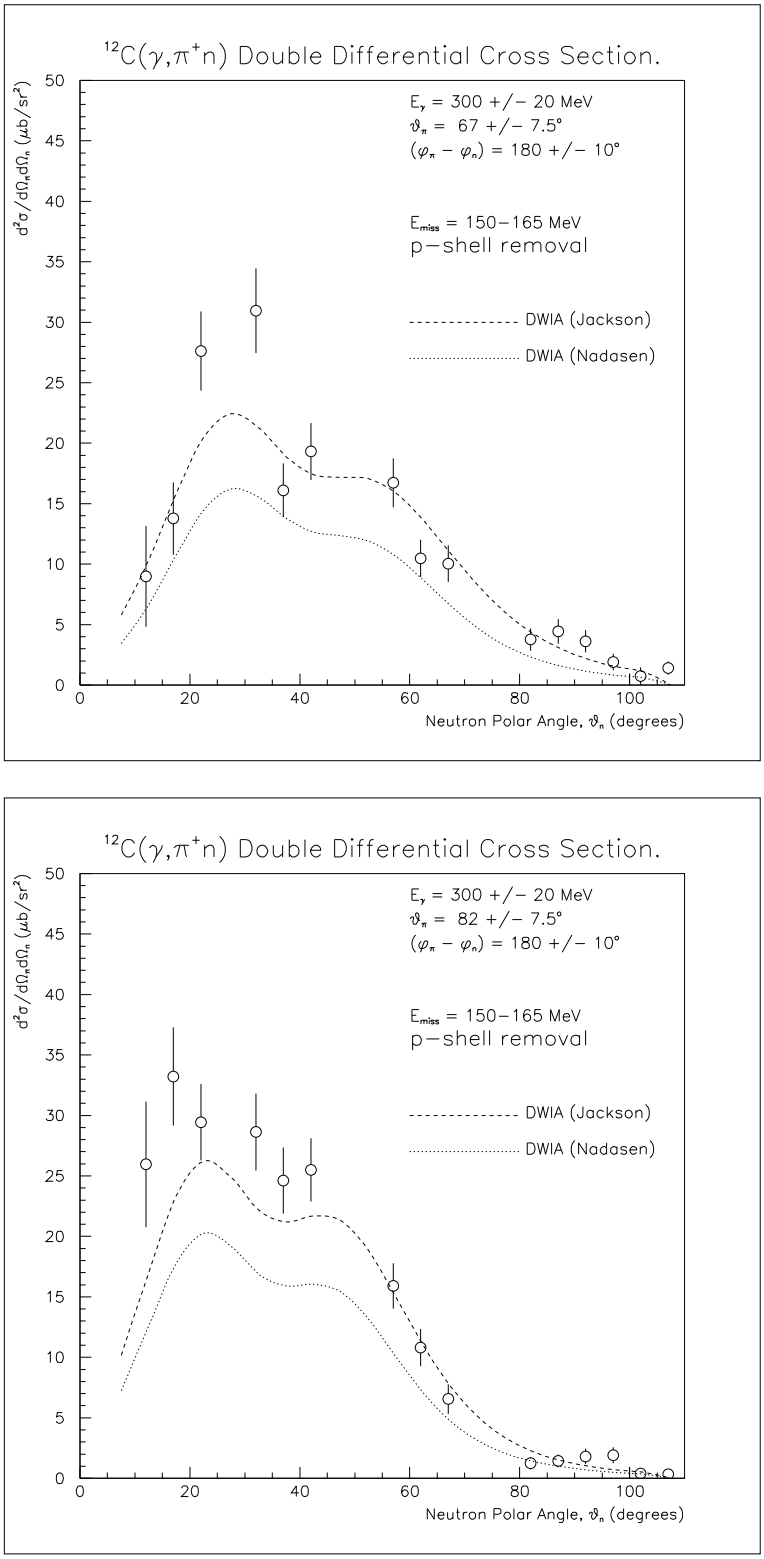

Figure 7.3: *Double Differential Cross Section Data*

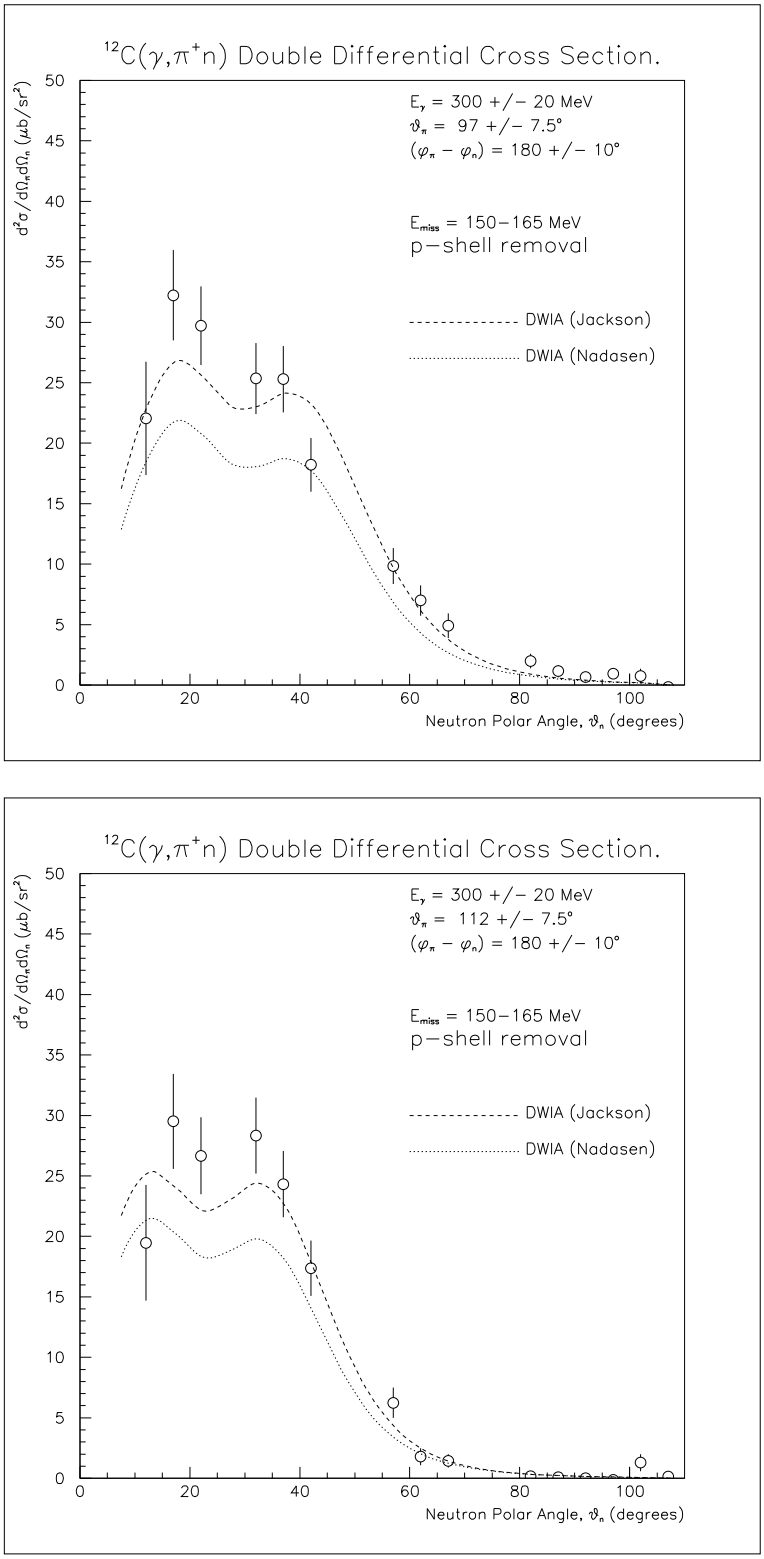

Figure 7.4: *Double Differential Cross Section Data*

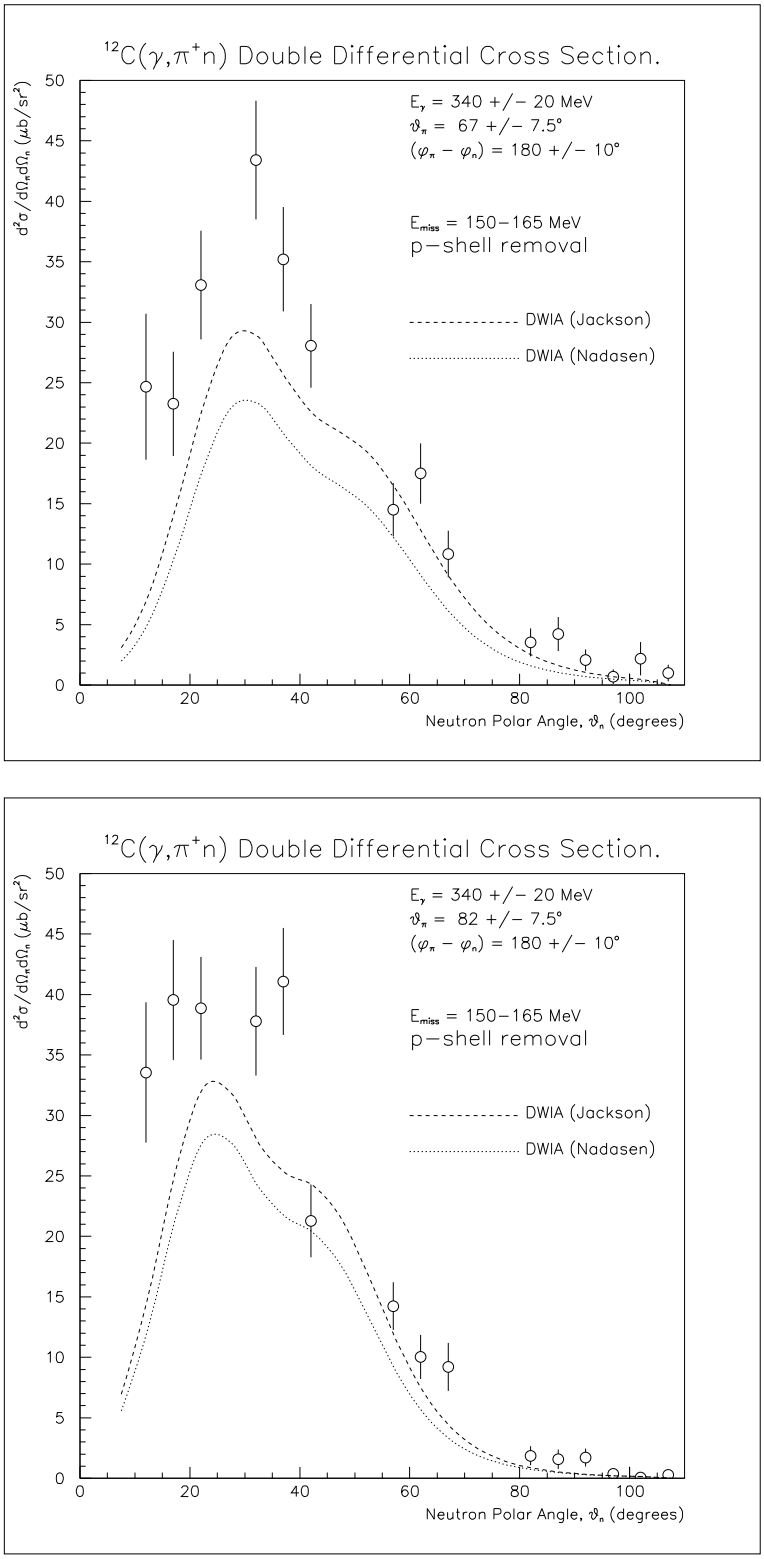

Figure 7.5: *Double Differential Cross Section Data*

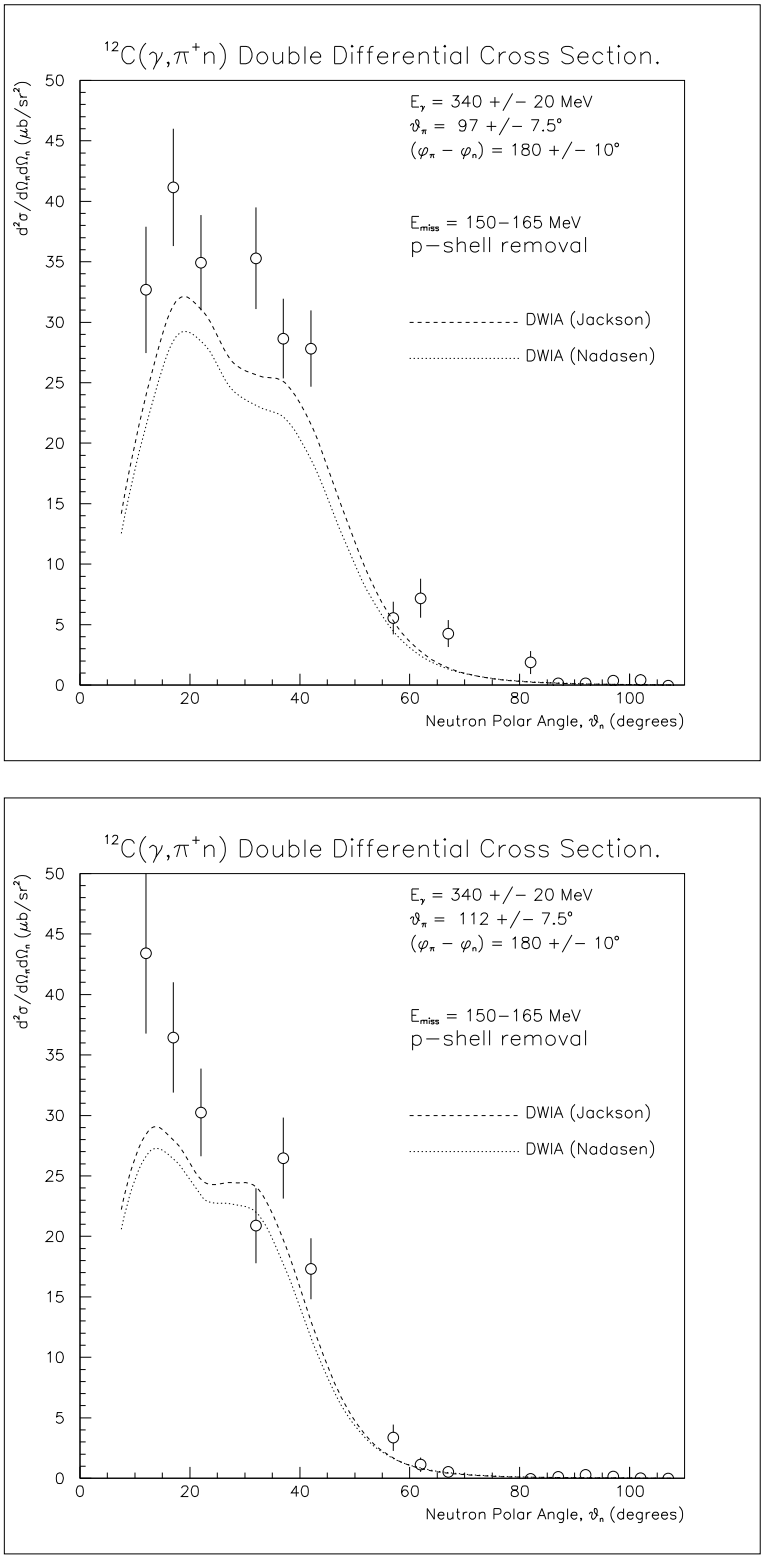

Figure 7.6: *Double Differential Cross Section Data*

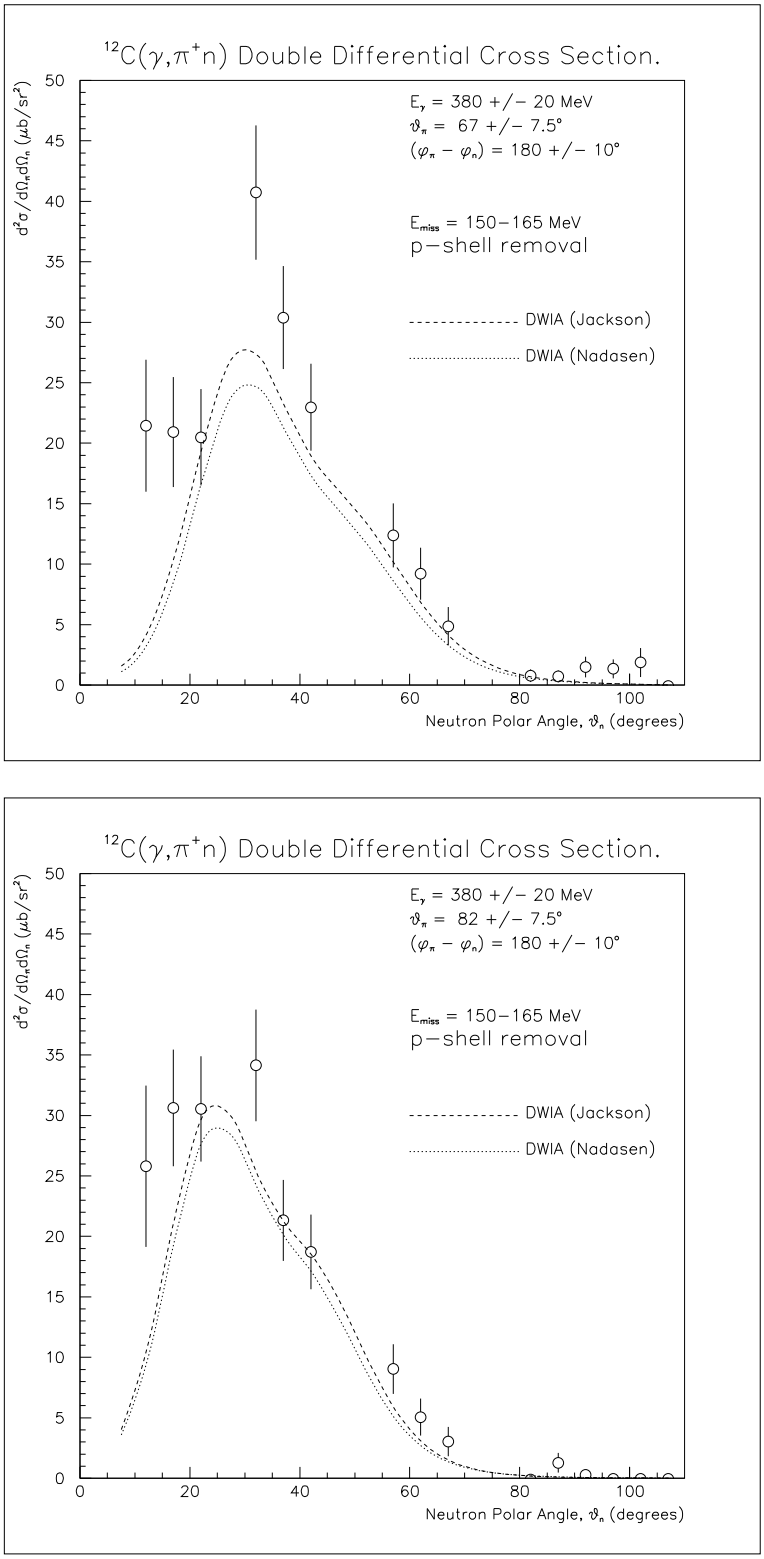

Figure 7.7: *Double Differential Cross Section Data*

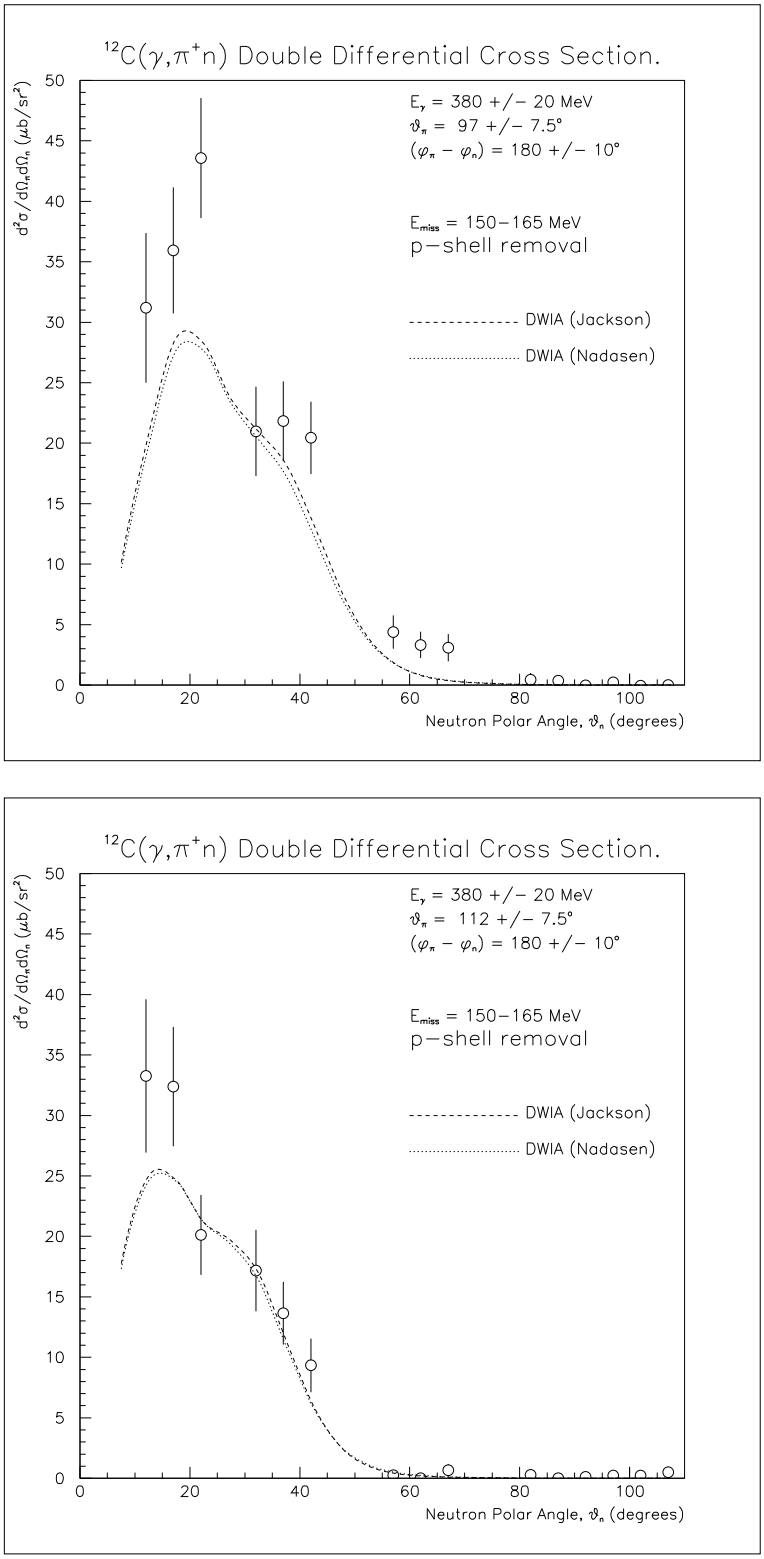

Figure 7.8: *Double Differential Cross Section Data*

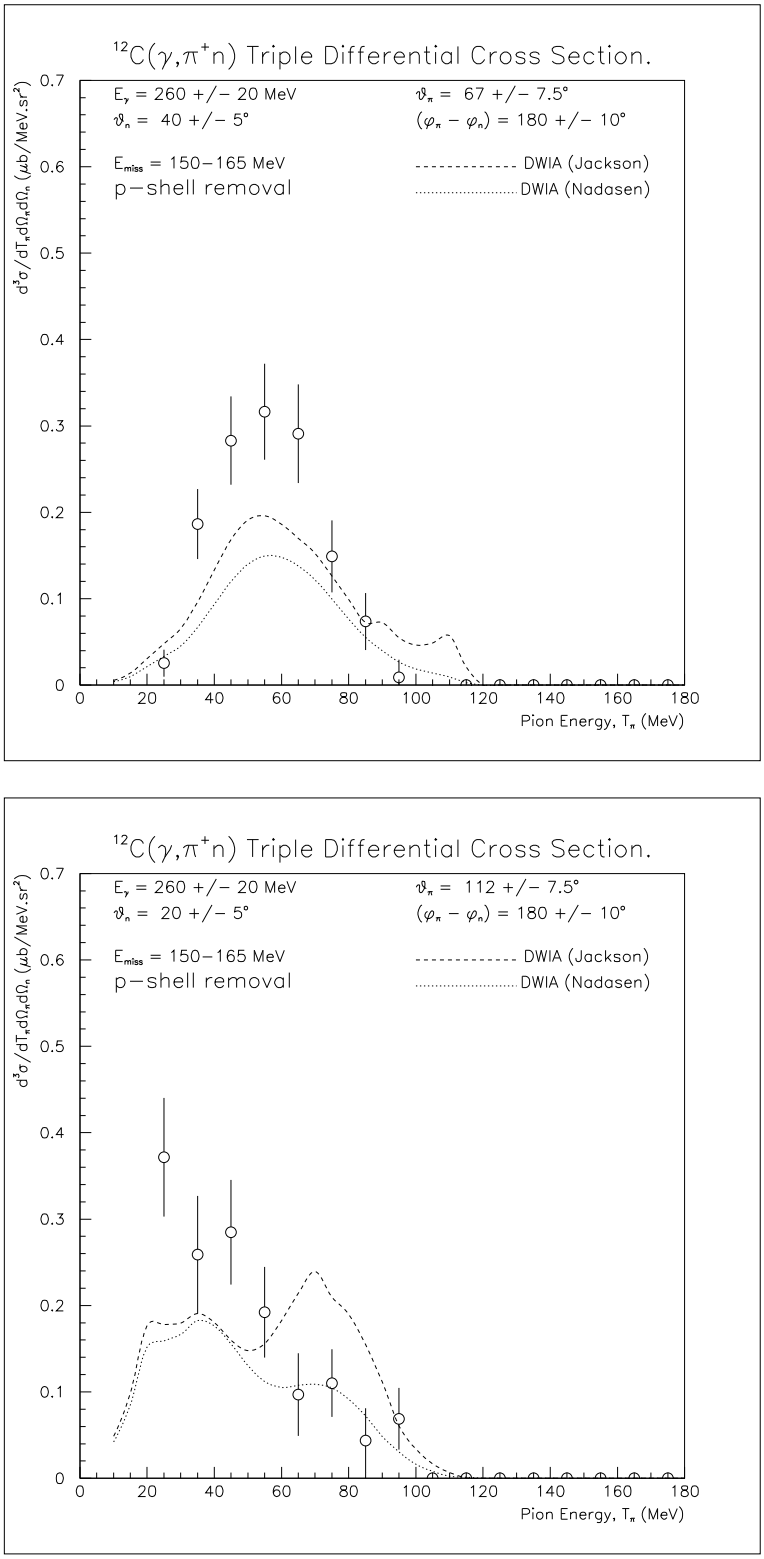

Figure 7.9: *Triple Differential Cross Section Data*

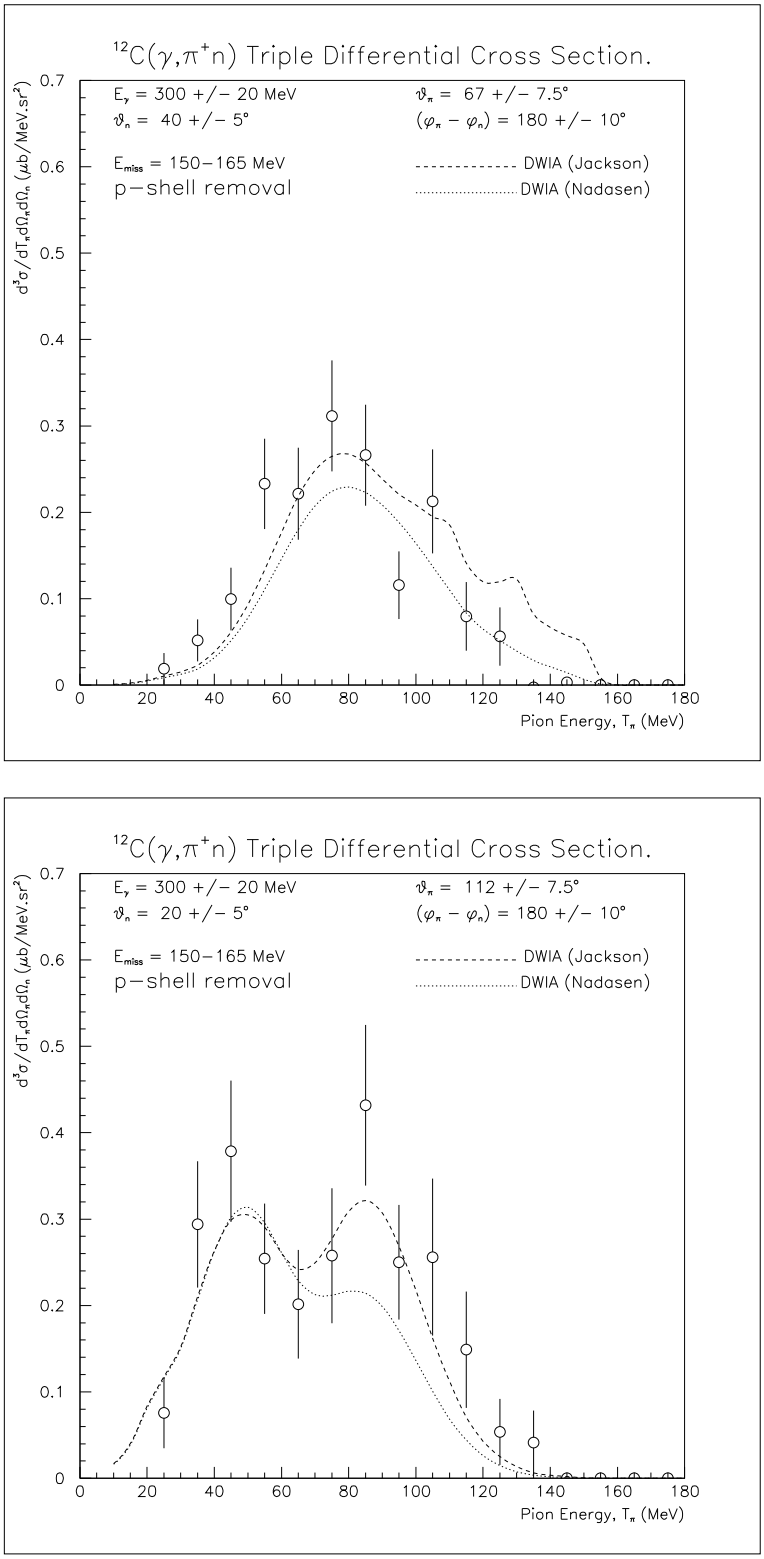

Figure 7.10: *Triple Differential Cross Section Data*

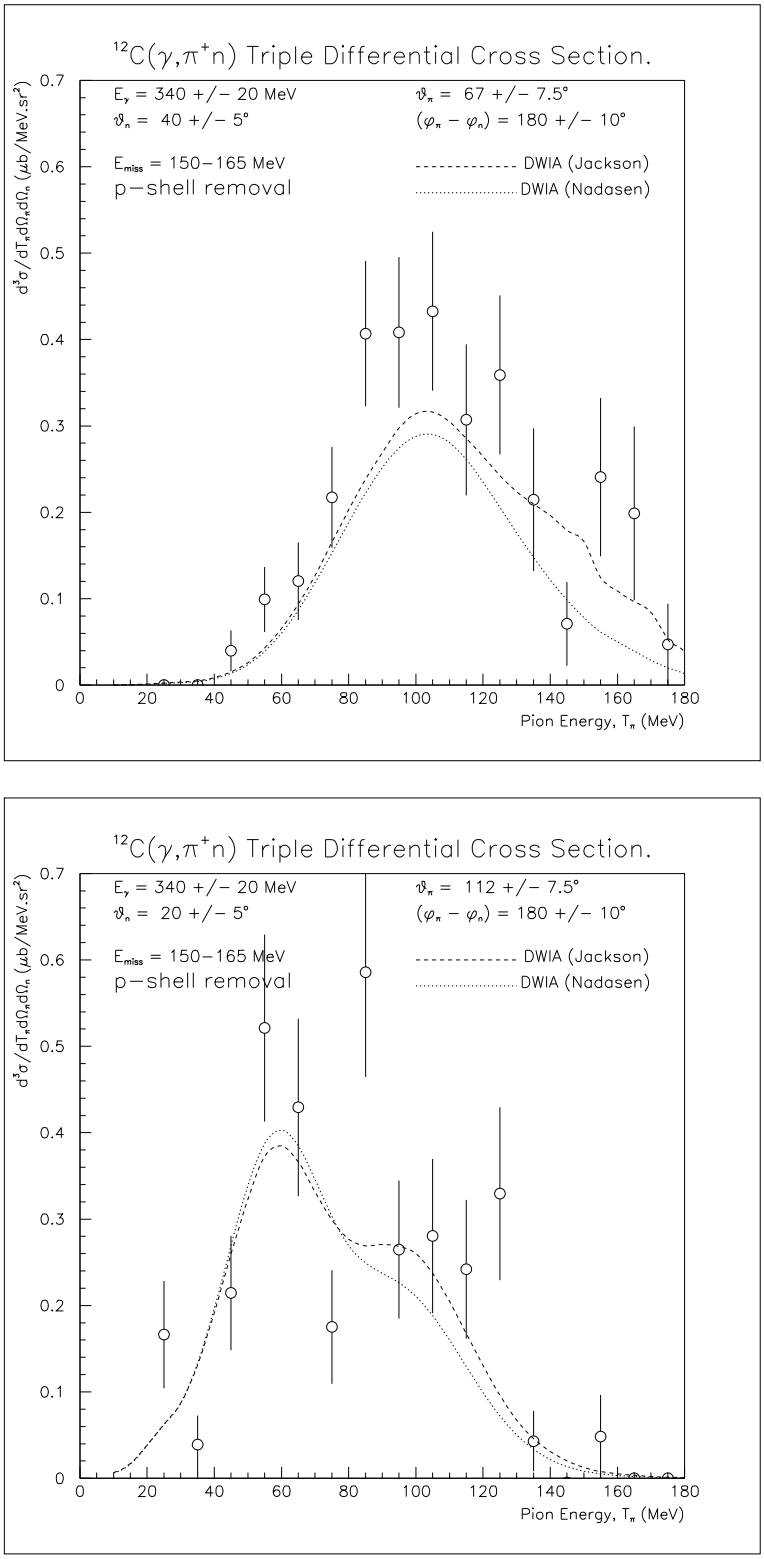

Figure 7.11: *Triple Differential Cross Section Data*

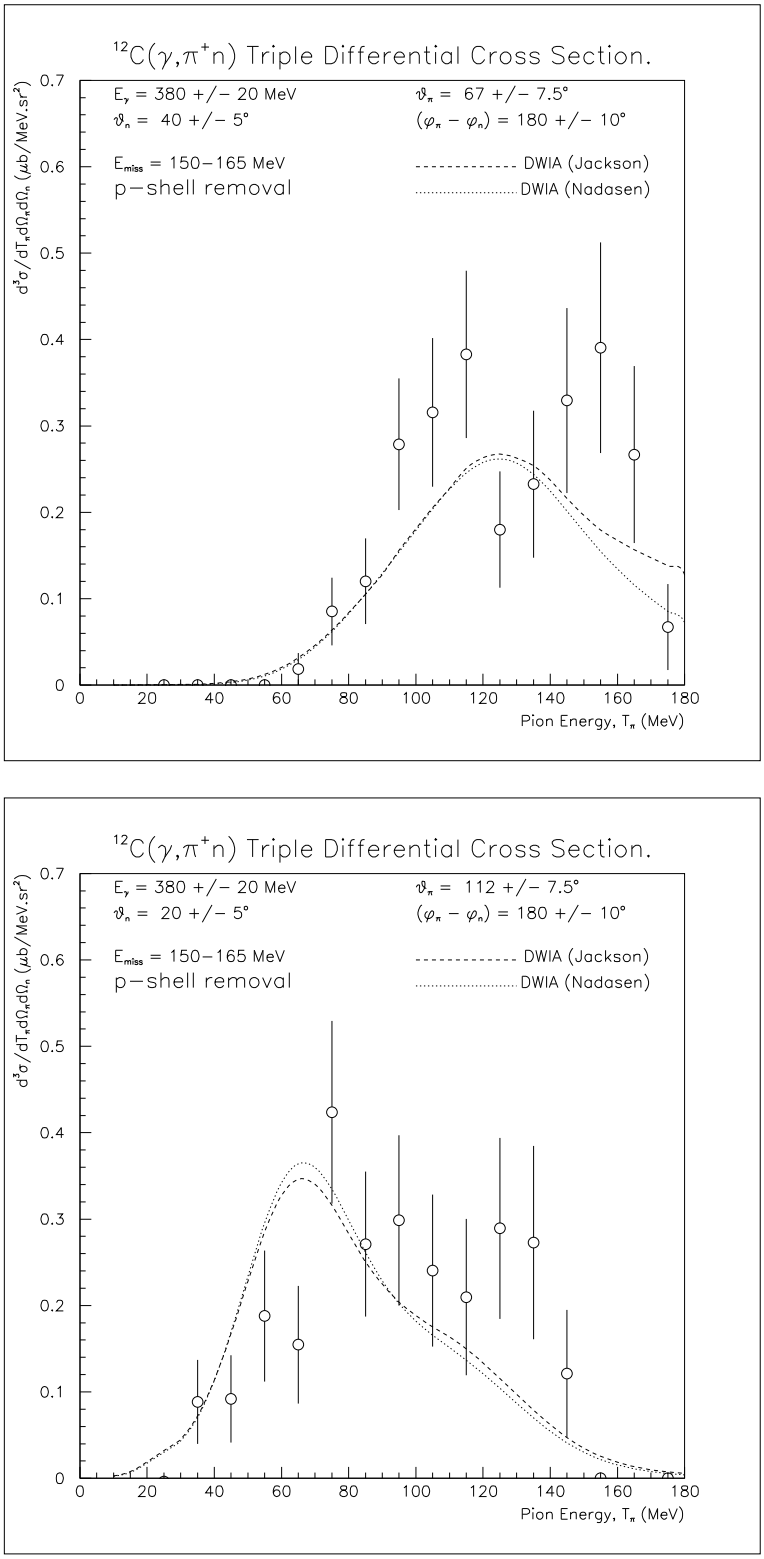

Figure 7.12: *Triple Differential Cross Section Data*

7.2 Comparison of Data with Carrasco Theory

The comparison with Carrasco theory is desirable because it represents a microscopic approach to the problem including the many medium effects that are of interest in these reaction studies, in particular Δ-propagation. There are, however, some problems in performing the comparison with the exclusive $^{12}C(\gamma, \pi^+n)$ reaction studied here and this section outlines these problems and suggests how they could be overcome. This is not to suggest that meaningful comparison is not possible, simply that there are complexities to be considered which are beyond the scope of the current work. The problems are two-fold and are described separately under the headings 'Nuclear Structure' and 'Exclusivity'.

Nuclear Structure

Carrasco theory, which is discussed more fully in Chapter 2, is based on a nuclear matter calculation which is applied to the finite nucleus by the use of the local density approximation. The main consequence of this is a lack of nuclear structure effects in the model; nucleons preside in a Fermi gas as opposed to the single particle wave functions of the shell model. The model therefore cannot be used to study p-shell nucleon removal as was the case with the DWIA discussed earlier. This weakness is shown explicitly where the missing energy spectra, for exclusive π^+n events, of theory and data are compared in figure 7.13. The theoretical missing energy is essentially 20 MeV lower than that of the data and thus it will predict correspondingly higher kinetic energy distributions for the produced particles. Perhaps, it would be possible to incorporate nuclear structure by the use of momentum wave functions and binding energies but these effects are not in the model as it stands which makes it difficult to compare to measurements sensitive to these effects such as the exclusive data presented in this thesis. A first order attempt at meaningful comparison can be made by summing data and theory over a wide missing energy range incorporating p and s-shell nucleon removal. This, however, has implications for the exclusive nature of the measurement which presents a new problem.

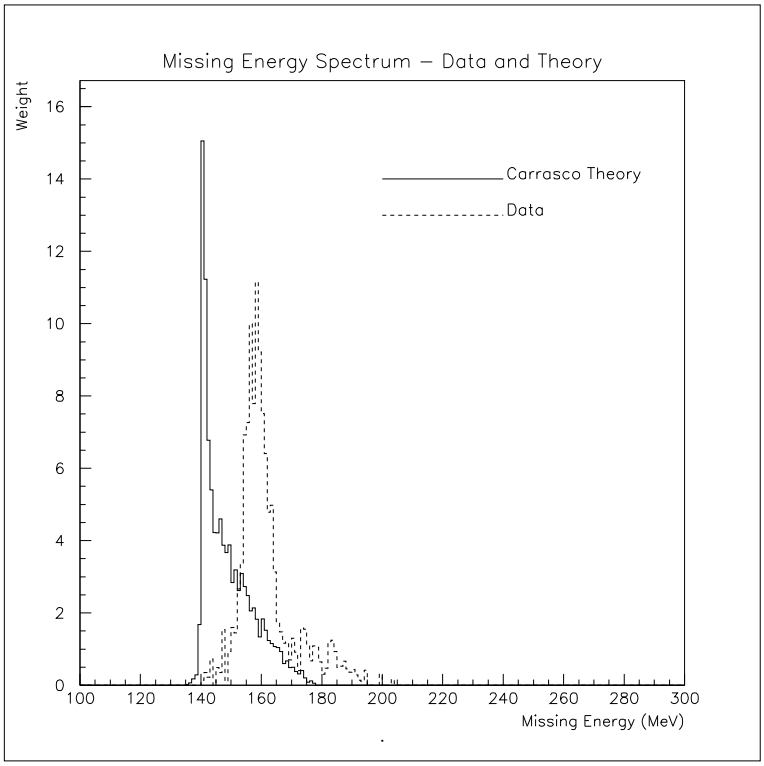

Figure 7.13: *Comparison of Missing Energy Spectrum in Theory and Data*

Exclusivity

In the comparison of data and DWIA predictions, only p-shell removal was considered. This was achieved by cutting on the corresponding peak in the missing energy spectrum. This in effect means that the residual nucleus was left intact, in the ground or a lowly excited state. This guarantees that the measurement was truly exclusive $(\gamma, \pi^+\mathrm{n})$. If however one studies higher missing energies there is no longer any guarantee that a third undetected particle was not emitted in the reaction. Thus comparison with theory must be able to account for this. The Carrasco and Oset code generates events via a Monte Carlo method and comparison was made with data by selecting the two-particle π^+n channel in both theory and data. However, a proper comparison would require consideration of the detector geometry to ascertain how many multi-particle events are recorded in the data.

The problem of exclusivity increases with incident photon energy as the likelihood of multi-particle emission increases. Comparisons of data and theory should

be possible at lower energies and figures 7.14 to 7.16 present double differential cross sections for photon energies regions between 240 and 320 MeV. A neutron lower energy threshold of 30 MeV has been applied due to limitations in the theory. The large binning employed is partly in order to reduce the effects of the nuclear structure which may be partially smeared out and also to give better statistics such that one can ascertain if the theory predicts the overall magnitude of the cross section. At higher energies, the theory falls below the data which is probably due to the presence of multi-particle events in the data which have not been included in the theory.

Conclusion

As it stands the theory does quite well in reproducing the data at the lower photon energies studied. Certainly, future more detailed comparisons are to be encouraged.

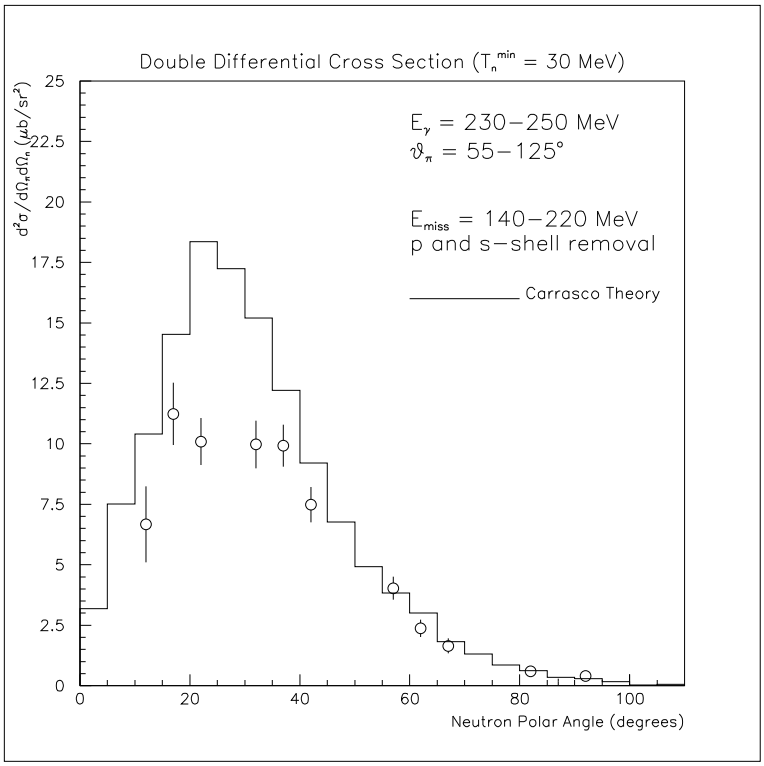

Figure 7.14: *Double Differential Cross Section Data*

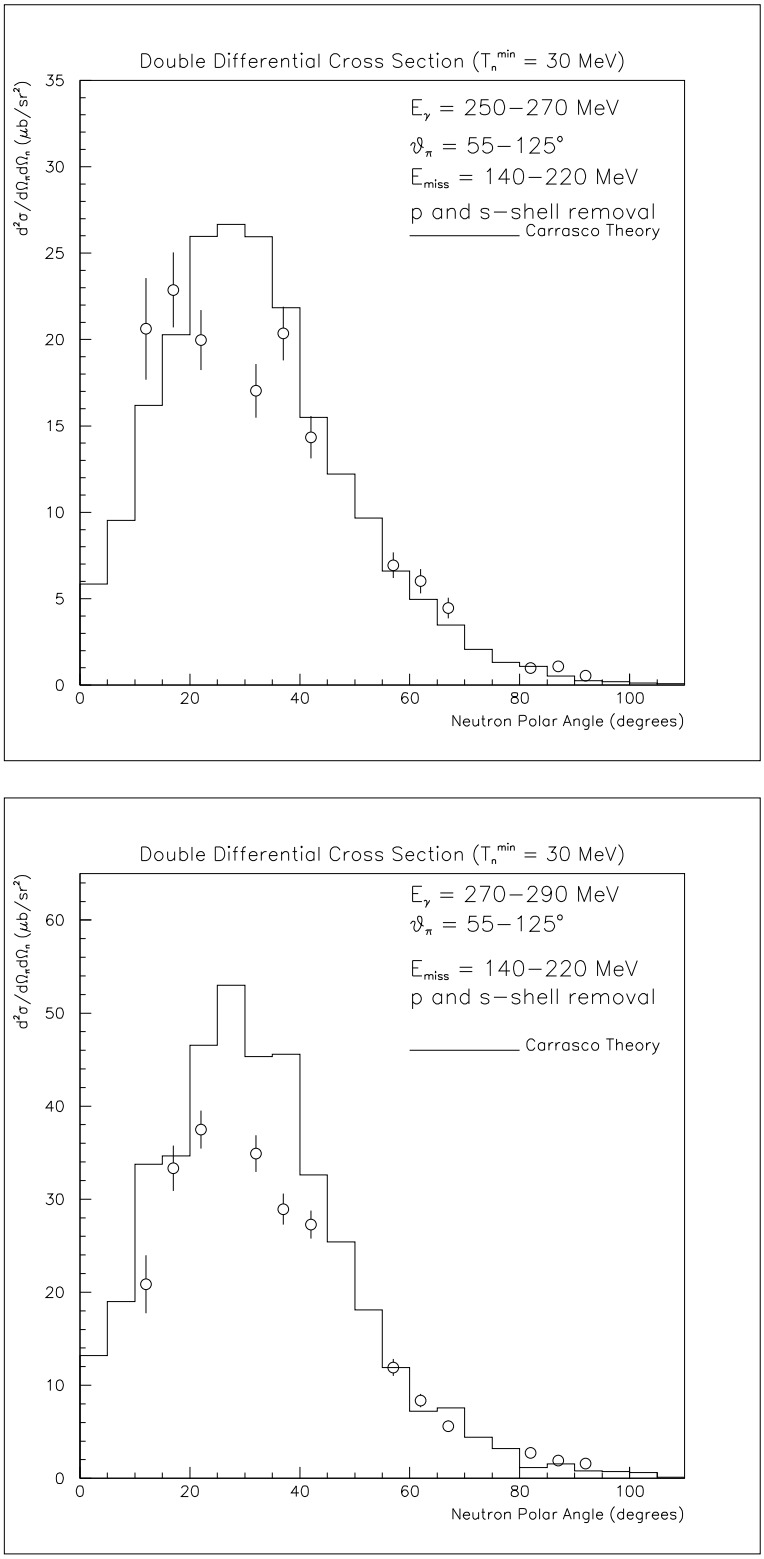

Figure 7.15: *Double Differential Cross Section Data*

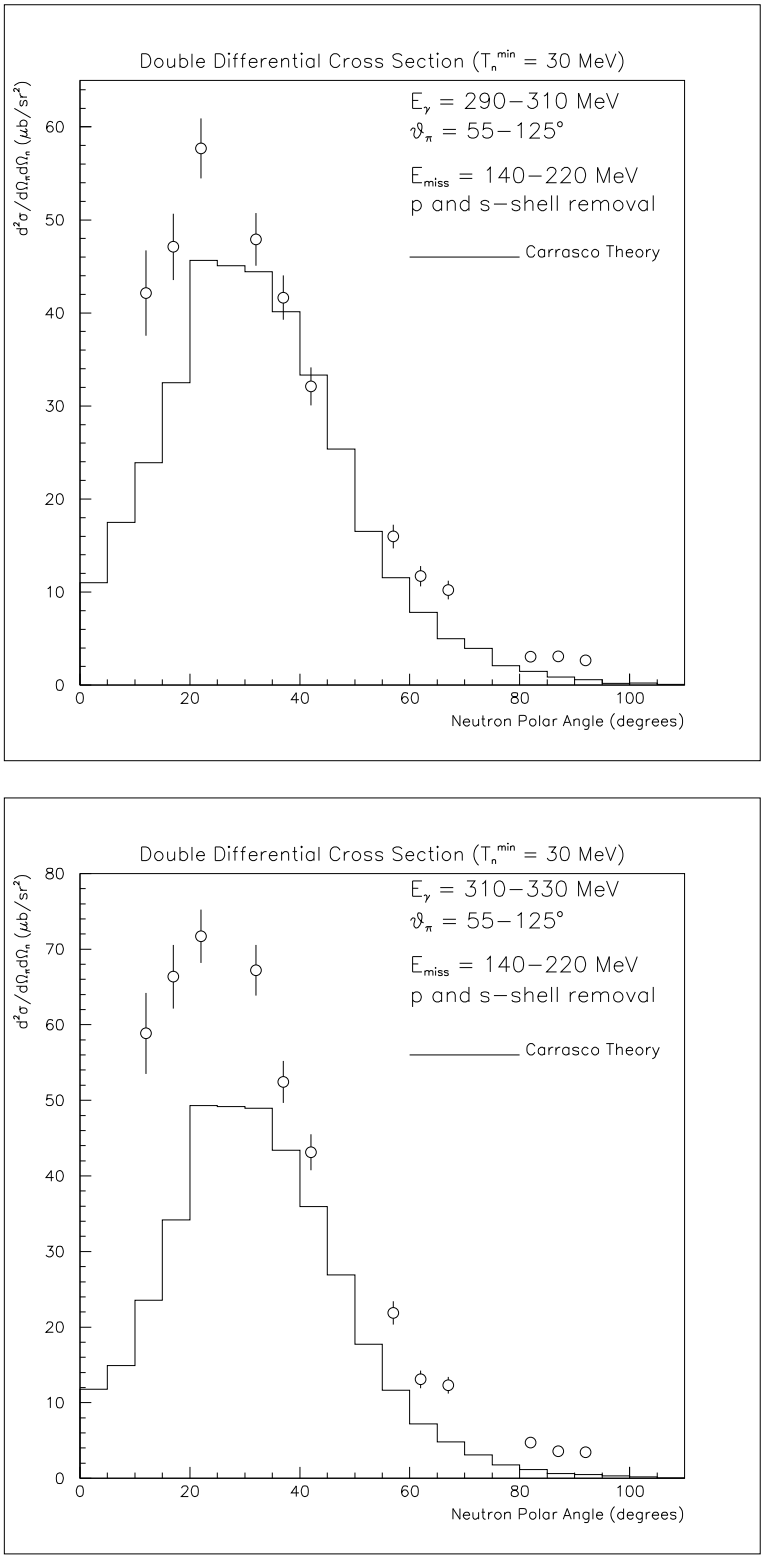

Figure 7.16: *Double Differential Cross Section Data*

Chapter 8

Conclusions

The conclusions that can be drawn from the work described in this thesis fall into two categories; those relating to the experimental techniques developed and employed and those relating to the results extracted and their implications for the study of nuclear pion photoproduction. In making these conclusions, the opportunity is taken to suggest possible detector improvements and future reaction studies.

Experimental Techniques

The main innovation of the current work has been the development of a pion detection technique using the plastic scintillator hodoscope, PiP. The problems overcome in developing the method were discussed specifically in Chapter 5 and from it one can conclude that with support for afterpulse detection and careful calibration and analysis, PiP can be used as an effective large solid angle, moderate resolution pion detector.

Although emphasis has been placed on the PiP detector, the measurements made in this work rely equally upon the Glasgow photon tagging spectrometer and the Tübingen time-of-flight array, TOF. This work represents one of the initial studies using the combined PiP-TOF-Tagger system to perform exclusive coincidence reaction measurements. In particular, the development of the weighted subevent method of data analysis has been important in order that randoms subtractions and detection efficiencies could be properly and efficiently treated in the

extraction of cross section results.

Although the detector system performed adequately for the current study, future improvements which would be desirable include better vertical position resolution in the PiP detector. This would be essential if, as is proposed, asymmetries are to be measured using polarised photon beams. Other minor improvements could include the use of a longer pion afterpulse inspect period in order to facilitate more effective randoms subtraction and the collection of more calibration data such that the pion detection efficiency could be more precisely obtained.

Pion Photoproduction in Nuclei

The results of this thesis represent the first comprehensive measurements of exclusive nuclear pion photoproduction reactions in the Δ-region, the previous measurements being performed in very restricted kinematics [Pha91, Gla79a]. The differential cross sections for p-shell excitation of the residual nucleus were measured and compared favourably with the DWIA predictions although limitations in the optical potentials employed should be noted. This suggests that the the impulse approximation is capable of describing the quasi-free events and casts doubt on previous suggestions that there was a large deficit in strength at forward pion angles [Pha91]. This conclusion, however, does not preclude the existence of new non-quasi-free mechanisms and a careful analysis of the higher missing energy and possibly multi-particle events would be required to ascertain if excess strength is present. This undertaking is, however, outside the scope of the current work where the aims were the development of the detection technique and a survey of the reaction in the low missing energy region. Although the data set is comprehensive, this is not to say it is without weaknesses. Certainly, a higher level of statistics is desirable to avoid the need for the large bin sizes used in the presentation of the data. The current study has been the first major test of the detection system and with the lessons learned future studies would be able to optimise the data collection and hopefully obtain better statistics in a comparable time frame. Future reaction studies could also exploit the recent development of polarised photon beams at Mainz. The study of asymmetries should provide even more sensitive tests of medium modifications to the elementary pion production

operator and has been actively encouraged by theorists [Li93]. This work provides an important contribution to the available data in this field and it is hoped that it will stimulate theoretical investigation and thus forward our understanding of nuclear photoreactions and the nature of the nucleus itself.

Appendix A

Tabulation of Results

The following tables represent the numerical values of the double and triple differential cross sections which were plotted in chapter 7. The errors quoted are due to statistics. A further 15% systematic error is common to all the data points.

	^{12}C(γ, π^+n) p-shell nucleon removal			
	$d^2\sigma/d\Omega_\pi d\Omega_n\,(\mu b/sr^2)$			
$\bar{\theta}_n^{LAB}$	$\bar{\theta}_\pi^{LAB} = 67^\circ$	$\bar{\theta}_\pi^{LAB} = 82^\circ$	$\bar{\theta}_\pi^{LAB} = 97^\circ$	$\bar{\theta}_\pi^{LAB} = 112^\circ$
12.	9.18 ± 2.73	18.06 ± 3.64	18.25 ± 3.92	15.23 ± 3.38
17.	16.58 ± 2.85	20.18 ± 2.92	20.46 ± 2.66	14.23 ± 2.26
22.	17.46 ± 2.05	17.26 ± 2.05	16.42 ± 2.01	14.30 ± 1.96
32.	12.18 ± 1.85	16.56 ± 1.87	11.64 ± 1.89	16.20 ± 2.03
37.	14.16 ± 1.79	14.46 ± 1.73	11.62 ± 1.67	19.27 ± 2.03
42.	12.22 ± 1.58	11.70 ± 1.43	15.08 ± 1.66	14.27 ± 1.65
57.	7.60 ± 1.09	8.76 ± 1.08	9.35 ± 1.17	4.42 ± 0.86
62.	7.58 ± 1.14	6.50 ± 0.99	5.61 ± 0.90	3.89 ± 0.81
67.	7.12 ± 1.05	5.13 ± 0.89	3.78 ± 0.74	1.66 ± 0.49
82.	3.00 ± 0.64	1.26 ± 0.47	1.82 ± 0.44	1.26 ± 0.45
87.	1.36 ± 0.42	0.99 ± 0.37	0.59 ± 0.28	0.44 ± 0.34
92.	1.21 ± 0.39	1.09 ± 0.40	0.22 ± 0.23	0.62 ± 0.34
97.	1.07 ± 0.41	1.48 ± 0.45	0.23 ± 0.18	0.61 ± 0.33
102.	1.53 ± 0.76	1.88 ± 0.79	1.09 ± 0.52	0.32 ± 0.28
107.	0.81 ± 0.36	0.65 ± 0.33	0.11 ± 0.15	0.42 ± 0.23

Table A.1: $< \mathrm{E}_\gamma > = 260\,\mathrm{MeV}$

	^{12}C(γ, π^+n) p-shell nucleon removal			
	$d^2\sigma/d\Omega_\pi d\Omega_n\,(\mu b/sr^2)$			
$\bar{\theta}_n^{LAB}$	$\bar{\theta}_\pi^{LAB} = 67^\circ$	$\bar{\theta}_\pi^{LAB} = 82^\circ$	$\bar{\theta}_\pi^{LAB} = 97^\circ$	$\bar{\theta}_\pi^{LAB} = 112^\circ$
12.	8.98 ± 4.16	25.96 ± 5.19	22.05 ± 4.69	19.46 ± 4.78
17.	13.77 ± 2.98	33.21 ± 4.06	32.23 ± 3.74	29.51 ± 3.93
22.	27.61 ± 3.28	28.45 ± 3.15	29.70 ± 3.25	26.66 ± 3.18
32.	30.95 ± 3.51	28.62 ± 3.18	25.35 ± 2.93	28.34 ± 3.15
37.	16.11 ± 2.22	24.62 ± 2.74	25.30 ± 2.75	24.32 ± 2.74
42.	19.31 ± 2.36	25.50 ± 2.62	18.22 ± 2.22	17.37 ± 2.28
57.	16.72 ± 2.02	15.92 ± 1.87	9.85 ± 1.49	6.24 ± 1.26
62.	10.48 ± 1.56	10.81 ± 1.54	7.00 ± 1.25	1.78 ± 0.71
67.	10.03 ± 1.52	6.56 ± 1.22	4.92 ± 1.03	1.44 ± 0.55
82.	3.77 ± 0.91	1.24 ± 0.53	1.98 ± 0.61	0.17 ± 0.19
87.	4.45 ± 1.03	1.43 ± 0.52	1.16 ± 0.51	0.10 ± 0.15
92.	3.63 ± 0.92	1.81 ± 0.65	0.65 ± 0.44	0.07 ± 0.13
97.	1.92 ± 0.69	1.91 ± 0.65	0.95 ± 0.43	-0.11 ± 0.04
102.	0.75 ± 0.71	0.38 ± 0.38	0.75 ± 0.59	1.30 ± 0.70
107.	1.41 ± 0.55	0.34 ± 0.29	-0.17 ± 0.15	0.15 ± 0.17

Table A.2: $< \mathrm{E}_\gamma > = 300\,\mathrm{MeV}$

	^{12}C(γ, π^+n) p-shell nucleon removal			
	$d^2\sigma/d\Omega_\pi d\Omega_n\,(\mu b/sr^2)$			
$\bar{\theta}_n^{LAB}$	$\bar{\theta}_\pi^{LAB} = 67^\circ$	$\bar{\theta}_\pi^{LAB} = 82^\circ$	$\bar{\theta}_\pi^{LAB} = 97^\circ$	$\bar{\theta}_\pi^{LAB} = 112^\circ$
12.	24.67 ± 6.04	33.55 ± 5.80	32.68 ± 5.22	43.40 ± 6.62
17.	23.26 ± 4.31	39.55 ± 4.95	41.14 ± 4.84	36.44 ± 4.56
22.	33.08 ± 4.49	38.86 ± 4.24	34.92 ± 3.95	30.25 ± 3.63
32.	43.40 ± 4.91	37.80 ± 4.49	35.29 ± 4.20	20.88 ± 3.11
37.	35.20 ± 4.32	41.08 ± 4.42	28.65 ± 3.28	26.47 ± 3.36
42.	28.05 ± 3.46	21.29 ± 3.00	27.82 ± 3.14	17.33 ± 2.53
57.	14.50 ± 2.20	14.24 ± 1.98	5.54 ± 1.36	3.35 ± 1.08
62.	17.50 ± 2.49	10.04 ± 1.82	7.18 ± 1.60	1.12 ± 0.60
67.	10.84 ± 1.93	9.21 ± 1.99	4.26 ± 1.11	0.54 ± 0.39
82.	3.54 ± 1.16	1.85 ± 0.79	1.87 ± 0.95	-0.06 ± 0.03
87.	4.21 ± 1.41	1.57 ± 0.80	0.15 ± 0.20	0.11 ± 0.15
92.	2.07 ± 0.88	1.71 ± 0.75	0.14 ± 0.18	0.28 ± 0.26
97.	0.70 ± 0.59	0.36 ± 0.43	0.37 ± 0.32	0.16 ± 0.19
102.	2.18 ± 1.38	0.07 ± 0.20	0.41 ± 0.51	0.14 ± 0.05
107.	0.99 ± 0.69	0.27 ± 0.37	-0.05 ± 0.04	-0.03 ± 0.03

Table A.3: $< \mathrm{E}_\gamma > = 340\,\mathrm{MeV}$

	^{12}C(γ, π^+n) p-shell nucleon removal			
	$d^2\sigma/d\Omega_\pi d\Omega_n\,(\mu b/sr^2)$			
$\bar{\theta}_n^{LAB}$	$\bar{\theta}_\pi^{LAB} = 67^\circ$	$\bar{\theta}_\pi^{LAB} = 82^\circ$	$\bar{\theta}_\pi^{LAB} = 97^\circ$	$\bar{\theta}_\pi^{LAB} = 112^\circ$
12.	21.44 ± 5.47	25.79 ± 6.67	31.20 ± 6.19	33.27 ± 6.33
17.	20.92 ± 4.54	30.61 ± 4.82	35.94 ± 5.20	32.39 ± 4.94
22.	20.49 ± 3.97	30.54 ± 4.36	43.58 ± 4.96	20.12 ± 3.31
32.	40.73 ± 5.55	34.14 ± 4.62	20.97 ± 3.70	17.17 ± 3.37
37.	30.38 ± 4.26	21.32 ± 3.36	21.82 ± 3.29	13.65 ± 2.59
42.	22.97 ± 3.61	18.72 ± 3.01	20.44 ± 2.98	9.33 ± 2.21
57.	12.37 ± 2.65	9.03 ± 2.06	4.39 ± 1.37	0.26 ± 0.28
62.	9.21 ± 2.14	5.06 ± 1.54	3.31 ± 1.09	-0.05 ± 0.23
67.	4.86 ± 1.59	3.03 ± 1.21	3.08 ± 1.13	0.67 ± 0.51
82.	0.77 ± 0.52	-0.09 ± 0.06	0.46 ± 0.53	-0.29 ± 0.27
87.	0.73 ± 0.50	1.28 ± 0.81	0.36 ± 0.40	0.00 ± 0.27
92.	1.50 ± 0.86	0.29 ± 0.34	-0.02 ± 0.02	0.12 ± 0.24
97.	1.35 ± 0.79	-0.04 ± 0.04	0.24 ± 0.26	0.23 ± 0.23
102.	1.87 ± 1.19	-0.06 ± 0.06	-0.05 ± 0.05	0.22 ± 0.24
107.	-0.07 ± 0.05	-0.04 ± 0.04	0.00 ± 0.05	0.51 ± 0.47

Table A.4: $< \mathrm{E}_\gamma > = 380\,\mathrm{MeV}$

	^{12}C(γ, π^+n) p-shell nucleon removal			
	$d^3\sigma/dT_\pi d\Omega_\pi d\Omega_n\,(\mu b/MeV.sr^2)$			
	$< \mathrm{E}_\gamma > = 260\,\mathrm{MeV}$		$< \mathrm{E}_\gamma > = 300\,\mathrm{MeV}$	
	$\bar{\theta}_\pi^{LAB} = 67^\circ$	$\bar{\theta}_\pi^{LAB} = 112^\circ$	$\bar{\theta}_\pi^{LAB} = 67^\circ$	$\bar{\theta}_\pi^{LAB} = 112^\circ$
$T_\pi(MeV)$	$\bar{\theta}_n^{LAB} = 40^\circ$	$\bar{\theta}_n^{LAB} = 20^\circ$	$\bar{\theta}_n^{LAB} = 40^\circ$	$\bar{\theta}_n^{LAB} = 20^\circ$
25.	0.025 ± 0.015	0.372 ± 0.069	0.019 ± 0.018	0.076 ± 0.041
35.	0.186 ± 0.041	0.259 ± 0.068	0.052 ± 0.024	0.294 ± 0.073
45.	0.283 ± 0.051	0.285 ± 0.061	0.100 ± 0.036	0.379 ± 0.081
55.	0.316 ± 0.055	0.192 ± 0.052	0.233 ± 0.052	0.254 ± 0.064
65.	0.291 ± 0.057	0.097 ± 0.048	0.221 ± 0.053	0.202 ± 0.063
75.	0.149 ± 0.042	0.110 ± 0.039	0.311 ± 0.064	0.258 ± 0.078
85.	0.074 ± 0.033	0.044 ± 0.037	0.266 ± 0.058	0.432 ± 0.093
95.	0.008 ± 0.021	0.069 ± 0.037	0.116 ± 0.039	0.250 ± 0.066
105.	-0.014 ± 0.014	-	0.213 ± 0.060	0.256 ± 0.091
115.	-	-	0.080 ± 0.040	0.149 ± 0.067
125.	-	-	0.056 ± 0.034	0.054 ± 0.038
135.	-	-	-0.002 ± 0.002	0.041 ± 0.036
145.	-	-	0.003 ± 0.003	-
155.	-	-	-	-
165.	-	-	-	-
175.	-	-	-	-

Table A.5:

	^{12}C(γ, π^+n) p-shell nucleon removal			
	$d^3\sigma/dT_\pi d\Omega_\pi d\Omega_n\,(\mu b/MeV.sr^2)$			
	$< \mathrm{E}_\gamma > = 340\,\mathrm{MeV}$		$< \mathrm{E}_\gamma > = 380\,\mathrm{MeV}$	
	$\bar{\theta}_\pi^{LAB} = 67^\circ$	$\bar{\theta}_\pi^{LAB} = 112^\circ$	$\bar{\theta}_\pi^{LAB} = 67^\circ$	$\bar{\theta}_\pi^{LAB} = 112^\circ$
$T_\pi(MeV)$	$\bar{\theta}_n^{LAB} = 40^\circ$	$\bar{\theta}_n^{LAB} = 20^\circ$	$\bar{\theta}_n^{LAB} = 40^\circ$	$\bar{\theta}_n^{LAB} = 20^\circ$
25.	-	0.166 ± 0.062	-	-0.004 ± 0.004
35.	-	0.039 ± 0.033	-	0.089 ± 0.049
45.	0.040 ± 0.023	0.214 ± 0.066	-	0.092 ± 0.050
55.	0.099 ± 0.038	0.521 ± 0.108	-	0.188 ± 0.076
65.	0.120 ± 0.045	0.423 ± 0.103	0.018 ± 0.018	0.155 ± 0.068
75.	0.217 ± 0.058	0.175 ± 0.067	0.085 ± 0.039	0.424 ± 0.106
85.	0.407 ± 0.084	0.586 ± 0.121	0.120 ± 0.050	0.271 ± 0.084
95.	0.408 ± 0.087	0.265 ± 0.080	0.279 ± 0.076	0.299 ± 0.099
105.	0.433 ± 0.092	0.280 ± 0.089	0.316 ± 0.086	0.240 ± 0.088
115.	0.307 ± 0.087	0.242 ± 0.080	0.383 ± 0.097	0.210 ± 0.090
125.	0.359 ± 0.092	0.323 ± 0.100	0.180 ± 0.067	0.290 ± 0.105
135.	0.214 ± 0.083	0.043 ± 0.035	0.234 ± 0.085	0.273 ± 0.112
145.	0.071 ± 0.048	-0.005 ± 0.005	0.329 ± 0.107	0.121 ± 0.073
155.	0.241 ± 0.092	0.048 ± 0.048	0.390 ± 0.122	-
165.	0.199 ± 0.100	-	0.267 ± 0.102	-
175.	0.047 ± 0.047	-	0.067 ± 0.050	-

Table A.6:

Bibliography

[Ama64] U. Amaldi *et al.*, *Phys. Lett. B* 13 (1964) 341

[Ana76] P. S. Anan'in, I. V. Glavanokov *et al.*, *JETP* 23 (1976) 298

[Aud77] G. Audit *et al.*, *Phys. Rev. C* 15 (1977) 1415

[Abd79] I. Abdul-Jalil and Daphne. F. Jackson, *J. Phys. G* 5 (1979) 1699

[Ana82] P. S. Anan'in *et al.*, *Sov. J. Nucl. Phys.* 36 (1982) 170

[Ana84] P. S. Anan'in *et al.*, *Sov. J. Nucl. Phys.* 39 (1984) 1

[Are82] J. Arends *et al.*, *Z. Phys. A* 305 (1982) 205

[Are90] J. Arends *et al.*, *Nucl. Phys. A* 526 (1990) 479

[Ant91] I. Anthony *et al*, *NIM* A301 (1991) 230.

[Ann93] J.R.M. Annand and B. Oussena, *NIM* A330 (1993) 220.

[Ann] J.R.M Annand, I. Anthony and A. Sibhald, *ACQU Manual* Kelvin Lab Report.

[Bet34] H. Bethe and W. Heitler, *Proc. Roy. Soc. (London)* A146 (1934) 83.

[Ber67] F.A. Berends, A. Donnachie and D.L. Weaver, *Nucl. Phys. B* 4 (1967) 54

[Bet68] C. Betourne *et al.*, *Phys. Rev.* 172 1342 (1968)

[Ber71] V.B. Berensky, E.M. Lifshitz and L.P. Pitaevskii, *Relativistic Quantum Theory*, Pergamon Press, 1971

[Bil76] S.M. Bilenkii, *Introduction to Feynman Diagrams*, Pergamon Press (1976)

[Blo77] I. Blomqvist and J. M. Laget, *Nucl Phys. A* 280 (1977) 405

[Bur79] W.E. Burcham, *Elements of Nuclear Physics* Longman (1979)

[Bor89] B. Borgia, M. Diemoz and S. Morganti, *NIMS* A278 (1989) 699

[Bru82] R, Brun, M. Hansroul and J.C. Lassalle, *GEANT User's Guide* DD/EE/82 CERN (1982)

[Ben90] C. Benhold, L. Tiator and L.E. Wright, *Can. J. Phys.* 68 (1990) 1270

[Bra91] D. Branford (Ed.), *Future Detectors for Photonuclear Experiments*, Edinburgh University (1991).

[Che57] G.F. Chew, M.L. Goldberger, F.E. Low and Y. Nambu, *Phys. Rev.* 106 (1957) 1345

[Cra70] R.L. Craun and D.L. Smith, *NIMS* 80 (1970) 239.

[Cha77] N.S. Chant and P. Roos, *Phys. Rev C* 15 (1977) 15

[Cec79] R.A. Cecil *et al*, *NIM* 161 (1979) 439

[Cot80] W.B. Cottingame and D.B. Holtkamp, *Phys. Rev. Lett.* 45 (1980) 1828

[Car82] J.A. Carr *et al.*, *Phys. Rev. C* 25 (1982) 952

[Car92a] R. Carrasco and E. Oset, *Nucl. Phys. A* 536 (1992) 445

[Car92b] R. Carrasco and E. Oset, *Nucl. Phys. A* 541 (1992) 585

[Car92c] R. Carrasco and E. Oset, *Phys. Rev. C* 45 (1992) 764

[Car94] R. Carrasco and E. Oset, *Nucl. Phys. A* 570 (1994) 701

[Cro94] G.E. Cross, *Ph.D Thesis*, University of Glasgow, 1994.

[Dav86] R. Davidson *et al.*, *Phys. Rev. Lett.* 56 (1986) 804

[Dre92] D. Drechsel and L. Tiator, *J. Phys. G.* 18 (1992) 449

[Eis76] J.M. Eisenberg and W. Greiner, *Nuclear Theory*, North-Holland (1976)

[Epo79] V. N. Eponeshnikov *et al.*, *JETP Lett.* 29 (1979) 401

[Fet71] A. Fetter and J. Walecka, *Quantum Theory of Many-Particle Systems*, McGraw-Hill (1971)

[Fin72] D. Findlay and R. O. Owens, *Nucl. Phys. A* 292 (1977) 53

[Gaa91] C. Gaarde, *Ann. Rev. Nucl. Part. Sci.* (1991) 187

[Gar81] M. Gari and H. Hebach, *Physics Reports* 72 (1981) 1

[Gla79a] I. V. Glavanokov, *Sov. J. Nucl. Phys.* 29 (1979) 746

[Gla79b] I. V. Glavanokov, *Sov. J. Nucl. Phys.* 30 (1979) 465

[Gla79] I. V. Glavanokov, *Sov. J. Nucl. Phys.* 49 (1989) 58

[Hom83] S. Homma *et al.*, *Phys. Rev. C* 27 (1983) 31

[Hom84] S. Homma *et al.*, *Phys. Rev. Lett.* 52 (1984) 2026

[Her90] H. Herminghaus *et al*, *Proc. Linear Accelerator Conf.*, Albequerque, 1990.

[Koc84] J. H. Koch, E. J. Moniz, N. Ohtsuka, *Annals of Physics* 154 (1984) 99

[Kan86] M. Kanazawa *et al.*, *Phys. Rev. C* 35 (1986) 1828

[Kis73] L.S. Kisslinger and W.L. Wang, *Phys. Rev. Lett.* 30 (1973) 1071

[Lag72] J. M. Laget, *Nucl. Phys. A* 194 (1972) 81

[Lag88] J. M. Laget, *Nucl. Phys. A* 481 (1988) 765

[Lev51] J. S. Levinger, *Phys. Rev.* 84 (1951) 43

[Led78] C.M. Lederer and V.S. Shirley, *Table of Isotopes*, John Wiley & Sons (1978)

[Li93] X. Li, L. E. Wright and C. Benhold, *Phys. Rev. C* 48 (1993) 816

[McG94] J.C. McGeorge, *Private Communication.*

[Mai94] *Jahresbericht 1992-1993*, Institut für Kernphysik, Universität Mainz, 1994.

[Ne] *Scintillation Materials*, NE Technology Limited.

[Nad81] A. Nadasen *et al.*, Phys. Rev. C 23 (1981) 1023

[Nag91] A. Nagl, V. Devanathon and H. Überall, *Nuclear Pion Photoproduction* (1991)

[Noz90] S. Nozawa *et al.*, *Nucl. Phys. A* 513 (1990) 459

[Ols74] M.G. Olsson, *Nucl. Phys. B* 78 (1974) 55

[Ose79] E. Oset and W. Weise, *Nucl. Phys. A* 319 (1979) 477

[Ose82] E. Oset, H. Toki and W. Weise, *Physics Reports* 83 (1982) 281

[Ose87] E. Oset, *Nucl. Phys. A* 468 (1987) 631

[Owe90] R. O. Owens, *NIMS A* 288 (1990) 574

[Pha91] L. D. Pham *et al.*, *Phys. Rev. C* 46 (1992) 621

[Par79] N. Paras *et al*, *Phys. Rev. Lett.* 42 (1979) 1455

[Rao70] K.S. Rao *et al.*, *Nucl. Phys. A* 159 (1970) 97

[Ste87] G. van der Steenhoven, *Ground-state correlations in* ^{12}C *and the mechanism of the* $(e, e'p)$ *reaction*, ICG Printing (1987)

[Sat93] T. Sato and T. Takaki, *Nucl. Phys. A* 562 (1993) 673

[Sin81] M.K. Singham and F. Tabakin, *Annals of Physics* 135 (1981) 71

[Sch82] P. Schwandt *et al.*, *Phys. Rev. C* 26 (1982) 55

[Ste95] G. van der Steenhoven, *Private Communication.*

[Tia84] L. Tiator and L. Wright, *Phys. Rev. C* 30 (1984) 989

[Tia88] L. Tiator *et al*, *Nucl. Phys. A* 485 (1988) 565

[Vac94] M.J Vincente Vacas *et al.*, *Nucl. Phys. A* 568 (1994) 855

[Wat54] K. Watson, *Phys. Rev.* 95 (1954) 228

[Wei77] W. Weise, *Nucl. Phys. A* 278 (1977) 402

[Wit86] R. Wittman and Nimai C. Mukhopadhay, *Phys. Rev. Lett.* 57 (1986) 1113